Møller polarimetry for the BGO-OD experiment and cross section measurement of the reaction $\gamma p \rightarrow K^{+}\Lambda$ at the extreme forward angles

Dissertation
zur
Erlangung des Doktorgrades (Dr. rer. nat.)
der
Mathematisch-Naturwissenschaftlichen Fakultät
der
Rheinischen Friedrich-Wilhelms-Universität Bonn

von
Thomas Zimmermann
aus
Neuwied

Bonn, August, 2016

Dieser Forschungsbericht wurde als Dissertation von der Mathematisch-Naturwissenschaftlichen Fakultät der Universität Bonn angenommen und ist auf dem Hochschulschriftenserver der ULB Bonn http://hss.ulb.uni-bonn.de/diss_online elektronisch publiziert.

1. Gutachter:	Prof. Dr. Hartmut Schmieden
2. Gutachter:	Prof. Dr. Bernhard Ketzer
Tag der Promotion:	19.12.2016
Erscheinungsjahr:	2017

Abstract

The BGO-OD experiment, located at the electron accelerator ELSA at the University of Bonn, is designed to study nucleon and hyperon excitations via meson photoproduction using an energy tagged bremsstrahlung photon beam, with the emphasis on understanding the reaction dynamics. It consists of a central BGO calorimeter with a magnetic spectrometer in forward directions. The physics program includes the measurement of polarization observables, some of which can be accessed using polarized photon beams. Circularly polarized photon beams can be produced via bremsstrahlung from an amorphous radiator using longitudinally polarized electrons. The degree of polarization of the photon beam depends on the transferred momentum from the beam electron to the beam photon, and the degree of polarization of the electron beam. The polarization of the electron beam is measured by a Møller polarimeter. The setup and commissioning of this polarimeter is described in this thesis.

Using a circularly polarized photon beam, several double polarization observables can be measured. For associated strangeness photoproduction, such as $\gamma p \rightarrow K^+\Lambda$ the self analyzing weak hyperon decay, allows the determination of the recoil polarization without requiring an additional recoil polarimeter. $\gamma p \rightarrow K^+\Lambda$ is therefore one of the photoproduction final states with the most polarization observable data available. Large contributions from t-channel exchange mechanisms however still leave it difficult to determine resonance, s-channel contributions in this channel. To understand the t-channel contribution, the forward angles are essential, but even in the most simplest observable, the cross section, the angular coverage is not complete. In addition the available data disagrees with each other.

The BGO-OD experiment is ideally suited to resolve these issues. The magnetic forward spectrometer covers the forward angular range and the BGO calorimeter enabled significant background reduction. The differential cross section of $\gamma p \rightarrow K^+\Lambda$ at extreme forward angles, from $\Theta^{c.m.}_{K^+} = 3°$ to 24°, is measured in this thesis. The achieved statistical and systematic uncertainties are 10 % and 30 % respectively. Within these errors the cross section fits to the model prediction of the Bonn Gatchina partial wave analysis.

For the future, more data is available for analysis, which will reduce the statistical uncertainty significantly. By the ongoing improvement of the determination of the photon flux and by better modeling the real detector efficiencies in simulated data, the systematic uncertainties can be improved by a factor of two.

Contents

CHAPTER 1

Introduction

In the early 20th century it was found that atoms are composite objects; Ernest Rutherford concluded from scattering experiments "that the atom contains a central charge distributed through a very small volume"[Rut11], which is surrounded by electrons. Soon it was shown that this central charge, the atomic core, is composed of nucleons: protons and neutrons. Half a century later it was found that also the nucleons are composed particles: they consist of quarks and the exchange particles of the strong force, gluons. The strong interaction between quarks and gluons is described by quantum chromo dynamics (QCD). In the standard model of particle physics six quarks exist, in three generations of two quarks each (up & down, strange & charm, top & bottom). Particles made up of quarks are called hadrons. Those composed of one quark and one anti quark are called mesons. Those composed of three quarks are called baryons. Based on group theory mesons and baryons can be organized in multiplets, ordered by strangeness and isospin and grouped by their internal angular momentum, spin. The isospin, I_3, is defined as $+1/2$ for up quarks, $-1/2$ for down quarks and 0 for all other quarks. The isospin of the hadron is given by the sum of the isospins of its constituents. The strangeness corresponds to the number of anti strange quarks. The two octets of the lightest mesons are the pseudoscalar mesons with spin 0 and the vector mesons with spin 1. The lightest mesons, pions, are composed of the lightest quarks and anti quarks (up and down). Therefore they have a strangeness of 0 and an isospin of -1 (π^-), 0 (π^0) or +1 (π^+).

The rules of QCD also allow the formation of bound states of more than three quarks, however these have not been previously observed. Recently particles made up of four and five quarks may have been discovered [Cho+03; Aai+15], but their inner structure is still unclear.

Quarks are only observed as bound states, which is known as confinement. As single quarks are not observed they can only be studied bound in hadrons. Therefore studying the structure of hadrons gives essential input for the development of QCD.

Scattering and production experiments are performed to investigate the structure of hadrons. The Mandelstam variables s, t and u are commonly used to describe the kinematics of such a process in a Lorentz invariant way. When considering $2 \rightarrow 2$ particle processes with initial and final state four-momenta p_1, p_2 and p_3, p_4 respectively, the Mandelstam variables are defined as:

$$s = (p_1 + p_2)^2 = (p_3 + p_4)^2, \tag{1.1}$$

$$t = (p_1 - p_3)^3 = (p_2 - p_4)^2, \tag{1.2}$$

$$u = (p_1 - p_4)^2 = (p_2 - p_3)^2. \tag{1.3}$$

The process is characterized by three different Feynman-like diagrams: s-channel, t-channel and u-channel (shown in figure 1.1). The variable s gives the square of the energy of the reaction ($s = W^2$), and t the square of the momentum transfer. In each diagram the square of the four-momentum of the intermediate particle is described by the corresponding Mandelstam variable, s, t or u respectively.

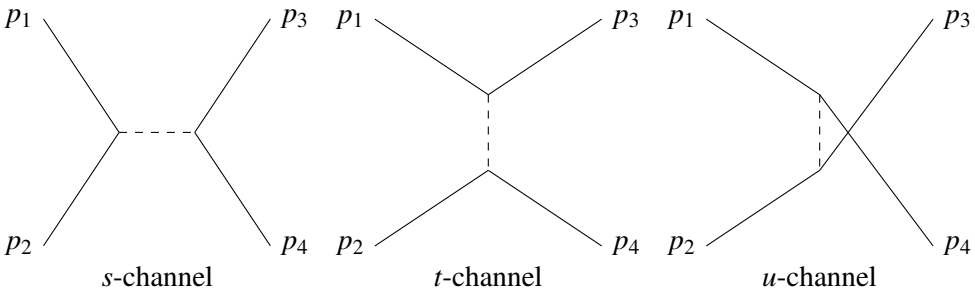

Figure 1.1: s-, t- and u-channel Feynman-like diagrams of a $2 \rightarrow 2$ particle process.

One process to study the nucleon structure and their excited states (resonances), is pion-nucleon scattering. Several models are developed which try to explain this structure of the nucleons. One of these models is the relativistic quark model of [LMP01]. Resonances predicted by this model are shown in figure 1.2. In the lower mass region for every measured resonance a predicted resonance can be found that fits more or less well. In the higher mass region many more resonances are predicted than experimentally observed. Other quark models predict slightly different resonances, but all models have in common that they predict more resonances than experimentally observed. This is called the missing resonance problem.

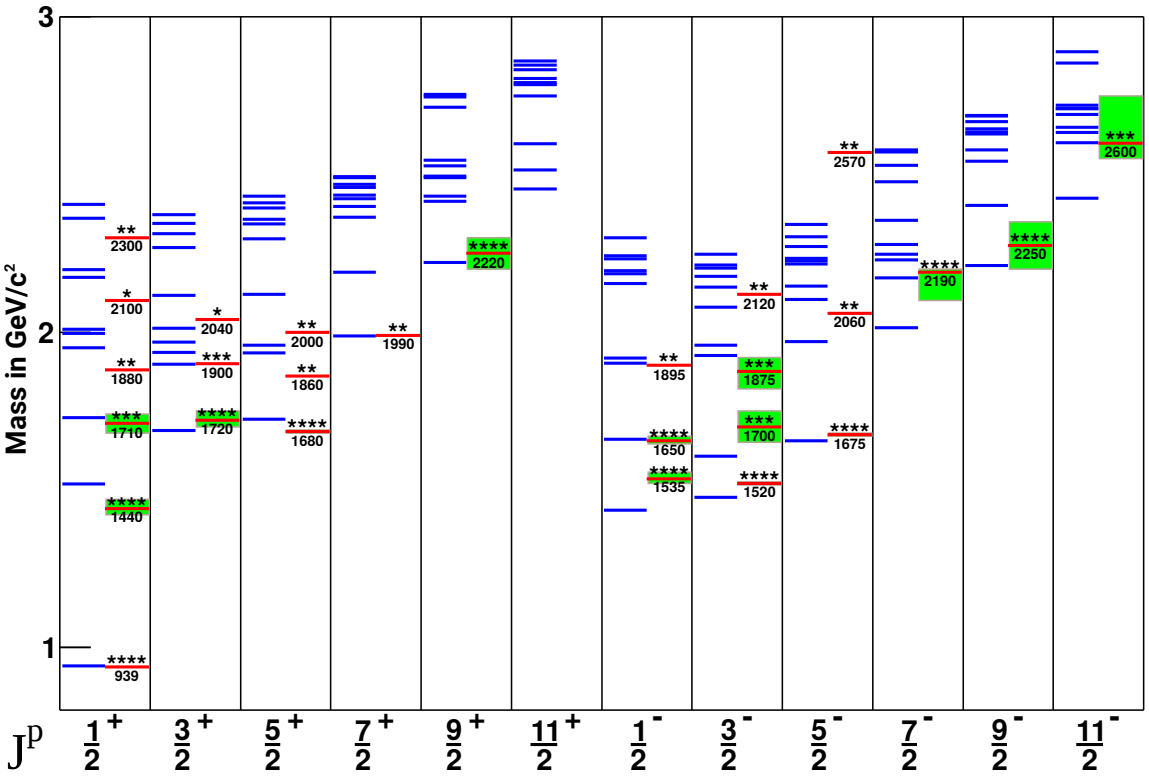

Figure 1.2: Nucleon resonances predicted by the relativistic quark model of Löring et al. [LMP01], ordered by their spin and parity. Blue lines indicate the predicted resonances, red lines with green boxes for their uncertainties indicate the resonances found by experiments so far. The stars indicate how well the experimental results are established. The graphics was taken from [Mül15].

Due to the high cross sections, pion-nucleon (πN) scattering is ideal to investigate the nucleon resonances with high precision. Therefore most of the properties of the currently known nucleon resonances originate from πN scattering experiments. Due to a potential weak coupling of certain resonances to the pion-nucleon channel, some resonances may not be observable in πN scattering.

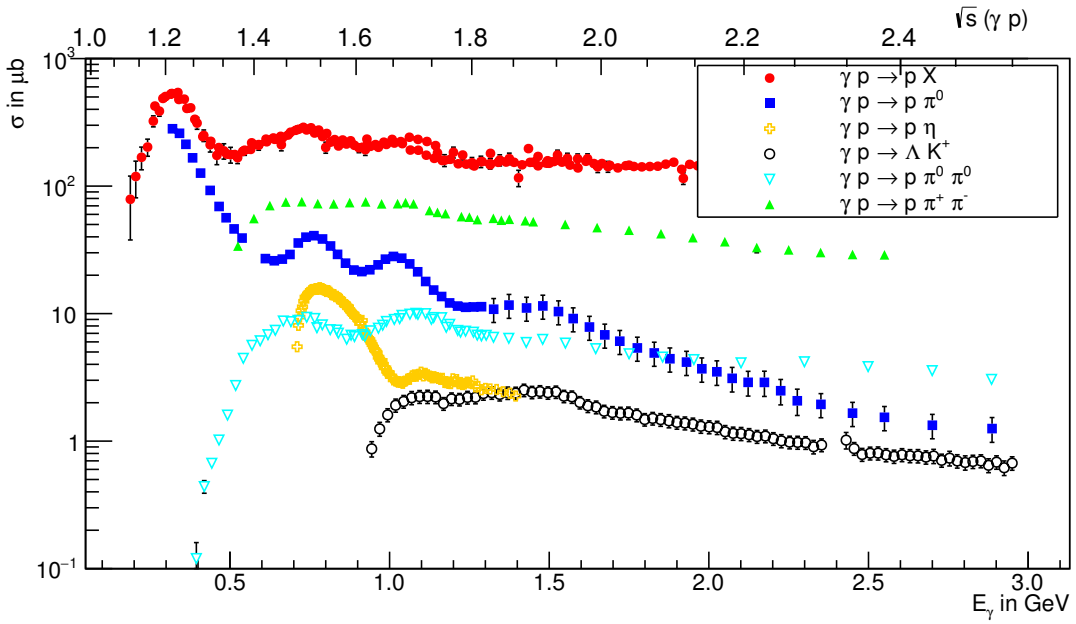

Figure 1.3: The cross sections in photoproduction off the proton. Symbols represent: Red dots total photoproduction cross section [Oli+14], blue squares $\gamma p \to p\pi^0$ [Bar+05], yellow circles $\gamma p \to p\eta$[McN+10], green triangles $\gamma p \to p\pi^0\pi^0$[Fuc05], cyan triangles $\gamma p \to p\pi^+\pi^-$[Wu+05] and black circles $\gamma p \to \Lambda K^+$ [Bra+06].

With photoproduction another production mechanism exists to investigate nucleon resonances. In photoproduction, high energetic photons are absorbed by nucleons and exited nucleon states in coincidence with mesons are produced. In figure 1.3 the photoproduction cross section is shown. Due to the short life time of the excited states, the resonant peaks are very broad and overlapping, and cannot be distinguished from each other in the total photoproduction cross section. In specific reaction channels, e.g. $\gamma p \to p\pi^0$, some peaks show up. In other channels, e.g. $\gamma p \to p\eta$ the shape is completely different. This is caused by the different coupling of the resonances to the different final states. Therefore studying individual channels helps to disentangle the different resonances.

The photoproduction of a single pseudoscalar meson off a nucleon is fully described by four complex amplitudes. The bilinear combinations of these amplitudes can be expressed in 16 experimental observables, shown in table 1.1. Besides the unpolarized differential cross section, there are three single polarization and 12 double polarization observables. These polarization observables depend on one or a combination of the following polarization degrees of freedom:

- polarization of the photon beam, which can be linearly or circularly polarized,
- polarization of the nucleon target, which can be longitudinal or transversely,
- polarization of the recoiling nucleon, which can also be longitudinal or transversely.

The single polarization observables include the beam asymmetry Σ, the target asymmetry T and the recoil polarization P. The 12 double polarization observables are various combinations of beam, target and recoil polarization shown in table 1.1. From these 16 experimental observables, the full angular distribution of eight well chosen ones need to be measured to uniquely determine the four complex amplitudes and perform the so-called complete experiment [CT97]. For these eight observables, the unpolarized cross section, the three single polarization observables and at least four double polarization observables need to be included. The four complex amplitudes are determined from the observables by performing a partial wave analysis (PWA). In the coupled channel approach this is performed not only on a single channel, but on all reaction channels simultaneously, to consider all the available information.

Photon		Target			Recoil			Target-Recoil								
					x'	y'	z'	x'	x'	x'	y'	y'	y'	z'	z'	z'
		x	y	z				x	y	z	x	y	z	x	y	z
Unpolarized	σ	–	T	–	–	P	–	$T_{x'}$	–	$L_{x'}$	–	Σ	–	$T_{z'}$	–	$L_{z'}$
Linearly	Σ	H	P	G	$O_{x'}$	T	$O_{z'}$	$L_{z'}$	$C_{z'}$	$T_{z'}$	G	σ	F	$L_{x'}$	$C_{x'}$	$T_{x'}$
Circularly	–	F	–	E	$C_{x'}$	–	$C_{z'}$	–	$O_{z'}$	–	E	–	H	–	$O_{x'}$	–

Table 1.1: All 16 polarization observables in single pseudoscalar meson photoproduction off a nucleon.

The aim of this thesis is twofold. The first part addresses the production of circularly polarized photons, which gives access to a whole class of double polarization experiments. This requires the knowledge of the absolute electron beam polarization. Therefore the first goal is to build a Møller polarimeter for the BGO-OD experiment, to measure the electron beam polarization. In particular interest for the BGO-OD experiment is the polarization transfer in associated strangeness production ($C_{x'}$ and $C_{z'}$), where one can make use of the self analyzing weak decay of the hyperon to determine its recoil polarization. For all observables a full angular coverage is essential to determine the fundamental amplitudes, but this is not yet achieved even for the differential cross section of the best measured reaction $\gamma p \to K^+\Lambda$. The extreme forward angles are not covered by the existing data. This angular range is not only needed for the PWA, but is also of particular interest for the study of hypernuclei. Therefore the second goal of this thesis is the determination of the differential cross section of the reaction $\gamma p \to K^+\Lambda$ at extreme forward angles, using the Open Dipole spectrometer of the BGO-OD experiment.

To reflect these aims, this thesis is structured as follows:

- Chapter 2 describes the current status in the analysis of the reaction $\gamma p \to K^+\Lambda$.
- Chapter 3 introduces the electron accelerator ELSA and the experimental setup of the BGO-OD experiment. The production of longitudinally polarized electrons at ELSA is also explained, as well as the data acquisition and the initial analysis of the BGO-OD experiment is introduced.
- Chapter 4 describes the production of circularly polarized photon beams from longitudinally polarized electrons beams. Methods to measure the degree of electron beam polarization are introduced and the first measurement of the electron beam polarization with the Møller polarimeter of the BGO-OD experiment are presented.
- Chapter 5 describes the analysis of the reaction $\gamma p \to K^+\Lambda$ at extreme forward angles and presents the measured cross sections.
- Chapter 6 summarizes the results of this thesis and gives a short outlook.

CHAPTER 2

Current Status of $\gamma p \rightarrow K^+\Lambda$

The $K^+\Lambda$ channel received a lot of attention. The self analyzing hyperon weak decay opens the possibility of recoil polarization measurements and the possibility to achieve the complete experiment without the need of a secondary scattering polarimeter. This overcompensates the higher cross section in pionic channels, where such a polarimeter is necessary. In table 2.1 an overview of measured observables is given for the latest experiments. Already in the 50's, 60's and 70's experiments investigated the $K^+\Lambda$ channel, but due to missing polarized photon beams only the observables σ and P could be measured.

Experiment	σ	P	Σ	T	G	H	E	F	O_x	O_z	C_x	C_z	T_x	T_z	L_x	L_z
SAPHIR [Gla+04]	✓	✓														
GRAAL [Lle+07; Lle+09]		✓	✓	✓					✓	✓						
CLAS [McC+10; Bra+07; Pat+16]	✓	✓	✓	✓					✓	✓	✓	✓				
LEPS [Sum+06]	✓		✓													
Crystal-Ball [Jud+14]	✓															

Table 2.1: Overview of published observables of the reaction $\gamma p \rightarrow K^+\Lambda$ measured by different experiments.

The CLAS collaboration has also high statistics data available for the analysis of all remaining observables [Ire16]. Therefore it is expected that in the next years all observables in this channel will be determined. To finally determine the four complex amplitudes, beside the measurement of enough observables, also a full angular coverage is essential.

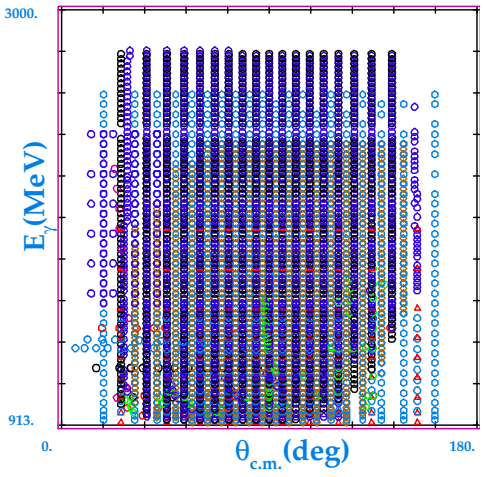

Figure 2.1: Data available in the SAID database [ASW03] for the differential cross section of the reaction $\gamma p \rightarrow K^+\Lambda$, Each point represents a published measurement in $\Theta^{c.m.}_{K^+}$ and E_γ. The different colors represent different publications.

In figure 2.1 the angular coverage of the most simple observable, the differential cross section, σ, is shown by the data available in the SAID database [ASW03]. The angular range of $\Theta_{K^+}^{c.m.} = 20°$ to 160° is covered by several data sets, but the forward and backward region is not. In addition in the region already covered by the experiments, the data does not agree within their errors. In figure 2.2 the total cross section, measured by the SAPHIR, CLAS and LEPS experiments are shown. Discrepancies between the data sets are obvious.

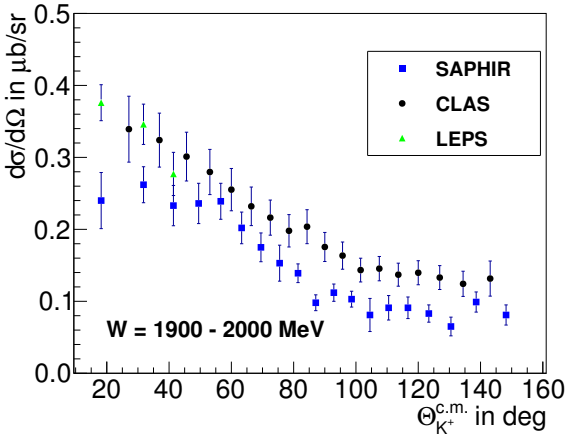

Figure 2.2: Differential cross section data from SAPHIR [Gla+04], CLAS [McC+10] and LEPS [Sum+06] for the center of mass energy $W = 1\,900$ MeV to $2\,000$ MeV.

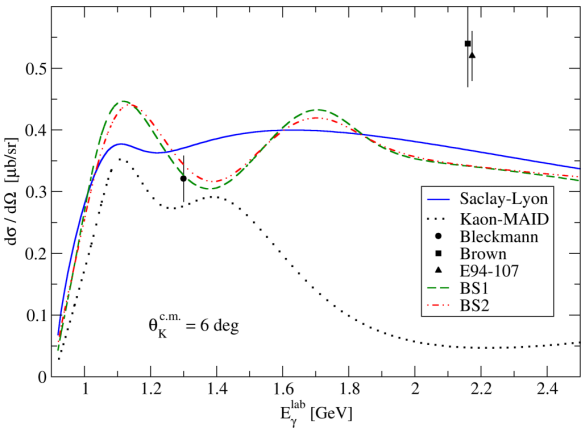

Figure 2.3: Available differential cross section data for $\Theta_{K^+}^{c.m.} = 6°$, from [Ble+70], [MA10] and [Bro+72], together with predictions from the Saclay-Lyon isobar model [Dav+96], the kaon-MAID tree-model [Lee+01] and two isobar models from [SB16]. Figure taken from [SB16].

Also the very forward region of the cross section is very important. Due to the dominant t-channel contribution in this reaction, this angular range is very important to constrain different models. In figure 2.3 different available models are shown for $\Theta_{K^+}^{c.m.} = 6°$. At this angle the only available data point from photoproduction is from the 70s [Ble+70], the other two data points are from electro-production with very low momentum transfer. As models the Saclay-Lyon isobar model [Dav+96], the kaon-MAID tree-model [Lee+01] and two isobar models from [SB16] are shown. Apart from the steep rising of the cross section close to threshold, all models predict completely different behavior. To further constrain the models, especially in the extreme forward angular region, more experimental data is needed. This can be provided by the BGO-OD experiment, which will be introduced in the following chapter.

CHAPTER 3

The BGO-OD Experiment

The BGO-OD experiment is a hadron physics experiment located at the Electron Stretcher Accelerator (ELSA) at the physics institute of the University of Bonn. This chapter describes the electron accelerator ELSA in section 3.1, the BGO-OD experiment in section 3.2 and explains how the obtained data is prepared for the further analysis in sections 3.3 and 3.4.

3.1 ELSA - Electron Stretcher Accelerator

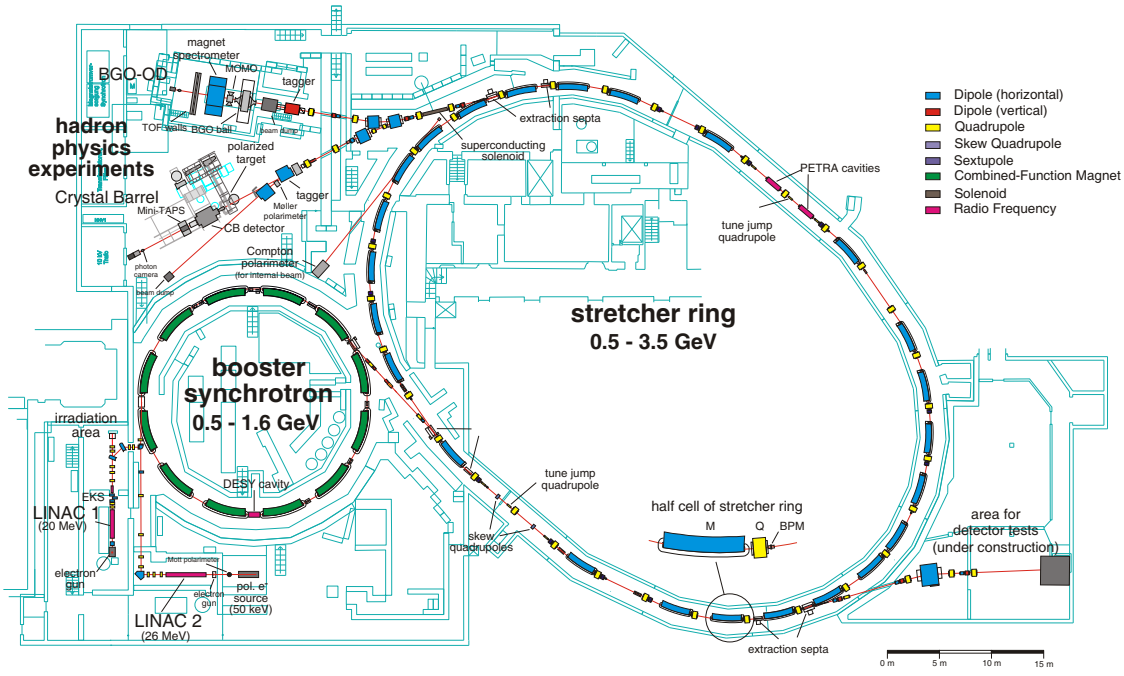

Figure 3.1: Schematic drawing of the ELSA electron accelerator facility [ELS].

ELSA, shown in figure 3.1, is a three stage electron accelerator. The electrons are produced using a polarized or unpolarized electron source at the electron gun situated at the beginning of LINAC 1 and 2 respectively (bottom left of figure 3.1). For unpolarized electron beams, the electrons are produced in a thermionic gun via photoemission [Hil00] and preaccelerated to 50 keV or 90 keV [Kla11], depending on which linear accelerator will be used. Polarized electrons are produced via photoemission from a

Superlattice-GnAs crystal [Hil00]. A description of the techniques used to extract polarized electrons is presented in section 3.1.1.

In the first stage of the accelerator, the produced electrons are accelerated in one of the linear accelerators (LINAC 1 and 2) up to 20 MeV or 26 MeV respectively (bottom left of figure 3.1)[1]. The electrons accelerated by the Linac are injected into the booster synchrotron. The booster synchrotron is a circular accelerator with combined function magnets (shaded green on figure 3.1) to provide dipole magnetic fields for the electron beam curvature and quadrupole fields for beam focusing in both the horizontal and vertical plane. The beam is kept on a circular orbit and accelerated repeatedly by one accelerator cavity up to an energy of 1.6 GeV. To keep the electrons on the circular orbit, the magnetic field is ramped accordingly. In the usual operation mode however the electrons are transferred to the next stage, the stretcher ring, at an energy of 1.2 GeV. The stretcher ring is comprised of an oval of dipole magnets to keep the beam on orbit, quadrupole magnets for beam focusing and sextupole magnets for higher order corrections. The electrons are then accelerated up (or even down) to their desired energy, which can be up to 3.5 GeV with the stretcher ring achieving stored electron currents of up to 20 mA [Sch15b]. Usually the maximum energy used for the hadron physics experiments is 3.2 GeV. After the electrons are accelerated to their desired energy, they are slowly extracted to the BGO-OD experimental area. The desired current for the BGO-OD experiment is around 1 to 2 nA to avoid saturation of detector signals and extensive dead time of the data acquisition. Therefore only a part of the stored beam in the stretcher ring is extracted to the experiments via resonance extraction [Gen99]. Through the extraction beam line, the beam line part between the stretcher ring and the experimental areas, seen in the upper left part of figure 3.1, the beam is then delivered to the hadron physics experiments. Due to this design ELSA always runs through a cycle of: injection, acceleration and extraction, where a complete cycle takes usually about 6 s. One extraction phase, also called a spill, usually takes around 5 s. Where the time for injection and acceleration sums up to about 1 s, so that the macroscopic duty-cycle (duty-cycle $= \frac{t_{extraction}}{t_{injection}+t_{acceleratrion}+t_{extraction}}$) is around 83 %. During the extraction phase the electron beam has a microscopic duty-cycle of 100 % (continues wave beam).

3.1.1 Production of Polarized Electron Beams

At the polarized electron source, polarized electrons are produced by optical pumping of a GaAs (Gallium Arsenide) crystal. The topmost energy levels of the valence band in GaAs are in a P state, the conduction band is in a S state. Due to the spin-orbit coupling, the $P_{3/2}$ state is four times and the $P_{1/2}$ state two times degenerated as shown in figure 3.2. The relative transition amplitudes are given in figure 3.2 by the circled numbers. When pumping the crystal with circularly polarized light, the magnetic moment has to change by ± 1 due to angular momentum conservation.

When using laser light with an energy of $\hbar\omega = 1.42\,\text{eV}$, which corresponds to the band gap between the $P_{3/2}$ state and the conduction band, one gets a degree of polarization, P, as given in equation 3.1. Where $N_{m=+1/2}$ and $N_{m=-1/2}$ are the relative transition amplitudes.

$$P = \frac{N_{m=+1/2} - N_{m=-1/2}}{N_{m=+1/2} + N_{m=-1/2}} = \frac{1-3}{1+3} = -0.5 \tag{3.1}$$

Canceling the degeneration of the energy levels, by using a superlattice crystal, increases the degree of polarization to around 70 % [Hil00]. Due to the photoemission process used to produce the polarized electrons at the electron source, the spin of the electrons is longitudinal, and therefore orthogonal to the magnetic field of the dipole magnets used to keep the electrons on a circular orbit during the acceleration

[1] Currently only Linac 2 is operational

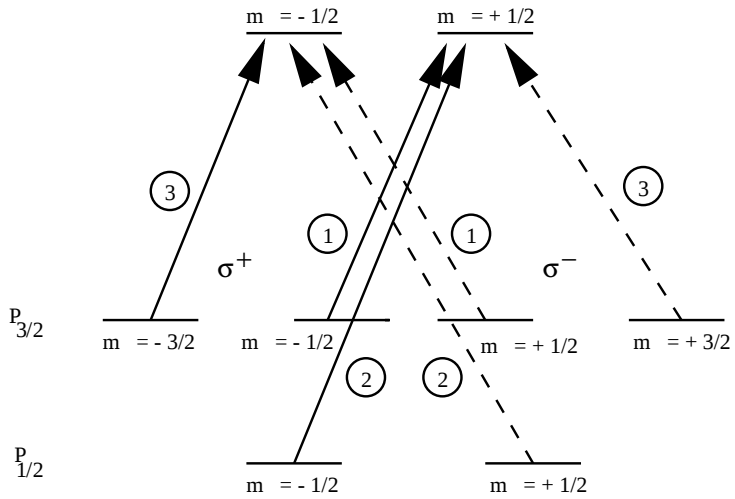

Figure 3.2: Possible transitions in GaAs, depending on chirality the laser light (solid and dashed lines). Relative transition amplitudes are given by the circled numbers. Figure taken from [Hil00].

in the booster synchrotron and the stretcher ring. This would cause a precession of the electron spin. Horizontal magnetic fields would increase the cone of spin precession. When horizontal magnetic fields occur repetitive in the same direction, this causes a loss of the electron polarization. To avoid this the electron beam is deflected, using electric fields, directly after the production at the electron source [Hil00]. The electrons produced at the electron source are non-relativistic so the relativistic effect of spin-orbit coupling can be neglected and therefore this results in an effective rotation of the electron spin to the transverse direction. A change of the momentum vector of the electron does therefore not change the spin vector. Deflecting the beam by 90° results in nearly full polarization transfer from longitudinal to transverse direction (orthogonal to the acceleration plane, parallel to the direction of the magnetic fields of the dipole magnets).

The linac structure is also penetrated by solenoid magnetic fields. To compensate the effect of these fields the direction of the electron spin can be corrected with pairs of solenoid magnets mounted in the transfer beamline between the Linacs and the booster synchrotron.

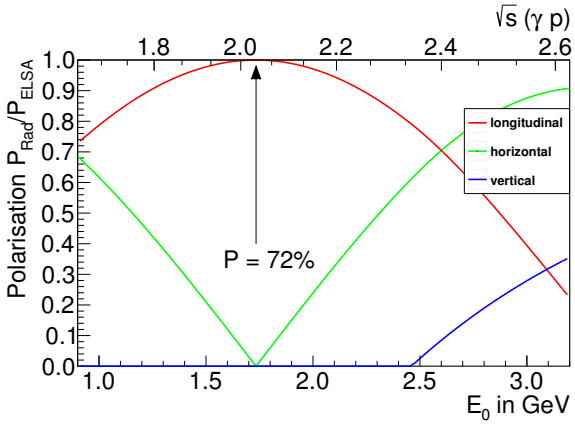

Figure 3.3: Dependency of the electron beam polarization at the experiment P_{Rad} in parts of the polarization in ELSA P_{ELSA} as function of electron beam energy E_0, or alternatively the center of mass energy $\sqrt{s}$, assuming a bremsstrahlung photon is produced which is in turn incident upon a target nucleon. [Hof01]

In the extraction beamline, the spin is rotated again with a superconducting magnet by 90° around the direction of motion. Due to spin precession caused by the remaining dipole magnets in the beam line, the spin rotates again in the accelerator plane. The angle of this rotation depends on the energy of the electron beam. The resulting polarization components as a function of the electron beam energy is shown in figure 3.3. Up to 2.45 GeV only longitudinal and horizontal polarization components occur. As the spin is totally rotated from vertical to horizontal direction by the superconducting solenoid magnet, after precession the spin is still oriented in the horizontal plane. At an energy of 1.73 GeV, the vertical polarization in ELSA is fully transferred into longitudinal polarization at the BGO-OD experiment [Hil00]. Therefore the degree of longitudinal polarization is maximal, and given by the maximum degree of polarization the polarized source of ELSA can provide, which is 72 %. At a beam energy of more than 2.45 GeV, the field integral of the solenoid magnet is no longer sufficient to fully rotate the electron spin completely from vertical to horizontal orientation and a vertical component remains.

3.2 BGO-OD Experiment

The BGO-OD experiment, shown in figure 3.4, is located in one of the two experimental areas for hadron physics experiments at ELSA. It performs photoproduction experiments off nucleons with a real photon beam. The photon beam is produced from the electron beam of ELSA by bremsstrahlung as described in section 3.2.1.

The BGO-OD experiment itself consists mainly of two parts: the central calorimeter with the **BGO**-ball (described in section 3.2.3) and a forward spectrometer around the **O**pen-**D**ipole magnet (described in section 3.2.4), which are also the eponymous components of the experiment. The coordinate system used in the experiment has its z-axis along the photon beam, the y-axis pointing to the top and the x-axis to the left, when looking downstream the photon beam. Liquid hydrogen, liquid deuterium or solid state targets, such as carbon, are available for use.

3.2.1 Photon Tagging and Monitoring

Photoproduction experiments require a real photon beam. At the BGO-OD experiment the photon beam is produced by bremsstrahlung from the electron beam provided by ELSA off of different kind of radiators. Depending on the radiator and the electron beam polarization, it is possible to produce polarized or unpolarized photon beams. By using the tagging system described in this section, it is possible to determine (or "tag") the energy and time of every single produced photon. The flux monitoring system, installed at the end of the experiment, counts the total photon flux on the target of the experiment, which is important for absolute cross section measurements.

Goniometer & Radiators

The radiators used to produce bremsstrahlung are mounted on a goniometer system shown in figure 3.5. All, except for the Møller radiator are attached to a radiator plate. The goniometer system can move the radiator plate in x- and y-directions, as well as rotate it around the beam, the horizontal and the vertical axis. The Møller radiator is mounted in a solenoid magnet and can only be moved in the x-direction and rotated around the vertical axis. The different available radiators are listed in table 3.1. Available are a thin diamond radiator for the production of linearly polarized photon beams via coherent bremsstrahlung, as described in the diploma thesis of A. Bella [Bel11], several amorphous radiators for the production unpolarized photon beams, also used to normalize the coherent bremsstrahlung spectrum

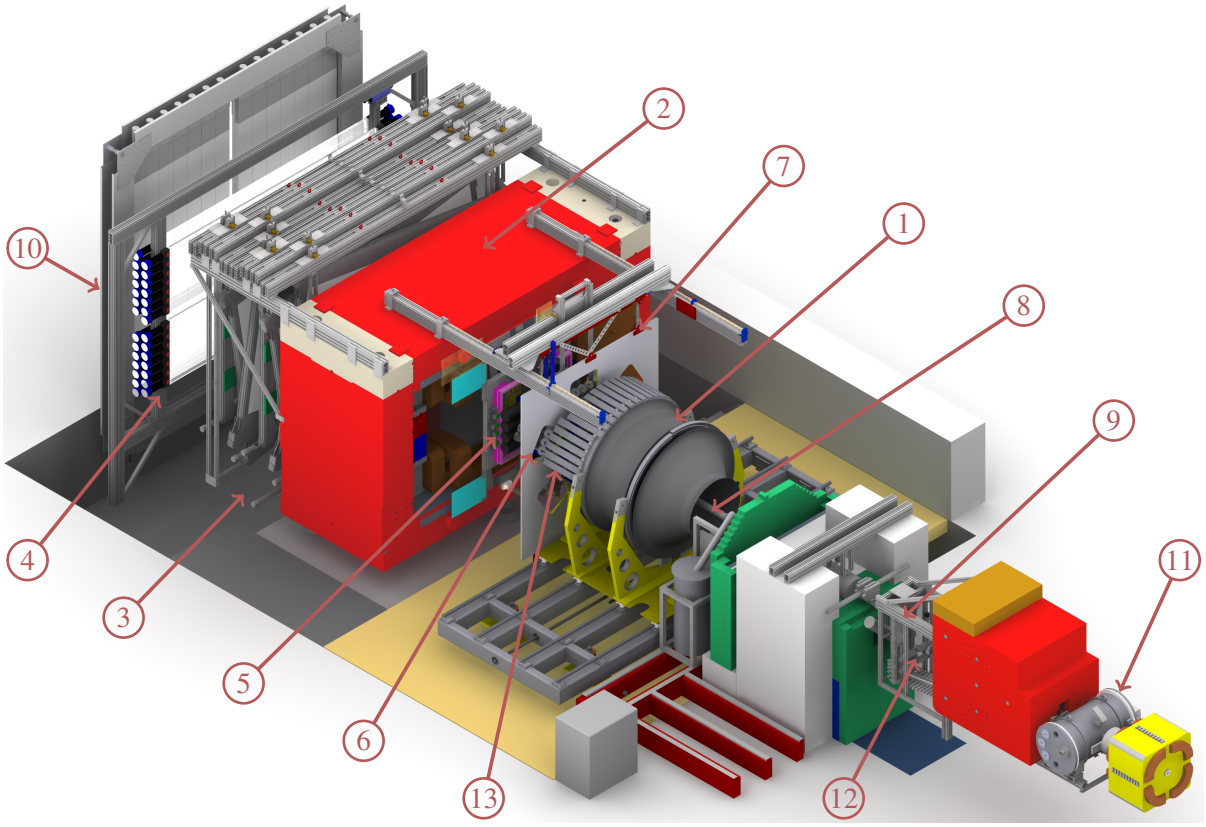

Figure 3.4: CAD drawing of the experimental setup of the BGO-OD experiment. The numbered circles label the following detectors: (1) BGO-Ball + Scintillator Barrel + MWPC, (2) Open Dipole Magnet, (3) Drift chambers, (4) TOF-walls, (5) SciFi2, (6) MOMO, (7) Daisy, (8) Cryotarget, LH_2 or LD_2, (9) Tagging detector, (10) Photon Flux Monitor, (11) Goniometer, (12) Møller detectors, (13) SciRi.

and several other radiator for diagnostic purposes. For the production of bremsstrahlung, thin radiators are used to avoid multiple scattering.

Radiator	Material	Thickness	Function
Cromox screen	Cromox	1 mm	Electron beam diagnostics
Copper 50	*Cu*	50 µm	Unpolarized photon beam
Copper 67	*Cu*	67 µm	Unpolarized photon beam
Copper 100	*Cu*	100 µm	Unpolarized photon beam
"Empty radiator"	-	-	Background studies
Capton foil	Capton	125 µm	Low rate unpolarized photon beam
Vertical wire	Steel guitar string	0.4 mm	Horizontal electron beam alignment
Horizontal wire	Steel guitar string	0.4 mm	Vertical electron beam alignment
Diamond	Diamond	560 µm	Linear polarized photon beam ([Bel11])
Møller foil	Vacoflux 50	20 µm	Circular polarized photon beam

Table 3.1: List of available radiators.

As part of this thesis, the goniometer system was extended by the inclusion of the Møller radiator for the Møller polarimeter as described in chapter 4.5.3 and appendix B.

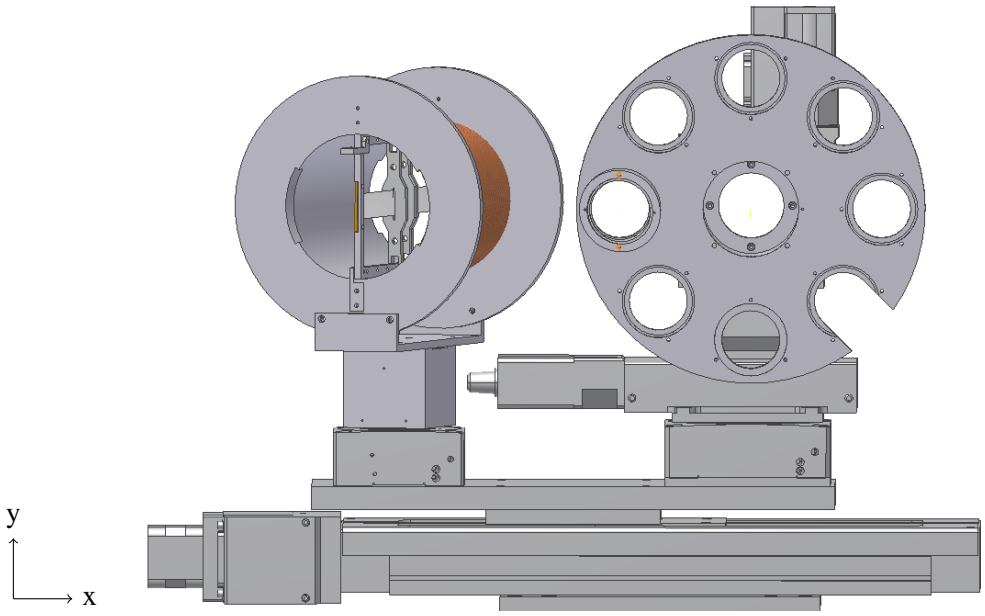

Figure 3.5: Schematic drawing of the goniometer system. Left Møller radiator with solenoid magnet, right radiator plate.

Tagging System

Every photon generated at the radiator requires an energy and time to be assigned to it. The tagging system composed of the tagging magnet and tagging detector is used for this. While producing a photon via bremsstrahlung in the radiator, a certain amount of energy is transferred from the electron to the produced photon. In the case of a single scattering event, the resulting energy of the post-bremsstrahlung scatted electron (E_{e^-}) is:

$$E_\gamma = E_0 - E_{e^-} \tag{3.2}$$

Where E_0 is the primary beam energy given by the electron accelerator, and E_γ is the energy of the resulting photon.

The tagging magnet is a dipole magnet with a horizontal magnetic field. Due to the Lorentz force the scattered electrons are deflected downwards and the deflection angle depends upon the momentum of the electron. From the detection position in the tagging detector, the energy, E_{e^-}, of the post-bremsstrahlung electron can be determined. The primary electron beam (black line in figure 3.6) with energy E_0 hits the radiator in the goniometer chamber. A fraction of the electrons in the beam undergo bremsstrahlung in the radiator and loose energy. The electrons are deflected in the magnetic field of the tagging magnet and hit the tagging detector, which determines their energy E_{e^-} from the position of the hit detector channel. Electrons which did not undergo bremsstrahlung pass the tagging detector above the top most channel and their energy is not recorded. The photons produced by bremsstrahlung (blue line) with an energy of $E_\gamma = E_0 - E_{e^-}$ pass the magnet undeflected and go straight to the experiment. In front of the tagging detector the ARGUS detector is mounted, to increase the energy resolution of the tagging system, and the detectors of the Møller polarimeter which are described in section 4.5.4. With this system it is possible to determine the energy of the electron by measuring the deflection angle.

The tagging detector consists of 120, 5 mm thick, plastic scintillator bars (EJ-204 [Elj]) mounted in a hodoscope. Every scintillator overlaps with the adjacent scintillators by 55 % and is oriented such that the scintillator surface is perpendicular to the electron trajectory. This ensures an electron always hits

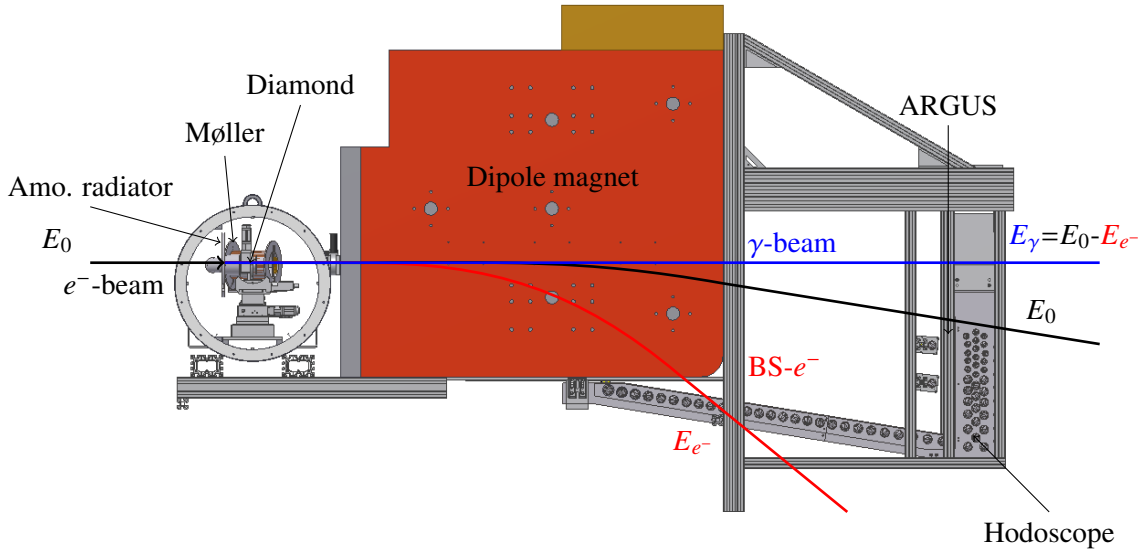

Figure 3.6: Illustration of the tagging principle.

2 or 3 scintillators. The scintillators cover a range of electron energies of 10 % to 90 % of the primary beam energy, E_0. Each scintillator is attached to a photomultiplier tube (PMT). Three different kinds of PMTs are used, Hamamatsu R7400U and R9880U-110 [Hama] for the 33 channels with the highest expected rate, and ET Enterprises 9111B [ET] for the remaining channels. To further process the signals they are discriminated by dual threshold discriminators, called B-Fred [Mes15], especially developed for this detector. The discriminated signals are then recorded by jTDCs, which are time to digital converter (TDC) implemented in an field-programmable gate array (FPGA), which was developed at the BGO-OD experiment and provides 30 ns time resolution [SB14; Bie16]. With this setup the detector achieves a time resolution of up to 150 ps [Mes15]. A good time resolution of this detector is very important for the experiment, because it provides the start time for the recorded events and therefore serves as start detector for the time of flight measurements. The energy resolution is not equal along all channels and depends on the electron energy. For low energy electrons, which correspond to high energy photons, the energy resolution is 0.5 % of E_0 and decreases to 2.1 % of E_0 for the highest electron energies, which corresponds to the lowest photon energies.

ARGUS

To improve the energy resolution of the tagging system, an additional detector (ARGUS) is installed in front of the part of the tagging detector with lower energy resolution [Ale15; Rei15]. ARGUS is a scintillating fiber detector with 480 2 mm diameter fibers in three layers. It covers the energy range of 30 % to 66 % of E_0. The fibers are connected to 16 channel PMTs[2] and the signals are processed by jDisc modules. The jDisc module is a jTDC, in combination with a time over threshold (ToT) discriminator module as input [Bie13]. The time resolution of ARGUS is 400 ps, which is sufficient to correlate the hits in the tagging detector with those from ARGUS. Due to the narrow diameter of the fibers, ARGUS achieves an energy resolution of 0.08 % to 0.45 % of E_0, which is about four times better than the energy resolution of the tagging detector. For data analysis it is possible to use the time measured by the tagging detector and the energy information of ARGUS.

[2] Hamamatsu H6568

Flux Monitor

When determining an absolute cross section it is essential to know the absolute photon flux. The cross section is proportional to the number of reactions per number of incoming photons. The expected integrated rate over all channels of the tagging detector is up to 50 MHz. Not all of the tagged photons will reach the target, as the photon beam is collimated between the tagging system and the target. Collimation is needed to increase the effective degree of linear polarization. As coherent bremsstrahlung for linear polarization is only produced together with incoherent bremsstrahlung, the effective degree of linear polarization is increased by suppressing the incoherent part. This is possible because the opening cone of incoherent bremsstrahlung is larger than the one of coherent bremsstrahlung. Therefore by collimation more of the incoherent bremsstrahlung is cut away, which increases the effective degree of linear polarization [Bel16]. Still more than 25 MHz are expected to reach the target, even after collimation. The method of determining the photon flux at the BGO-OD experiment is as follows: The number of photons is not determined directly, but instead the fraction of photons detected by the tagging detector reaching the target is determined. This fraction (P_γ) is called the photon definition probability and is determined run wise with the FluMo detector.

The FluMo detector uses electron-positron pair-production to measure a defined fraction of the photon beam. By knowing the fraction of photons counted by the FluMo detector it is possible to determine P_γ:

$$P_\gamma = \frac{\text{\# of hits in FluMo / photon efficiency}}{\text{\# of hits in tagging detector}}, \tag{3.3}$$

where photon efficiency represents the conversion probability of photons to electron-positron-pairs in front of the FluMo detector. With this method it is also possible to determine P_γ as a function of the photon energy ($P_\gamma(E_\gamma)$) by looking for coincident hits in the FluMo detector and in the individual channels of the tagging detector. The FluMo detector itself consists of 3, $7 \times 7\,\text{cm}^2$, 5 mm thick plastic scintillators (EJ-204 [Elj]). These scintillators are connected to ET Enterprises 9111B PMTs [ET] via light guides. Currently only the two further downstream scintillators are used. The threshold of these two is set such that only events where two charged particles hit each scintillator are counted. With the assumption that these two charges, close to the photon beam, must be produced by pair production from a beam photon somewhere in the experiment. As the amount of material in the photon beam does not change during the datataking, the number of detected pairs is proportional to the photon flux.

The photon efficiency, which is needed to determine the value of P_γ, is determined in dedicated runs during the data taking. In these runs, an additional detector (Gamma Intensity Monitor (GIM)) is moved behind the FluMo detector. The GIM is a total absorbing detector, which counts every single photon. It consists of a $6.5 \times 6.5 \times 30\,\text{cm}^3$ lead glass block attached to a fast PMT (Hamamatsu R2083 [Hamc]) and can count rates up to 4 MHz reliably [Zim12]. For higher rates the detected rate saturates and is no longer reliable. These dedicated runs are therefore performed at lower rates than normal data taking, typically the rate in the GIM detector in these runs is about 500 kHz. From the photons that have been seen by the GIM, the fraction seen by the FluMo can be determined. This fraction directly corresponds to the photon efficiency. By requiring the photons seen in the GIM are coincident with electrons in the tagger, the photon efficiency can even be determined in dependence of the photon energy.

With the photon efficiency determined with the GIM, P_γ determined with FluMo and the produced photons measured by the tagging detector, the photon flux at the target can be determined.

3.2.2 Nucleon Target

The targets, used for the photoproduction experiments, are located in the center of the central calorimeter. The liquid hydrogen or deuterium target cell is contained in a vacuum pipe. The cell is a aluminum cylinder with 4 cm diameter and has a length of 6 cm. It is closed with thin capton windows on both sides. The target area density of the liquid hydrogen target is $2.538 \times 10^{-7}\,\mu b^{-1}$. The current carbon target is a graphite cylinder of 3 cm diameter and available with a length of 2 and 3 cm. To position the carbon target in the middle of the central calorimeter, the complete structure of the liquid hydrogen/deuterium target is moved out of the central calorimeter, and instead a plastic tube, which carries the carbon target, is inserted.

3.2.3 Central Calorimeter

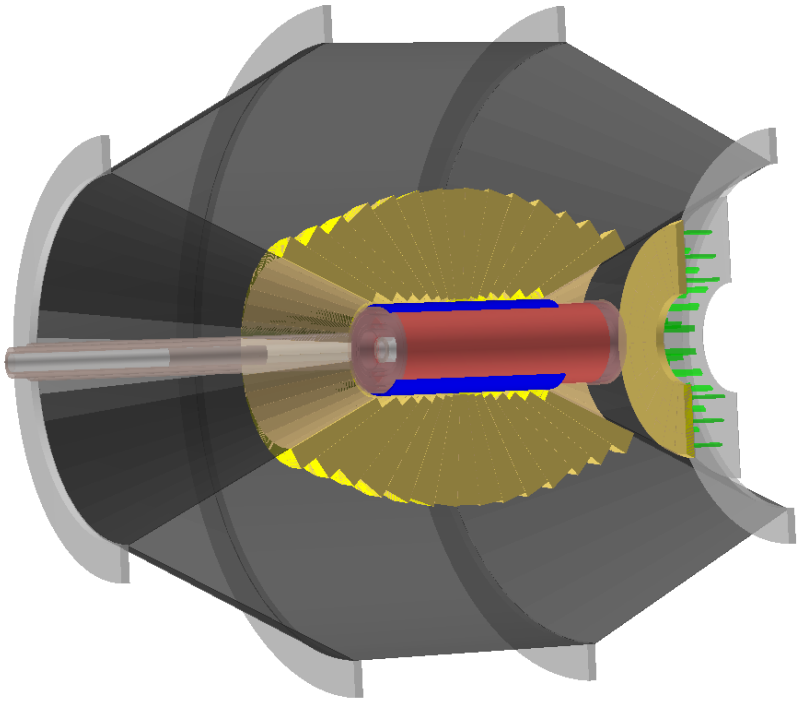

Figure 3.7: Drawing of the central calorimeter from the geometry description used in the Monte-Carlo simulation of the experiment. In black the carbon fiber holding structure of the BGO-ball is shown and in yellow one half of the BGO crystals. Part of the scintillator barrel for charged particle identification is shown in blue, and in red the two cylindrical multi wire proportional chambers (MWPCs) are shown with the target structure in their center. In the right opening cone of the BGO-ball holding structure, the SciRi detector is shown in yellow and green which is described in section 3.2.5.

The central calorimeter (see figure 3.7), surrounds the target, and mainly consists of the BGO-Ball, a crystal calorimeter of 480 Bismuth Germanate ($Bi_4Ge_30_{12}$ or BGO) crystals, shaped in the form of a rugby ball. Between target and BGO-ball, two cylindrical MWPCs are positioned to improve the vertex resolution for reactions where charged particles are produced, and a scintillator barrel with 32 bars of plastic scintillators aids charged particle identification.

BGO-Ball

The BGO-Ball, originally built for the GRAAL experiment [Ghi+98b], is a rugby-ball shaped electromagnetic calorimeter, covering a polar angular range of $25° < \Theta < 155°$ and all azimuthal angles, Φ. The 480 BGO crystals, each covering the same solid angle, have a depth of more than 21 radiation lengths. The crystals are arranged in 15 crowns. Each crown consists of 32 BGO crystals and covers 12° in Θ.

All 480 crystals are read out by PMTs and the siganls are processed by sampling analog to digital converters (SADCs) [3]. In the signal path, one "mixer" is included for every crown, which has adjustable attenuators integrated and provides an analog sum signal of all connected channels. This signal can be used as a trigger signal for the data acquisition (DAQ) to acquire the data only if enough energy was deposited in the BGO-ball, as described later in section 3.3. The SADC samples the signal of the PMT with a sample rate of 160 MHz. It has an integrated feature extraction which can be used to only acquire the relevant data, which in this case is the pulse integral and the start-time of the signal. With this combination, a relative time resolution of 2 ns is achieved and an energy resolution of 3 % at E_γ = 1 000 MeV [San+96]. This makes the BGO-ball ideal for neutral meson detection when decaying to photons, e.g. $\pi^0 \to \gamma\gamma$.

Scintillator Barrel

The scintillator barrel is included to distinguish charged from uncharged particles in the central calorimeter. It consists of 32, 5 mm thick, plastic scintillator bars made from Bicron (now Saint-Gobain) BC448 [Sai]. Each bar is connected to a Hamamatsu H3164-10 PMT [Hamb, p. 80] and read out by one jDisc module. Plastic scintillator has a high detection efficiency for charged particles of nearly 100 %. Photons have only a small probability of less than 1 % [4] to interact with the scintillator and produce a signal. Therefore it is ideally suited to distinguish charged and uncharged particles. A coincidence between the BGO-ball and the scintillator barrel in both azimuthal angle Φ and time t is used to identify hits of charged particles in the BGO-ball. Therefore charged particles can be very well distinguished from photons.

By the amount of energy deposited in the scintillator it is also possible to also distinguish protons from charged pions as described later in section 3.4.4.

MWPC

Two multi wire proportional chambers (MWPCs) are installed between target and scintillator barrel. These detectors consist of two coaxial cylindrical cathodes each, centered around the target. Each cathode is divided in 4.5 mm wide strips which are coiled helical at an angle of ±45°. In the 8 mm gap between the cathodes, 20 µm anode wires are placed parallel to the cylinder axis, 2 mm apart from each other. The exact dimensions of both chambers are shown in figure 3.8 and table 3.2a.

The gap between both cathodes is filled with a gas mixture of 69.5% Argon, 30% Ethan and 0.5% Halocarbon 14 (CF_4). Charged particles traversing this gap will produce an electron avalanche in the high electric field close to the anode wires. The electrons and ions drifting to the cathode and anode will produce measurable signals on the strips and wires. All signals are amplified by preamplifiers close to the chamber and further processed by the read out electronics. Anode wire signals are processed with

[3] W-IE-NE-R AVM16 [WIE]

[4] $P = 1 - e^{5\,\mathrm{mm}/\lambda}$ where λ is the mean free path, which is around 55 cm for carbon [Oli+14].

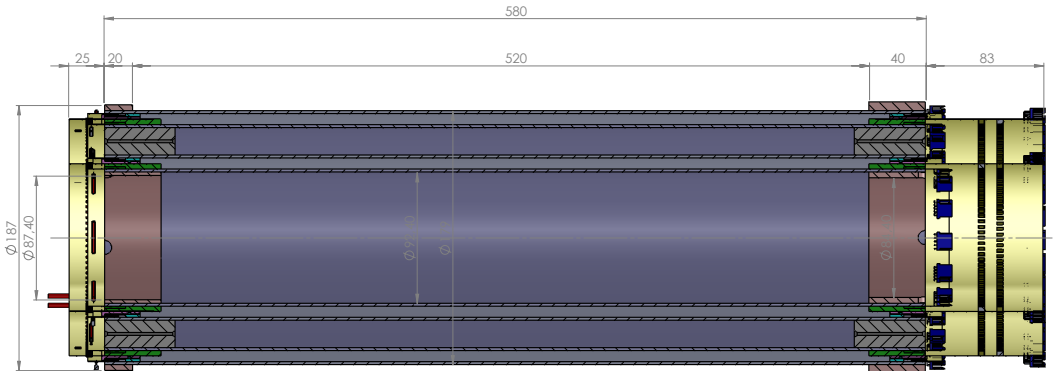

Figure 3.8: Schematic drawing of a cut through the two cylindrical MWPCs chambers, with dimensions in mm. In blue the inner cathode is shown. Figure taken from [Mes14, (Original author: A.Braghieri, INFN sez. di Pavia)].

	Inner Chamber	Outer Chamber
Length	520 mm	520 mm
Inner Radius	48.2 mm	79.5 mm
Outer Radius	56.2 mm	87.5 mm
Number Wires	160	256
Number of inner Strips	48	80
Number of outer Strips	56	88

(a) Dimensions of both MWPC chambers

	Resolution
Δz	300 µm
$\Delta\Phi$	2°
$\Delta\Theta$	1°
Θ coverage	8° to 163°

(b) Resolution of the combined MWPC detector

Table 3.2: Information about the cylindrical MWPC of the BGO-OD experiment from [Lei14]

jDisc modules, the cathode stripe signals are processed with the same type of SADCs as the signals of the BGO-Ball[5].

The achievable resolution and angular coverage of the MWPC detector is summarized in table 3.2b. At the time of writing this thesis the detector is being commissioned. Using this detector in future data taking periods will improve the reconstruction of the vertex of a reaction and will enable the experiment to reconstruct secondary vertices.

3.2.4 Forward Spectrometer

The second main part of the BGO-OD experiment is the magnetic forward spectrometer. It is centered around the large open dipole magnet, which is the second eponymous component of the experiment. It covers forward angles ($\Theta^{lab} < 10°$) and is used to reconstruct charged particle four-momenta. The magnetic field of the magnet, with an integrated field strength of up to ~0.5 T m, causes the trajectory of a charged particle to curve in the x-y plane. With two scintillating fiber tracking detectors (MOMO and SciFi2) in front of the magnet, and driftchambers behind the magnet, the trajectory of a charged particle through the magnetic field can be determined. From the curvature of the trajectory and the time of flight (TOF), measured with the TOF-walls, energy, momentum, charge and mass of the particle can be determined, as described later in section 3.4.6.

One example event from simulation is shown in figure 3.9. The proton, coming from the target, is detected by the detectors in front of the magnet, then deflected in the magnetic field and detected by the

[5] W-IE-NE-R AVM16 [WIE]

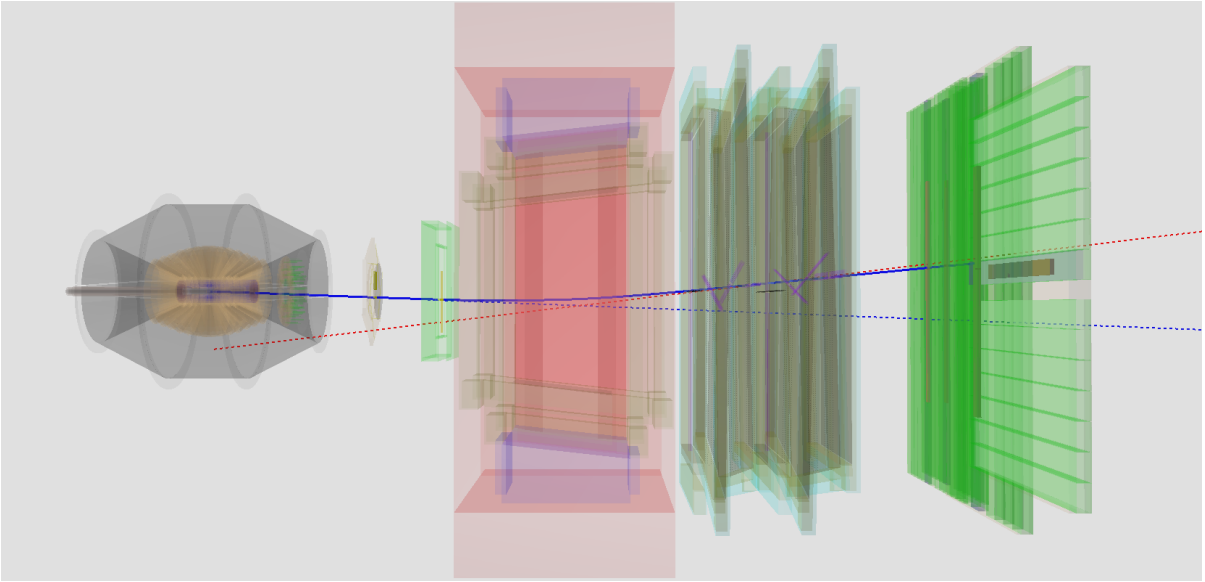

Figure 3.9: Simulated proton traversing through the forward spectrometer. On the left side the BGO crystals surounding the target are shown, with the SciRi detector in the opening cone. Right from the BGO-ball the MOMO and the SciFi2 detector is shown. In the center the spectrometer magnet is shown in red. On the right side of the magnet the eight driftchambers and four TOF walls are shown. The proton, indicated in cyan, originates from the target. It crosses MOMO and SciFi2, enters the magnetic field, where it is defelected and crosses the driftchambers and the first TOF wall. It is stopped in the second TOF wall.

detectors behind the magnet.

Beam photons which did not interact with nucleons in the target also pass through the forward spectrometer. Therefore all detectors in the forward spectrometer have a blind spot in the middle to let the photon beam pass through, corresponding approximately to a polar angle of $\Theta^{lab} = 0°$ to $1°$.

The angular range covered by the magnetic spectrometer is $\Theta^{lab} = 1°$ to $8°$ in vertical and $\Theta^{lab} = 1°$ to $12°$ in horizontal direction. The momentum resolution of the spectrometer, determined from simulation, is 1.4 % at full magnetic field (0.431 T), and 3 % at half magnetic field (0.216 T).

MOMO

The first tracking detector in front of the spectrometer magnet is the scintillating fiber detector, MOMO. MOMO was build for the MOMO experiment at COSY [Bel+99; Bel+07] and consists of six modules of 112, 2.5 mm scintillator fibers each. The six modules are arranged in 3 layers with 2 modules each and the layers are rotated 120° against each other. The shape of the individual modules is visible in figure 3.10a. The modules are shaped such that the overlap region has a circular shape of 44 cm diameter and a 4.5 cm hole in the center for the photon beam.

Due to the three layer setup it is possible to unambiguously distinguish two hits in the detector, as illustrated in figure 3.10b. In case of more than two hits in the detector, the combinatorial ambiguities need to be resolved with the help of other detectors.

The single fibers of the MOMO detector are attached to 16-channel photo multiplier tubes, read out with leading edge discriminators and commercial TDCs with about 80 ps RMS time resolution[6]. With this read out the detector achieves a time resolution of 1.5 ns and a position resolution of 2.5 mm. When

[6] CAEN V1190A-2eSST [CAEb]

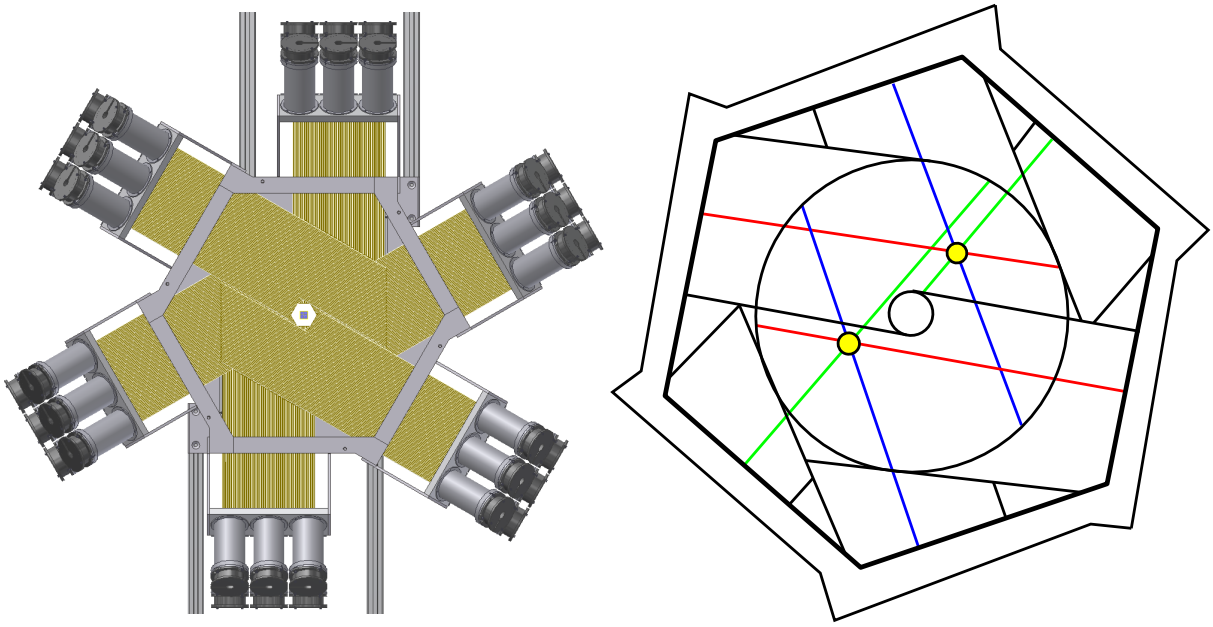

(a) (b)

Figure 3.10: (a) Schematic drawing of the MOMO detector. (b) Illustration of the reconstruction of the hit position of two charged particles which were coincident in time (yellow dots).

requiring a signal from only two of the three layers to detect a particle, the efficiency is 80 %, which reduces to 60 % if 3 layers are required [Jud11]. This loss is due to small gaps between the fibers. As the detector is only 1 m away from the spectrometer magnet, special 1 mm thick Permenorm cylinders were added to the detector to shield the photo tubes from the magnetic field. With this shielding the pulses produced by the PMT are sufficient, even at full magnetic field [Jah].

SciFi2

The second point for the track in front of the spectrometer magnet is provided by the SciFi2 detector. The SciFi2 detector, as MOMO, is a scintillating fiber detector. It was explicitly designed for the use at the BGO-OD experiment [Bös16] and is directly attached to the spectrometer magnet.

The fibers of the SciFi2 detector are arranged in two layers, one horizontal and one vertical layer. Each layer consists of 320 BC440 [Sai] fibers with a diameter of 3 mm. The fibers are overlapping each other to avoid inefficiencies due to particles crossing less material, and therefore depositing less energy and producing less light. The distance between two neighboring fibers is 2 mm, giving the spatial resolution of the detector. The fibers are packed together in modules of 16 fibers and connected to 16-channel PMTs [7]. To withstand the magnetic field the PMTs are shielded by iron tubes and mounted at an angle to the magnetic field lines of the spectrometer magnet [Bös16]. The achievable time resolution of the SciFi2 detector is 2 ns. It covers ±10° in horizontal and ±8° in vertical direction. In the middle a $4 \times 4\,\mathrm{cm}^2$ hole allows the photon beam to pass.

[7] Hamamatsu H6568

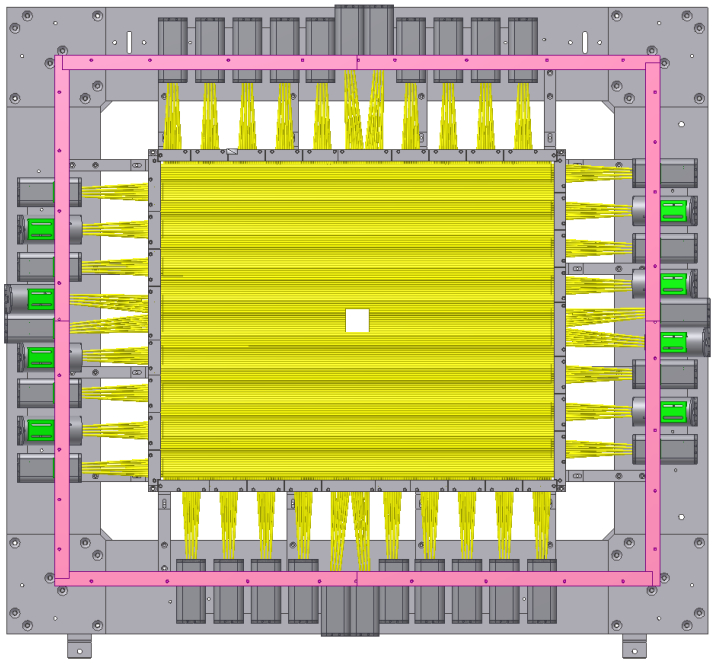

Figure 3.11: Schematic drawing of the SciFi2 detector.

Drifchambers

Eight driftchambers are installed behind the spectrometer magnet. Each driftchamber consists of a gas volume with anode wires surrounded by potential wires (cathode) forming hexagonal drift-cells, as shown in figure 3.12. The anode (sens wire) usually is on ground potential and the potential wires on a negative potential of about 3 kV. Charged particles crossing the gas volume ionize the gas and produce free electrons. These electrons are accelerated by the electric field. When they have gained enough energy they will ionize more gas atoms and produce an electron avalanche. When these electrons reach the anode wire they produce an electric pulse, which can be measured. Depending on the time the electrons needed to drift to the anode wire it is possible to calculate the distance, of the interaction point of the charged particle with the gas volume, to the anode wire. With this method a spatial resolution of better than 300 µm can be achieved [Sch10].

Eight driftchambers are installed. Two chambers with horizontal wires, two with vertical wires and each two chambers with wires tilted by ±9° to the vertical. The tilted chambers allow events with more then one particle in the forward spectrometer to be resolved. The exact dimensions of the chambers are listed in table 3.3.

Chamber	Wire direction	Width [mm]	Height [mm]	Sensitive area [mm^2]	Anode wires	Potential wires	Gas volume [L]
X	vertical	2867	1965	2456 × 1396	288	868	284.3
Y	horizontal	3053	1779	2483 × 1232	144	436	289.9
U	vert. +9°	3139	2335	2592 × 1765	304	916	398.2
V	vert. -9°	3139	2335	2592 × 1765	304	916	398.2

Table 3.3: Dimensions of the driftchambers [Sch10].

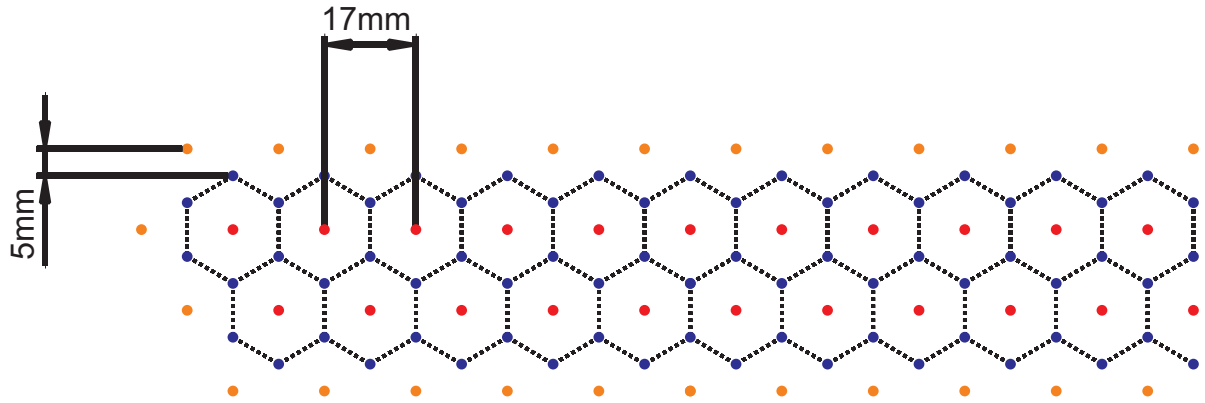

Figure 3.12: Drift-cell layout of one driftchamber from [Ham08]. Drift-cells (dashed blue lines) are arranged in two layers. Each drift-cell consists of the sens wire (red) and six potential wires (blue). To assure an equal field distribution in each cell, additional field forming wires (orange) surround the two layers of drift-cells.

TOF

To identify the particle type in the forward spectrometer, in addition to the momentum, the time of flight is needed. From the time of flight the β of the particle can be calculated and from β and momentum, mass and energy can be determined.

Wall	Source	Number of Bars	Bar Dimensions	Average Time Resolution
1	GRAAL	14	$300 \times 11.5 \times 3\,\mathrm{cm}^3$	~300 ps
2	GRAAL	14	$300 \times 11.5 \times 3\,\mathrm{cm}^3$	~300 ps
3	SAPHIR	8	$340 \times 21.5 \times 5\,\mathrm{cm}^3$	~500 ps

Table 3.4: Properties of the three horizontal TOF-walls.

To measure the time of flight, four TOF-walls are installed behind the driftchambers. The TOF-walls consists of long bars of plastic scintillator and are installed at a distance of about 5 m to the target. The four TOF-walls are divided in three walls with horizontal bars and one wall with vertical bars. Where the TOF-wall with vertical bars is currently not used in the experiment. The scintillator bars of the first two walls with horizontal bars were originally built for the former GRAAL experiment [Sch+98]. The bars of the later wall with horizontal bars and the wall with vertical bars were built for the former SAPHIR experiment [Sch+94]. SAPHIR TOF-bars provide a time resolution of ~500 ps and the GRAAL TOF-bars a time resolution of ~300 ps [Sch12; Mei13; Bau14]. The horizontal plane at the hight of the beam is dominated by electron-positron pairs, generated by electromagnetic interactions of the photon beam at the target and other detector components. The horizontal TOF-walls therefore have a gap in the central region.

The TOF-walls not only provide position information

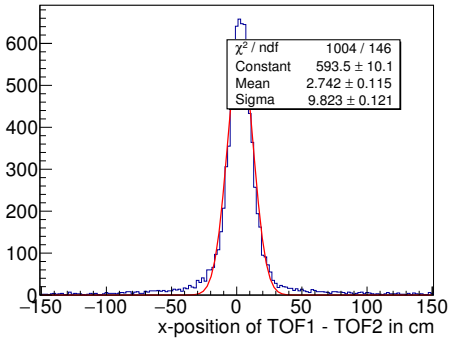

Figure 3.13: Difference in x-position measured by TOF-wall 1 and 2 for hits coincident in time. A Gaussian fitted to the distribution has a sigma of 9.8 cm, which is the convolution of the resolutions of both TOF-walls. The position resolution of one TOF-wall is then given by: $9.8\,\mathrm{cm}/\sqrt{2} \approx 6.9\,\mathrm{cm}$

from the hit bar, but also the position along the bars is given by the mean-time of the two signals of both ends of the bar. With this method a position resolution of 6.9 cm can be achieved, as shown in figure 3.13. The vertical position resolution is determined by the width and overlap of the bars of different TOF-walls. When taking all walls into account, a position resolution of about 10 cm can be achieved. With these values of the horizontal and vertical position resolution it is possible to correlate tracks from the driftchambers with hits in the TOF-walls.

3.2.5 Intermediate Detectors

The polar angle range between the acceptance of the central calorimeter and the forward spectrometer is covered by the SciRi and the Daisy detectors. In the laboratory frame this angular range of Θ^{lab} = 10° to 25° is small, but in the center of mass frame of hadronic reactions this range is large and very important for several reaction channels of interest.

SciRi

SciRi, short for scintillating ring detector, shown in figure 3.14, consists of three rings of 32, 2 cm thick scintillator ring segments. It is mounted inside the opening cone of the BGO-ball [Züg15; Sch15a]. Each ring of SciRi covers a Θ^{lab} range of 5° and the 32 pieces in Φ correspond to the 32 crystals of the BGO-ball in one crown. Each scintillator is attached to an avalanche photo diode (APD) and the signals are read out by jDisc modules. SciRi has a time resolution of up to 3 ns and a position resolution of 5° in Θ^{lab} and 11.25° in Φ direction [Sch15a].

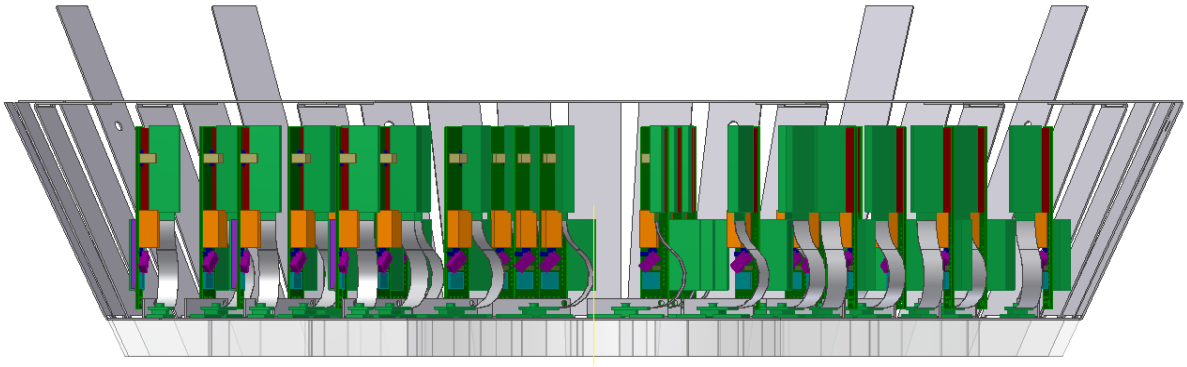

Figure 3.14: Schematic drawing of one SciRi half. The front face with the scintillator ring segments, which normally point towards the target, is pointing to the bottom in the picture. The scintillators (transparent) are wrapped in aluminum foil and glued to a 1 mm aluminum plate (gray). The APDs (green parts on top of the aluminum plate) are attached to scintillator through holes in the aluminum plate. With a short cable the APDs are connected to an electronics board which contains the preamplifier and controls the high voltage of each APD. To shield the detector from electromagnetic noise, it is surrounded by an aluminum cage.

Daisy

Daisy is a multi gap resistive plate chamber (MRPC), shown in figure 3.15. The detector covers a Θ^{lab} range of 8° to 25° and is divided in 16 petals in two layer with 8 petals each. Both layers are rotated by 20° against each other, similar to a daisy. It has a time resolution of ~30 ps and is therefore useable as

a time of flight detector, even at the short distance from the target of about 1 m. Each petal is divided in 15 concentric strips which are read out on both sides. The signal is processed by 32 channel multihit TDCs (CAEN V1290A [CAEa]) which have a time resolution of 25 ps. A position resolution of 1 cm should be achieved by this detector.

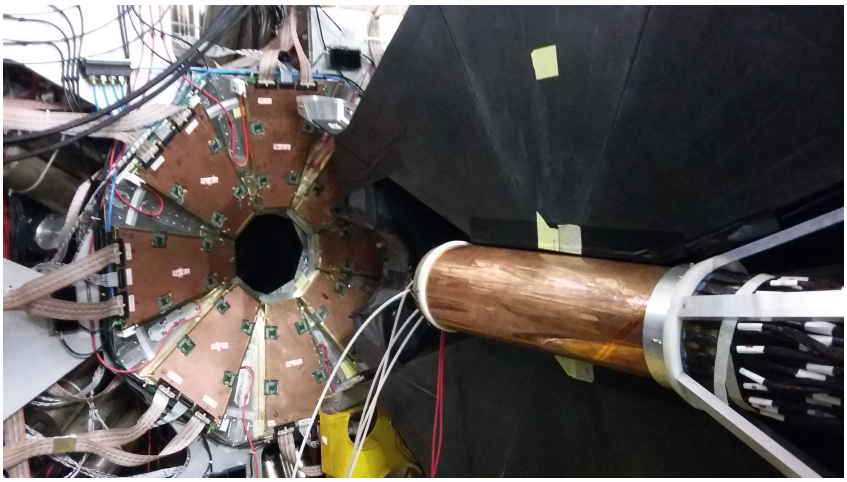

Figure 3.15: Picture of the daisy detector and the half opened BGO-ball with the MWPC inside. The black shape on the right half of the picture is the carbon-fiber holding structure of the BGO crystals. The copper cylinder inside is the MWPC. In the left half of the picture, behind the BGO-ball the copper colored petals of the daisy detector is shown. It is mounted on two sides of a honeycomb plate with holes for the PMTs of the MOMO detector and a hole in the center for particles going in the direction of the forward spectrometer.

3.3 Data Acquisition

The DAQ of the BGO-OD experiment is described in detail in [Ham16]. In this section only the trigger part is described.

The goal of a triggered DAQ is to record only data if an interesting event happened. All times measured in the detector components of the experiment are relative to this trigger. It is therefore important to understand under which conditions a trigger signal is generated. Each detector (except MOMO and the driftchambers) provides a local trigger signal if a certain condition is fulfilled. For most detectors the condition for a local trigger signal is just a signal in one of its channels above a given threshold, which is called a hit. The tagging detector, the BGO-ball and the TOF-walls have more complicated conditions to generate local trigger signals.

As post-bremsstrahlung electrons in the tagging detector always hit at least two adjacent channels, the local trigger signal of the tagging detector is only produced if two adjacent channels were hit.

The BGO-ball can produce two different local trigger signals. The mixer modules of the BGO-ball provide an energy sum signal, which is the analog sum of the analog PMT signals. The trigger condition is the requirement of a total energy sum exceeding either 100 MeV or 160 MeV.

The TOF-walls are read out on both sides of each bar. The local TOF trigger signal therefore requires two corresponding channels have to have a signal.

The DAQ uses all the local triggers to decide whether the current event should be recorded, by sending a global trigger signal to all detectors. If a given set of conditions are passed, this starts the read-out of the data acquired by the detectors. In the normal data-taking mode the condition for this decision is

given by a logic OR of the following conditions:

- Hit in tagging detector
  & BGO energy sum > ~160 MeV
- Hit in tagging detector
  & BGO energy sum > ~100 MeV
  & hit in SciRi
- Hit in tagging detector
  & hit in SciRi
  & hit in SciFi2
  & hit in at least one TOF-wall
- Hit in tagging detector
  & BGO energy sum > ~100 MeV
  & hit in SciFi2
  & hit in at least one TOF-wall
- Scaler trigger (20 Hz)
- Spill trigger (At beginning and end of every spill)

The last two triggers are special: The scaler trigger comes at a fixed rate of 20 Hz and causes a latch and readout of the scalers, which count the number of events since the last reset, to prevent them overflowing. The spill trigger intends to synchronize the scaler readout to spill structure of the electron beam. This trigger assures that in one scaler readout, the data taken in the extraction phase (see section 3.1) and data taken during the injection and acceleration phase is not mixed together.

As the tagging detector is always required in an event, to provide the energy of the initial state of the reaction, and has, expect for Daisy (see section 3.2.5), the best time resolution of the detectors in the experiment, it determines the time of an event. Therefore the tagging detector is always included in all trigger conditions used for data-taking.

The trigger logic of the DAQ is implemented in an FPGA as clocked logic, with a 200 MHz clock [Bie11]. All times recoded by the DAQ are relative to the time of the global trigger.

3.4 Data Analysis

The aim of the data analysis is to identify and reconstruct the kinematics of hadronic reactions from correlated signals from the BGO-OD detector components.

The first step in the data analysis is to calibrate the signals in time and check for time coincidences. Where required, the electronic signals from the detectors are calibrated to give the true energy deposition in MeV. Using the known geometry of the experiment, the full four-momentum and type of particles can then be reconstructed as described in sections 3.4.5 and 3.4.6. This information is then combined to tracks which can be used in the further physics analysis.

3.4.1 Time Calibration

The time calibration is performed in several steps. In the first step the 5 ns jitter introduced by the 200 MHz clock of the global trigger is compensated for. This is possible because all local triggers are

recoded on a TDC and from this information it is possible to determine the event-wise offset between event and trigger. In a second step the prompt events in each detector are assigned the time $t = 0\,\text{ns}$. Where prompt event means the events that are correlated to the event which caused the trigger signal.

3.4.2 BGO-ball Energy Calibration

For an initial energy calibration of the BGO-ball, to convert the raw analog to digital converter (ADC) channels to MeV, ^{22}Na sources are used. The attenuators of the mixers, in the readout chain of the BGO-ball, are set to 0 dB attenuation, instead of 12 dB that are used for normal data taking. An energy spectrum of the ^{22}Na sources is then recorded.

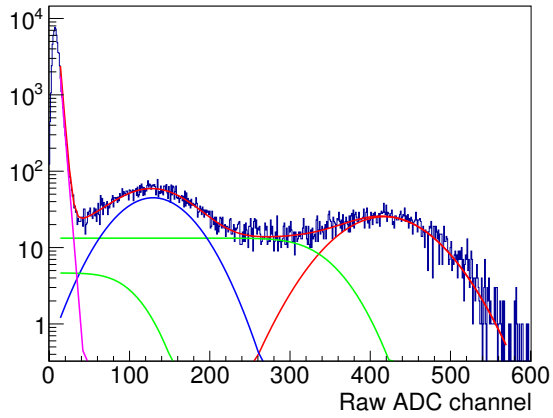

Figure 3.16: ^{22}Na spectrum from a calibration of one channel of the BGO-ball. Fitted to the spectrum are two gausian for the two peaks at 0.511 MeV and 1.27 MeV (blue and red), as well as the two corresponding Compton edges (green).

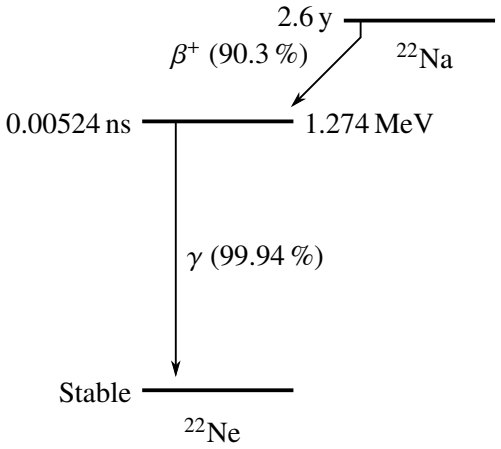

Figure 3.17: Decay chain of ^{22}Na. ^{22}Na decays to an excited state of ^{22}Ne via a β^+ decay. This state nearly immediately decays to the ground state of ^{22}Ne via the emission of a 1.27 MeV γ. The positron from the β^+ decay annihilates with an electron under the emission of two 0.511 MeV γ.

From the two peaks at 0.511 MeV and 1.27 MeV in the ^{22}Na spectra (see figures 3.16 and 3.17) the measured SADC values are calibrated for each crystal individually by accounting for the 12 dB attenuation. This energy calibration is already good at the 5 % level. Further corrections are applied during the clustering in section 3.4.3.

3.4.3 BGO-ball Clustering

The energy deposition in the BGO-ball is dependent upon particle type. High energy photons predominantly lose their energy in matter by electron-positron pair production and high energy electrons by bremsstrahlung. The produced photon or electron can again do pair production or bremsstrahlung as long as they have enough energy. Therefore photons and electrons hitting the BGO crystals produce electromagnetic showers, which span over several crystals of the calorimeter. Also other particles can penetrate several crystals and therefore produce a signal in more than one channel. Therefore the hits in the individual crystals of the BGO-ball are combined to clusters, with the idea that one cluster corresponds to one particle. The distribution of cluster sizes for photons and protons are shown in figure 3.18 and described below.

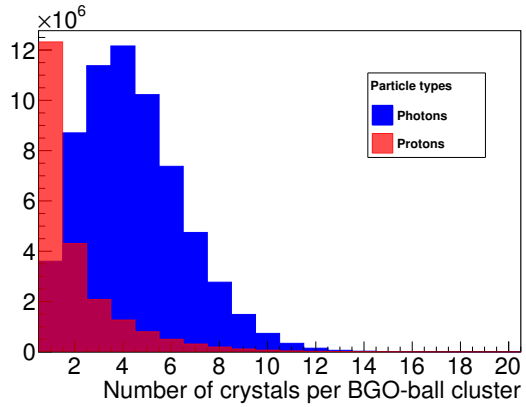

Figure 3.18: Red: protons (mostly one crystal), blue: photons (mostly 3 or more crystals). The data is taken from an analysis of $\gamma p \rightarrow p\pi^0 \rightarrow p\gamma\gamma$ performed by Oliver Freyermuth.

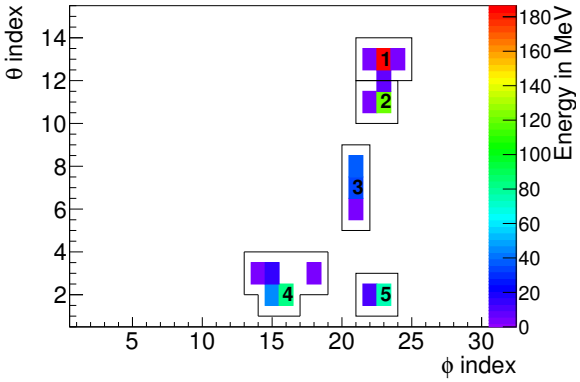

Figure 3.19: In the first step the local maxima are searched (numbered with 1-5). All remaining energy deposits are assigned to the closest local maximum (indicated by black boxes). Due to this cluster 1 and 2 are separated in two clusters, the energy deposit in between is assigned in equal parts to both clusters. Figure taken from [Sch15a].

To identify the clusters a local maxima clustering algorithm is used [Sch15a]. In this algorithm local maxima of the energy deposition in the BGO-ball are searched. A local maximum is found by comparing the amount of deposited energy in one crystal to the energy deposited in all surrounding crystals. If the crystal contains more energy than every surrounding crystal a local maximum is found, where local maxima with an energy of less than 5 MeV are ignored. All remaining energy deposits are added to the closest local maximum to form the clusters. This method is illustrated in figure 3.19.

To assign a time to the cluster the energy weighted mean, of the times of all crystals contributing to the cluster, is used.

$$t_{cluster} = \frac{\sum_i t_i E_i^2}{\sum_i E_i^2} \tag{3.4}$$

The position of the cluster is determined by the mean of the individual central positions of the crystals contributing to this cluster, weighted by the square root of the deposited energy.

$$\overrightarrow{r_{cluster}} = \frac{\sum_i \vec{r_i} \sqrt{E_i}}{\sum_i \sqrt{E_i}} \tag{3.5}$$

With this method for photon clusters a position resolution of better than the detector granularity can be achieved, as for large clusters the cluster position can be determined better than the size of one crystal. The energy of the cluster is the sum of energy deposited in each crystal contributing to the cluster.

$$E_{cluster} = \sum_i E_i \tag{3.6}$$

In addition two corrections are applied to the cluster energy. When the cluster spreads over more than one crystal, some part of the shower deposits energy in the dead material between two crystals. This correction is small of about 4 % and only applied to photons, as other particles tend not to spread over several crystals. Another effect with an influence on the measured cluster energy, is the temperature

dependence of the crystal light output and PMT gain [Ghi+98a]. Even when performing BGO-ball energy calibrations (see section 3.4.2) two to three times a day, the temperature dependence is measurable. Therefore a run-wise correction factor is applied to the determined cluster energy. This run-wise correction factor is obtained by analyzing the reaction $\gamma p \rightarrow p\pi^0 \rightarrow p\gamma\gamma$, and fitting the π^0 mass peak in the $\gamma\gamma$ invariant mass distribution and calculating the necessary scaling factor to scale the π^0 mass peak to its official mass taken from the Particle Physics Booklet [Oli+14]. This correction is in between $-6\,\%$ to $5\,\%$.

3.4.4 Barrel Particle Identification

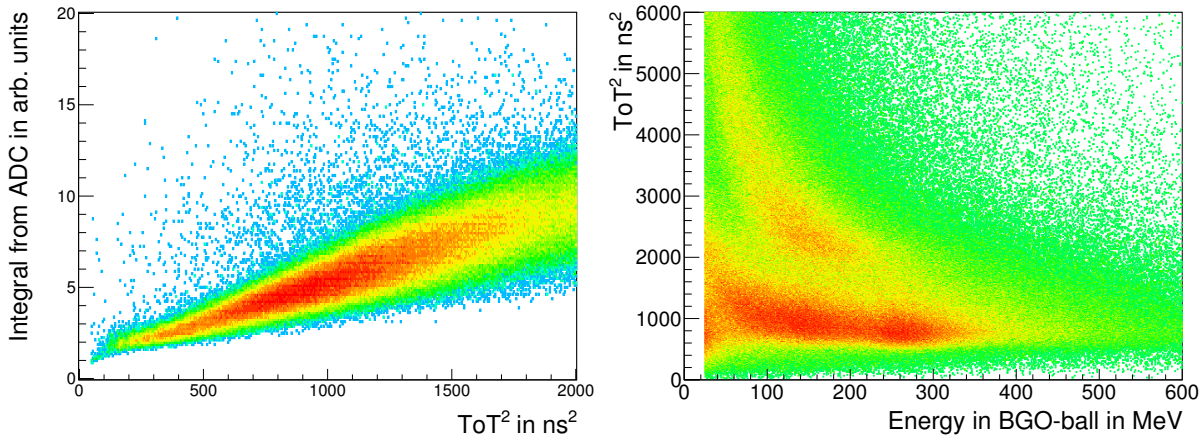

(a) (b)

Figure 3.20: Particle identification in the scintillator barrel [Fre15]. (a) Shows the linear correspondents between ToT^2 and the pulse integral measured by an ADC. (b) Shows ToT^2 versus the deposited energy in the BGO-ball. Where one can distinguish protons from pions by their difference in ToT^2 in dependence on the energy deposited in the BGO-ball.

The deposited energy per unit length of a particle depends on β. As β depends on mass and momentum of a particle, it is possible to identify particles by the dE/dx-method. The ToT, measured of the signals of the scintillator barrel, is correlated to the signal integral, as one can see in figure 3.20a. As the integral is correlated to the deposited energy, it is possible to get an energy information from the detector [Fre15]. When plotting the energy deposited in the BGO-Ball against the square of the time over threshold, protons and pions can be separated, as shown in figure 3.20b, where bands for protons, pions and electrons are visible.

3.4.5 Central Tracking

To combine the information of the detectors of the central calorimeter central-tracks are built. These tracks combine the information of the BGO-ball and the scintillator barrel. The information from the MWPCs is not included, as they were not in operation at the time of writing this thesis.

By cutting on the time and polar angle difference between clusters in the BGO-ball and hits in the scintillator barrel both can be combined (shown in figure 3.21). When an entry lies within the cuts shown in figure 3.21b for time t and the cuts shown in figure 3.21a for polar angle Φ a charged central-track is built. If a BGO-ball cluster can not be combined with a scintillator barrel hit a neutral central-track is

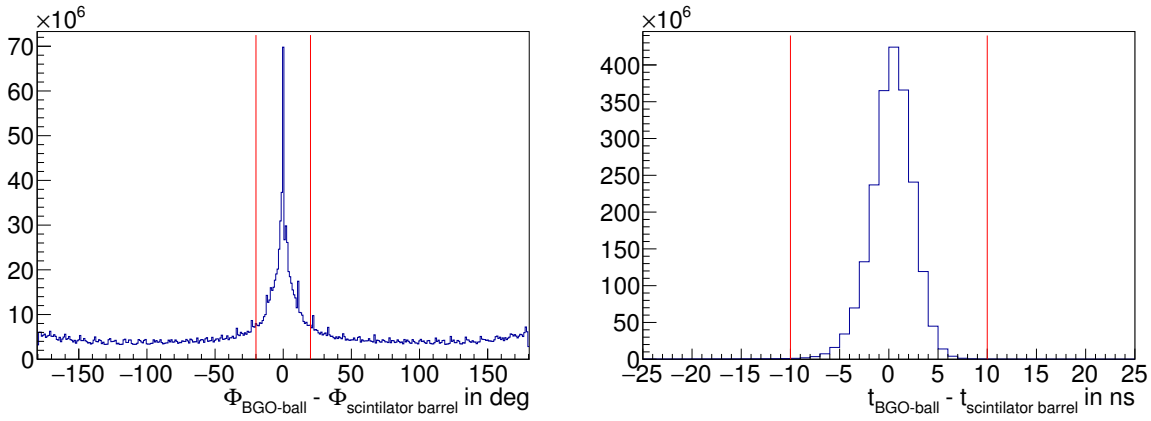

(a) (b)

Figure 3.21: Cuts used to assign hits in the scintillator barrel to clusters in the BGO-ball. (a) Differences in the Φ angle determined from a hit in the scintillator barrel to the Φ angle determined from a cluster in the BGO-ball. A clear peak of correlated events on top of uncorrelated events can be seen. The cut applied to identify correlated events is indicated by red lines. (b) Difference in the time of BGO-ball cluster and scintillator barrel hits. A clear peak for coincident times can be seen. The cut used to select coincident events is indicated by the red lines.

build. In both cases energy, polar-angle, azimuthal-angle and time of the central-track are given by the values of the BGO-ball cluster.

If one hit bar of the scintillator barrel covers several clusters in the BGO-ball, all central-tracks produced from these clusters are marked as charged.

3.4.6 Forward Tracking

From the curvature of a charged particle in the forward spectrometer, the full four-vector of the particle can be reconstructed.

The track finding is performed in four steps: finding a front-track in front of the spectrometer magnet from hits in MOMO and SciFi2, finding a rear-track behind the spectrometer magnet from hits in the driftchambers, combining front and rear-tracks to form combined-tracks and finally adding hits in the TOF-walls [Jud11].

For the front-tracks one dimensional clusters are built from hits in adjacent fibers in each layer of MOMO and SciFi2. These one-dimensional clusters are then combined to three dimensional clusters in each detector. In case of multiple clusters all possible combinations are built. Then the cluster in MOMO and SciFi2 are combined to form front-tracks. Which is a 3D vector connecting both clusters in a straight line. By requiring that the track originates from the target, by cutting on the distance of the front-track to the z-axis at $z = 0\,\text{cm}$ (shown in figure 3.22) to be less than 3 cm, many false combinations of MOMO and SciFi2 cluster are removed.

To find rear-tracks behind the spectrometer magnet again for each of the eight driftchambers one-dimensional clusters from hits in adjacent driftcells are built. These clusters are then combined to a rear-track by assuming straight lines between the chambers.

To combine front- and rear-tracks to combined-tracks all combinations of front- and rear-tracks are built, if the following constrains are fulfilled:

- Limits in curvature

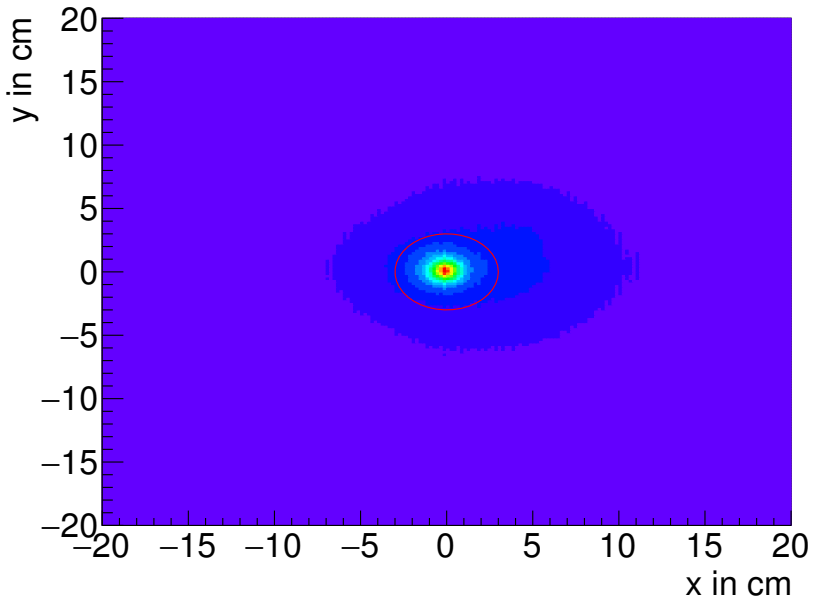

Figure 3.22: Position in the x-y-plane at the target center ($z = 0\,\text{cm}$). A peak at (x,y)=(0,0) can be seen. The applied cut to decide if a track originates from the target is indicated by the red circle.

Due to the constrained geometrical volume of the spectrometer magnet, only a limited curvature of the particle track in the x-z-plane is possible. To reflect this, straight front- and rear-tracks are assumed and a cut is applied on the intersection point of front- and rear-track. In figure 3.23c the y and z coordinate of the interception point is plotted. In figure 3.9 the front- and rear-track were indicated by the dashed blue and red line. For valid tracks this interception point should always be within the open dipole magnet. This is required by the cut on the magnet position shown in figure 3.23c by the red box.

- Straight tracks in y-z-plane

  As the magnetic field of the spectrometer magnet is along the y-direction, the charged particles are only bend in the x-z-plane. In the y-z-plane they are, in first order, not influenced by the magnetic field and therefore should form straight tracks in the y-z-plane. Therefore an angle difference of $0° < \alpha < 1.5°$ and an offset in y-direction of $\pm 5\,\text{cm}$ is allowed, as indicated by the red box in figure 3.23d.

The assignment of a momentum to the combined-tracks is again performed in two steps. In the first step a first approximation of the momentum is made by extrapolating the front- and rear-tracks to the center of the spectrometer magnet and calculating the radius of curvature. From this radius of curvature and the assumption of a homogenous box like field, the momentum is calculated according to the Lorentz force. This value, which is accurate within 10 %, is used as a start value for the second step. In the second step a particle is simulated and tracked through the magnetic field, where this time a measured field map [Fre12] of the magnetic field is used and energy loss of the particle is accounted for. The start momentum of the particle is varied until the simulated trajectory reflects the real measured trajectory.

By extrapolating the combined-tracks to the TOF-walls and looking for coincidences between combined tracks and hits in the TOF-walls can be combined. From the flight-time measured by the TOF-

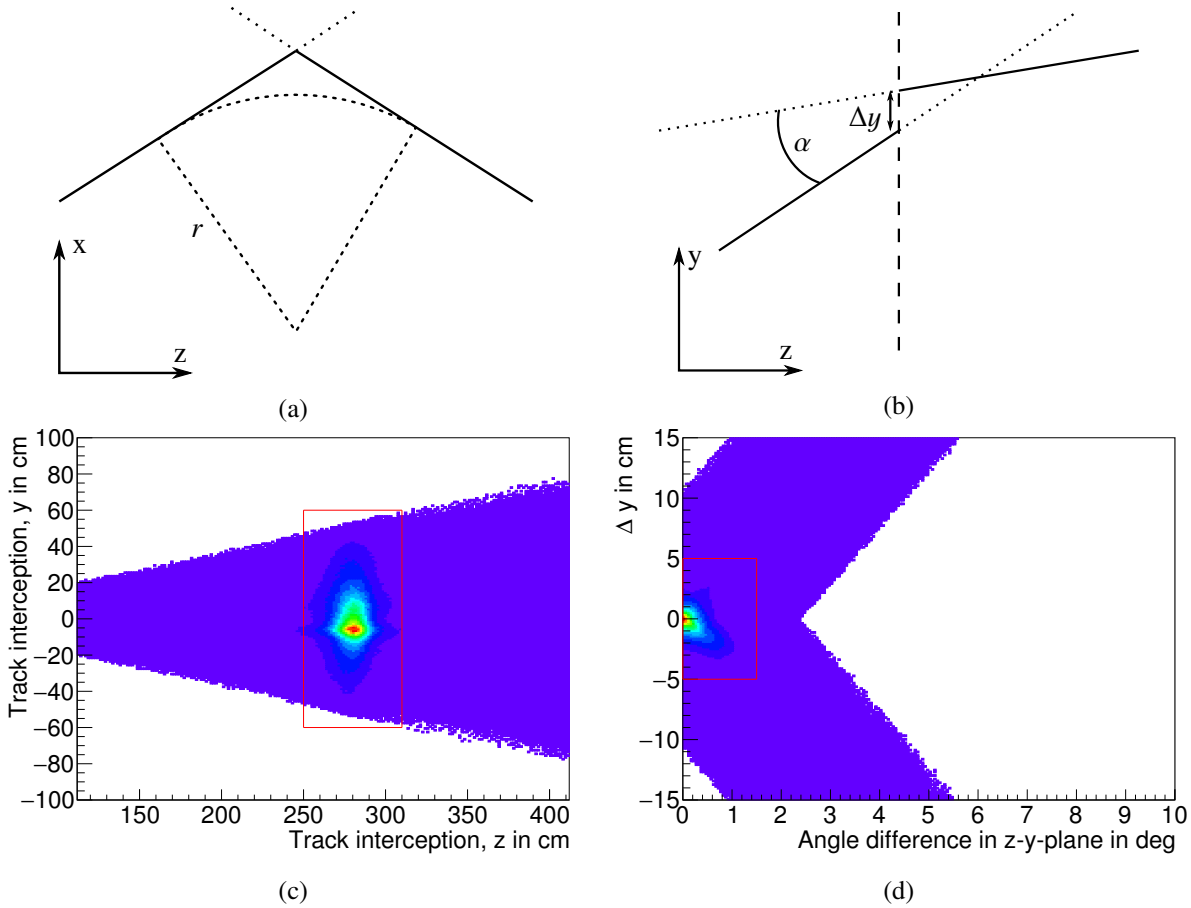

Figure 3.23: Track finding from front and rear track parts in the forward spectrometer. At first limits to the radius of curvature are applied. Therefore the radius of curvature is estimated as indicated in (a), by extrapolating front and rear tracks straight through the dipole magnet. Only if the intercept of front and rear track is within the geometrical volume of the dipole magnet, the track is accepted, as indicated in (c), where the red box indicates the cut on the y and z track intercept coordinate. Then the angle difference in the y-z plane is determined, according to (c), and the final track combinations are selected with the cut indicated by the red box in (d).

walls and the trajectory of the combined-track, a β can be assigned to the track to form the final forward-track. These tracks can then be used in the further analysis.

CHAPTER 4

Circular Polarized Photon Beams

For modern photoproduction experiments polarization degrees of freedom are essential. The polarization of the photon beam is defined by the orientation of the electric field vector of the electromagnetic wave. In the case of linear polarization, the field vector oscillates in one plane. In the case of circular polarization the field vector rotates around the direction of motion. In chapter 1 the different polarization observables were introduced including circular beam polarization. Different combinations of polarization degrees are needed to measure different polarization observables. This chapter describes the production of circularly polarized photon beams, and the determination of the degree of circular polarization at the BGO-OD experiment with an in-situ Møller polarimeter.

4.1 Production of Circularly Polarized Photon Beams

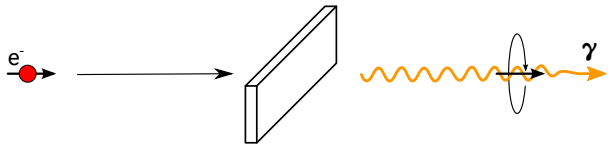

Figure 4.1: Illustration of the production of circularly polarized photon beams. The electron hits the radiator and produces a photon via bremsstrahlung. The post-bremsstrahlung electron is not shown in this figure. The black bold arrows along the direction of motion indicate the helicity of the particles.

Circular polarized photon beams can be produced by bremsstrahlung of longitudinally polarized electron beams. The helicity $h = \frac{\vec{s}\cdot\vec{p}}{|\vec{s}\cdot\vec{p}|}$ is defined as the projection of the particle spin, $\vec{s}$, on the direction of its momentum, $\frac{\vec{p}}{|\vec{p}|}$. In the case of relativistic particles, which is the case for the electrons at the BGO-OD experiment, the helicity is practically conserved, as no Lorentz transformation can change the projection of the particle spin on the direction of motion for particles with speed of light. To get an impression of the general behavior of this process, one can assume a simple picture. A longitudinal polarized electron ($h_{e^-} = \pm 1$) undergoes bremsstrahlung and transfers all of its momentum to the photon. As all of the momentum of the electron is transferred to the photon, the electron momentum is now equal to $\overrightarrow{p_{e^-}} = \vec{0}$ and therefore the helicity of the electron is $h_{e^-} = 0$. Due to the conservation of the helicity in this reaction, the helicity has to be taken over by the photon. The two possible helicity states of the photon ($h_\gamma = \pm 1$) are called left handed, and right handed and correspond to the two possible circular polarization states of the photon. Therefore in the case of full momentum transfer from the electron to the photon, the full longitudinal polarization of the electron beam is transferred to circular polarization of the photon beam. In the other extreme, where no momentum is transferred to the photon, no photon is produced and therefore no helicity can be transferred from the electron to the photon, and

therefore no polarization is transferred.

This can be described completely in QED, where the polarization transfer as function of the momentum transfer is given by equation 4.1 [OM59] and plotted in figure 4.2.

$$\frac{P_\gamma}{P_e} = \frac{\left(3 + 1\left(1 - \frac{E_\gamma}{E_e}\right)\right)\frac{E_\gamma}{E_e}}{3 + 3\left(1 - \frac{E_\gamma}{E_e}\right)^2 - 2\left(1 - \frac{E_\gamma}{E_e}\right)} \tag{4.1}$$

Longitudinally polarized electrons are provided by the ELSA accelerator and the momentum transfer from the electron to the bremsstrahlung photon is measured by the tagging detector (see chapter 3.2.1). The degree of longitudinal polarization of the electron beam needs to be measured in order to determine the degree of circular polarization of the photon beam using equation 4.1.

Measuring the electron polarization can be done with different methods. Commonly used polarimeters use the polarization depending upon the Compton, Mott or Møller scattering cross sections.

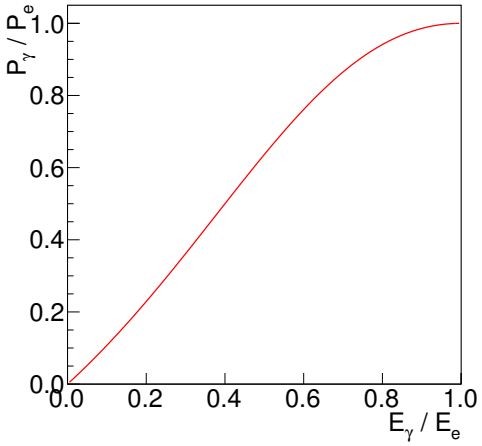

Figure 4.2: Polarization transfer from the electron to the photon beam in dependence on the energy transfer.

4.2 Mott Scattering

Mott scattering is a common tool for electron beam polarization measurements at energies low enough for spin-orbit couplings to be significant. By scattering electrons off of thin gold foils, one measures a left-right asymmetry for parallel and anti-parallel spin orbit couplings. The asymmetry, A_{Mott} is given by

$$A_{Mott} = S\,P \tag{4.2}$$

where P is the degree of polarization and S the Sherman function, which, for instance, is $S = -0.39 \pm 1\%$ for an electron energy of 100 keV, when scattering off of a gold foil at a scattering angle of 120° [Gow01]. This gives a large asymmetry, resulting in a statistically accurate determination of the polarization. Unfortunately the Mott cross section is proportional to $\frac{1}{E^2}$ and the asymmetry to $\frac{1}{E}$, making it unsuited for the high electron energies of up to 3 GeV that are needed at the BGO-OD experiment. However a Mott polarimeter is set up at the ELSA accelerator to measure the polarization of the electron in the transfer channel between the electron gun and the LINAC 2 [Gow01], where the electrons have an energy of 50 keV.

4.3 Compton Scattering

At higher energies Compton scattering can be used to determine the degree of electron beam polarization. This is typically done by scattering circularly polarized photons, produced by a laser and a $\frac{\lambda}{4}$-plate, off the electron beam. By measuring the scattering angle of the back-scattered photons, the degree of polarization can be determined. It is planned to build such a polarimeter at the ELSA accelerator [Dol98; Koo]. With a laser intensity of 10 W, an electron beam intensity of 100 mA and a measuring

time of 100 s, a relative statistical error of 3 % should be achieved. The disadvantage of a Compton polarimeter are the high electron intensities needed for the measurement. Therefore it is normally limited to measurements of the electron beam polarization within the accelerator, as the extracted currents at ELSA are 8 orders of magnitude lower, than the assumed 100 mA.

Extracting the beam from the accelerator influences the degree of polarization, as the spin is rotated by several magnets, as described in chapter 3.1.1. To measure the degree of polarization of the extracted electron beam, a different method is needed.

Nevertheless if the change of polarization due to the extraction is known, it is enough to monitor the degree of polarization in the stretcher ring with a Compton polarimeter. Then it might also be possible to do experiments with linearly and circularly polarized photons simultaneously by using a crystal radiator with a polarized electron beam, as it is proposed by A. B. Apyan [Apy+98]. This is currently investigated at the Crystal-Ball experiment at MAMI in Mainz [Afz15].

4.4 Møller Scattering

To determine the degree of polarization directly at the BGO-OD experiment a polarimeter, which determines polarization via Møller scattering, is used, which is described in the following sections.

Møller scattering was first described by Christian Møller in his work "Zur Theorie des Durchgangs schneller Elektronen durch Materie"[1] [Møl32]. Beside the scattering of electrons off atoms, the scattering off free electrons is described. The cross section calculated in this section of his work was later named Møller cross section, and the scattering of electrons off free electrons was named Møller scattering.

The Møller cross section depends on the relative momenta and spin orientations. According to the Pauli principle, two fermions cannot share the same quantum numbers. If both electrons involved in the Møller scattering process have the same spin orientation, they should not have the same spatial wavefunction and therefore should not be able to scatter off each other. The cross section of Møller scattering is suppressed if both electrons have the same spin orientation.

By knowing the polarization of one of the involved electrons and measuring the asymmetry between the parallel and anti-parallel spin orientation it is possible to calculate the degree of polarization of the second electron. As the degree of polarization of the target electrons can be measured (see section 4.5.3), the polarization degree of the beam electrons can be determined.

4.4.1 Kinematics

As Møller scattering is the elastic scattering of an incoming electron on an electron at rest [2], the following energy and momentum conservation needs to be fulfilled:

$$E^0 + m_e c^2 = E'_1 + E'_2, \tag{4.3}$$

$$\overrightarrow{p^0} = \overrightarrow{p'_1} + \overrightarrow{p'_2}. \tag{4.4}$$

Where the variables of the two electrons are distinguished by subscript $_1$ and $_2$. The variables marked with a superscript ^{0} belong the the electron approaching before the scattering and the variables after the scattering with a superscript $'$.

[1] On the theory of the passing of fast electrons through matter
[2] When not considering the Levchuk effect (see section 4.6.1)

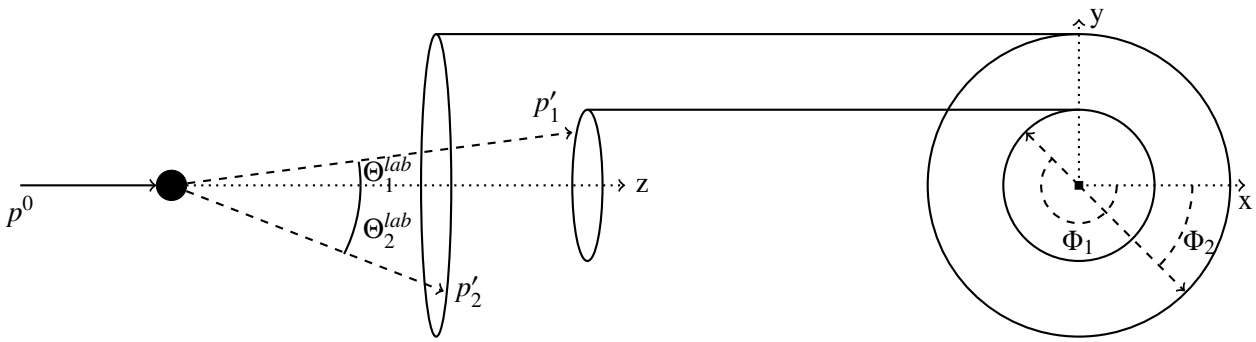

Figure 4.3: Kinematics of the Møller scattering. The left part shows a projection on the scattering on the y-z-plane and the right part shows a projection on the x-y-plane.

If assuming that the incoming particle was moving along the z-axis, equation 4.3 and 4.4 result in a fixed relation between scattering angle Θ_i and the energies E'_i, shown in equation 4.5.

$$E'_i = (E^0 + m_e)\cos\left(\frac{\Theta_i^{c.m.}}{2}\right)^2 + m_e,\ i \in \{1,2\} \tag{4.5}$$

Where $\Theta_i^{c.m.}$ is the center of mass angle between the z-axis and the corresponding particle momentum p'_i. The scattering angle Θ_i in the laboratory system, as shown in figure 4.3, is transformed to the scattering angle $\Theta_i^{c.m.}$ in the center of mass system by the following formula:

$$\tan\left(\frac{\Theta_i^{lab}}{2}\right) = \sqrt{\frac{E^0 + m_e}{2m_e}}\tan\left(\Theta_i^{c.m.}\right). \tag{4.6}$$

Therefore all particles scattered under a certain angle have the same energy, their momentum differs only in the Φ angle and the trajectory of scattered electrons, with the same energy, project out a cone shape.

The transverse momentum of the incoming electron is zero, so the total transverse momentum of both scattered electrons has to be equal to zero too. This is only achieved with a Φ angle difference between both scattered particles of 180°. Therefore, when projecting the momenta on to the x-y plane, the scattered electrons are going back to back.

In the case of symmetric Møller scattering, where both electrons have the same absolute momentum and therefore are scattered under the same $\Theta = \Theta_1 = \Theta_2$ angle, both electrons are scattered on the same cone on opposite sites.

4.4.2 Cross-Section

The original Møller cross section was determined without considering polarization degrees of freedom. The Møller cross section considering the polarization of the target and beam electron is given by [OM59, eq. 6.43]. To simplify the formulas the cross section below is factorized into different components as it was also done by [Wag+90] and [Kam10]:

$$\frac{d\sigma}{d\Omega} = \frac{d\sigma_0}{d\Omega}\left[1 + \sum_{j,k=x,y,z} a_{jk} P_j^{beam} P_k^{target}\right]. \tag{4.7}$$

a_{jk} is the asymmetry coefficient, also called analyzing power, for the different combinations of the polarization components, P_j^{beam} is the polarization of the electron beam along the specified axis and P_k^{target} is the polarization of the target electron along the specified axis. $\frac{d\sigma_0}{d\Omega}$ is the original Møller cross section, given by:

$$\frac{d\sigma_0}{d\Omega} = \frac{\alpha^2}{4E^2}\frac{1}{p^4 \sin^4 \Theta^{c.m.}} \cdot a_0. \tag{4.8}$$

Where α is the fine structure constant, E the incoming electron energy, $\Theta^{c.m.}$ the center of mass scattering angle, p the incoming electron momentum and a_0 is given by:

$$a_0 = \left[(2\gamma^2 - 1)^2(4 - 3\sin^2\Theta^{c.m.}) + (\gamma^2 - 1)^2(4 + \sin^2\Theta^{c.m.})\sin^2\Theta^{c.m.}\right]. \tag{4.9}$$

To simplify the calculations, a coordinate system is chosen, which is defined by the momentum vectors of the incoming electron ($\overrightarrow{p^0}$) and one of the scattered electrons ($\overrightarrow{p'}$):

$$\hat{z} = \overrightarrow{p^0}, \tag{4.10}$$

$$\hat{y} = \frac{\overrightarrow{p^0} \times \overrightarrow{p'}}{|\overrightarrow{p^0} \times \overrightarrow{p'}|}, \tag{4.11}$$

$$\hat{x} = \hat{y} \times \hat{z}. \tag{4.12}$$

In this coordinate system, the off-diagonal elements of a_{jk}, except a_{xz} and a_{zx}, are zero due to parity conservation. They only contain components orthogonal to the scattering plane. The remaining non-zero elements are given in the formulas 4.13-4.16:

$$a_{xx} = \frac{\sin^2\Theta^{c.m.}}{a_0}\left[(2\gamma^2 - 1) + (\gamma^4 - 1)\sin^2\Theta^{c.m.}\right], \tag{4.13}$$

$$a_{yy} = \frac{\sin^2\Theta^{c.m.}}{a_0}\left[(4\gamma^2 - 3) - (\gamma^2 - 1)^2\sin^2\Theta^{c.m.}\right], \tag{4.14}$$

$$a_{zz} = -\frac{\sin^2\Theta^{c.m.}}{a_0}\left[(2\gamma^2 - 1)^2(4\gamma^2 - 3) - (\gamma^4 - 1)\sin^2\Theta^{c.m.}\right], \tag{4.15}$$

$$a_{xz} = a_{zx} = -\frac{\sin^2\Theta^{c.m.}}{a_0}\left[\gamma(\gamma^2 - 1)\sin 2\Theta^{c.m.}\right]. \tag{4.16}$$

γ is the Lorentz gamma, given by $\gamma = \frac{E}{m}$. As one can see in figure 4.4, where the different a_{jk} are plotted, the largest value of around $a_{zz}(90°) \simeq -7/9$ is achieved in case of symmetric Møller scattering with the spin of the target and the spin of the beam electron aligned to the z-axis. Symmetric means both outgoing electrons are scattered under the same $\Theta^{c.m.}$ angle and have the same absolute momentum. This strong asymmetry of almost 1 between parallel and anti-parallel spin orientations can be understood due to the Pauli exclusion principle, as explained before. By measuring the asymmetry between parallel and anti-parallel spin orientations, it is therefore possible to determine the degree of polarization of longitudinally polarized beam:

$$A_{zz} = \frac{N^{\uparrow\downarrow} - N^{\uparrow\uparrow}}{N^{\uparrow\downarrow} + N^{\uparrow\uparrow}} = a_{zz}P_z^{beam}P_z^{target} \tag{4.17}$$

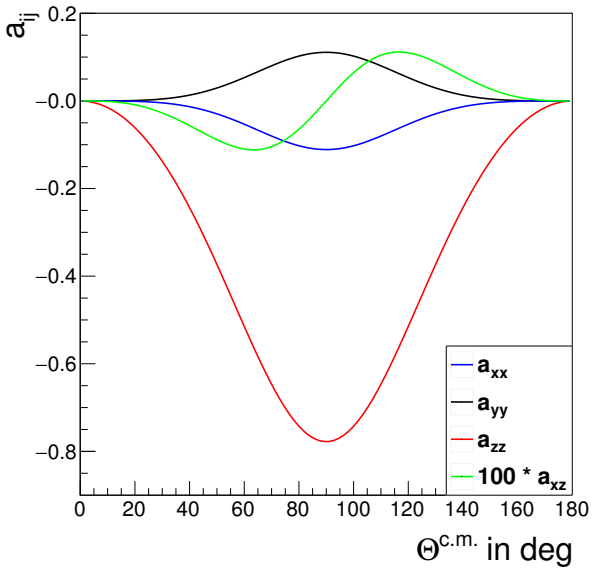

Figure 4.4: Analyzing power coefficients of polarized Møller scattering.

4.5 Møller Polarimeter

To utilize the Møller cross section for polarization measurements at the BGO-OD experiment, a momentum selecting Møller polarimeter was built. It detects symmetric Møller electron pairs in coincidence and uses an in plane magnetized ferromagnetic foil as a Møller and bremsstrahlung target simultaneously. By using a momentum selecting polarimeter, one is negligibly affected by the Levchuk effect (see section 4.6.1), and detecting symmetric pairs gives the highest analyzing power as shown in section 4.4.2. By using the same foil as Møller and bremsstrahlung target, one can measure the electron beam polarization in-situ.

4.5.1 Constraints

At the BGO-OD experiment two major space constraints exist for the Møller polarimeter. To separate the detectable Møller pairs as much as possible from the post-bremsstrahlung electrons, the detectors should be positioned as far as possible away from the radiator. The maximum distance of the Møller detectors to the radiator is limited by the electron beam-dump. There is sufficient space between the electron beam-dump and the tagging detector for the Møller detectors, however unfortunately the aluminum frame of the tagging detector has the same size as the diameter of the cone of the Møller electrons at this distance. With a depth of about 15 cm the frame would absorb most of the electron energy and scatter them away from the Møller detectors, so that they are not detected. Therefore the detectors have to be placed in front of the tagging detector.

The second constraint is the distance of the pole shoes of the tagging magnet. With a gap size of 7 cm and a distance from the downstream edge of the magnet to the radiator of 1.75 m, the cone of symmetric Møller electrons do not fit through, as shown in figures 4.5 and 4.6. To circumvent this constraint, the detector setup will be build such, that the symmetric pairs are not detected in the horizontal, but in a tilted plane, as shown in the next section.

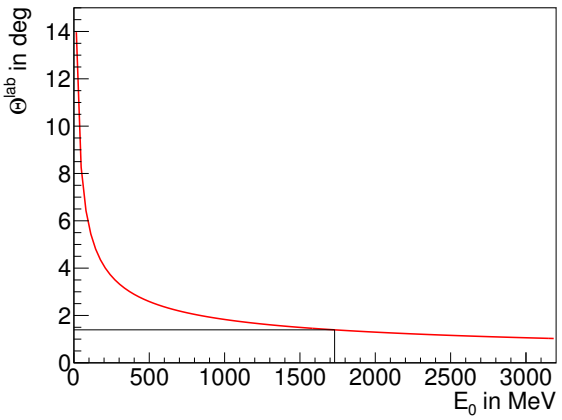

Figure 4.5: Opening angle of the cone of scattered symmetric Møller pairs in dependence on the primary electron beam energy, E_0. Marked with black lines is the "magic energy" of 1.73 GeV and the corresponding opening angle.

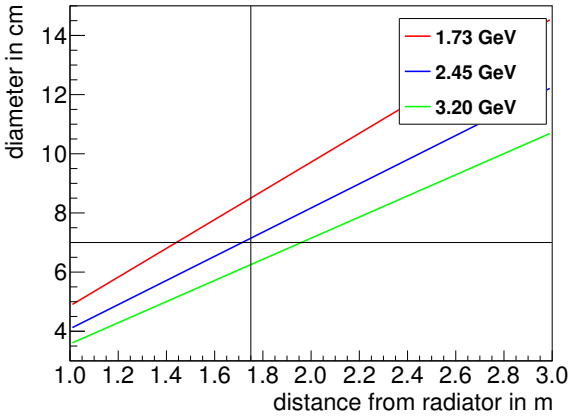

Figure 4.6: Diameter of the scattering cone against distance from the radiator for different primary beam energies. Marked with the vertical black line is the distance to the backside of the tagging magnet, marked with the horizontal black line is the gap size of the tagging magnet.

4.5.2 Simulation

At the beginning of this thesis it was clear that a Møller polarimeter, constructed like the polarimeter of the Crystal-Barrel experiment [Kam10], will not fit in the restricted space at the BGO-OD experiment. To verify that it is possible to build a polarimeter, without modifying the tagging magnet, different polarimeter configurations were simulated. In this section the simulation of the final design is presented, as well as how the effective analyzing power, a_{zz}, is determined. To perform the simulation. the analysis framework ExPlORA[3], based on ROOT [BR97] and Geant4 [Ago+03], is used. The distributions of Møller and post-bremsstrahlung electrons were investigated.

The simulated geometry includes the tagging magnet iron, aluminum vacuum chamber, as well as the capton foil closing the vacuum volume of the tagging magnet. All dimensions were taken from measurements taken on the outside of the tagging magnet. The wall thickness of the vacuum chamber is estimated from the different gap sizes of the BGO-OD tagging magnet (7 cm) and Crystal-Barrel tagging magnet (10 cm), as both magnets are of the same model, with the only difference that the vacuum chamber of the Crystal-Barrel tagging magnet was removed. The magnetic field is taken from the measurements of Andreas Balling [Bal13] of the magnetic field of the tagging magnet of the Crystal-Barrel experiment. Both magnets are of the same model, with only nonmagnetic material added, so the magnetic field map is expected to be the same. From comparisons between the simulations (using the same field map) and measurements of the tagging detector, no significant deviations were found [Bel16]. Therefore, the assumption that the field map also fits the tagging magnet of the BGO-OD experiment is considered valid. This field map only consists of three x-z layers taken at y = 0, -1.41 and 1.41 cm with the beam axis as x = 0, y = 0, so the values of the field map were linearly interpolated between the layers and extrapolated outside of ±1.41 cm. Also included in simulation are the concrete floor and the electron beam dump, as well as the scintillators and the aluminum structure of the tagging detector. The implemented geometry is shown in figure 4.7.

To find the optimal positions for the Møller detectors, a test plane was added to the simulation at

[3] **Ex**tended **Pl**uggable **O**bjectoriented **R**OOT(ified) **A**nalysis, developed by the CBELSA/TAPS collaboration (version from 2011): C. Schmidt, A. Suele, J. Hartmann, U. Thoma et al. Extended by the BGO-OD collaboration [Fre16]

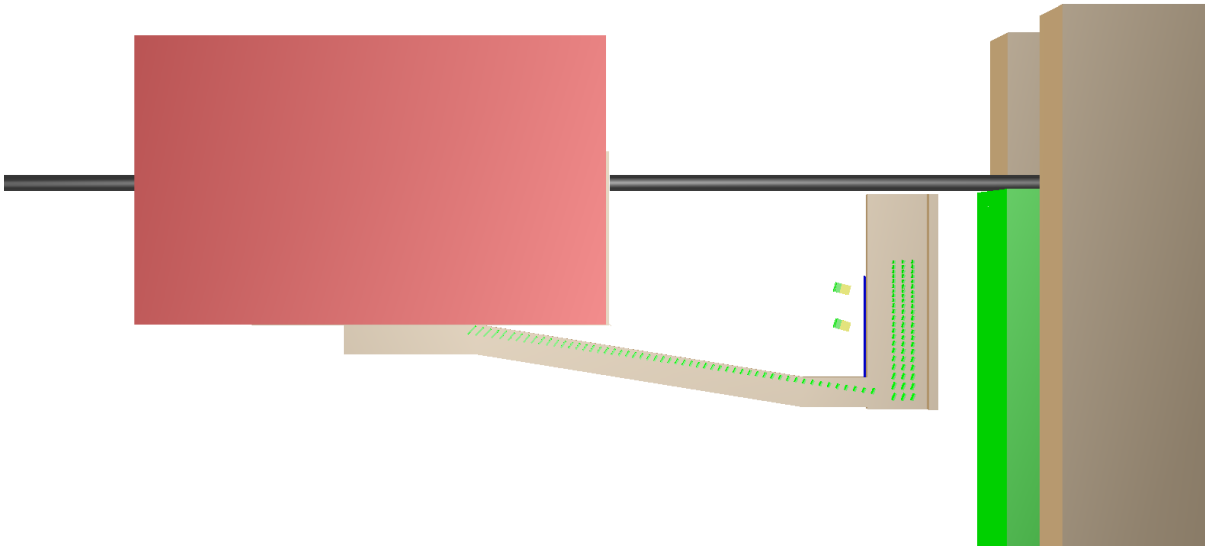

Figure 4.7: Implemented geometry in the simulation. In red the tagging magnet. Below and right of the tagging magnet in gray, the frame of the tagging detector. In green inside the frame of the tagging detector, the scintillators of the tagging detector. In blue in front of the vertical part of the tagging detector, the scintillating fibers of the argus detector. In front of the ARGUS detector, in yellow, the lead glass of the Møller detectors is shown with the green lead in front. Right of the tagging detector the lead and concrete of the electron beam dump is shown. The beam pipe is shown in black.

the position where possible detectors can be included. When a simulated particle hit this test plane the xy-position of this hit was added to a two-dimensional histogram. By simulating symmetric Møller electron pairs starting from the radiator position, according to the kinematics of the Møller scattering (from section 4.4.1), a circle of hit-positions is expected to be seen in the histogram. Due to the inclusion of the electron beam divergence[4] and beam spot size[5], the circle is expected to have a finite line width. Due to the Lorentz boost, the diameter of the scattering cone varies with the primary electron beam energy. As the maximum polarization can be achieved at a beam energy of 1.73 GeV and this energy will be most probably used for later experiments, the simulation was performed with this energy. The actual result of the simulation is not circular as one would expect from the kinematics (section 4.4.1), but two segments of a circle. Figure 4.8 shows the electron hit position. On the left and the right side in the histogram, smaller than −4.5 cm and larger than 4.5 cm, the electrons hit the wall of the vacuum chamber and are scattered away and are not seen in the histogram.

In addition to the Møller electrons, post-bremsstrahlung electrons were simulated. Identifying Møller electron pairs in between post-bremsstrahlung electrons is very challenging. With a typical coincidence gate of $t_{1/2} = 5$ ns per channel and a pessimistic post-bremsstrahlung electron rate approximation of 1 MHz, in the range of symmetric Møller electrons, the rate of accidental coincidences would be:

$$N_{acc} = (t_1 + t_2) N_1 N_2 = 10\,\text{kHz}, \tag{4.18}$$

which is higher than the expected rate of symmetric Møller electrons. Therefore this would completely spoil the polarization determination and introduce big systematic errors in the determination

[4] Beam divergence is taken from the fit of the coherent bremsstrahlung spectrum by Andreas Bella. The determined value is: $\nabla_x = 0.3$ mrad and $\nabla_y = 0.07$ mrad

[5] Beam spot size is taken from wire scans of the electron beam. The determined values are: $\sigma_x = 1$ mm and $\sigma_y = 1.5$ mm

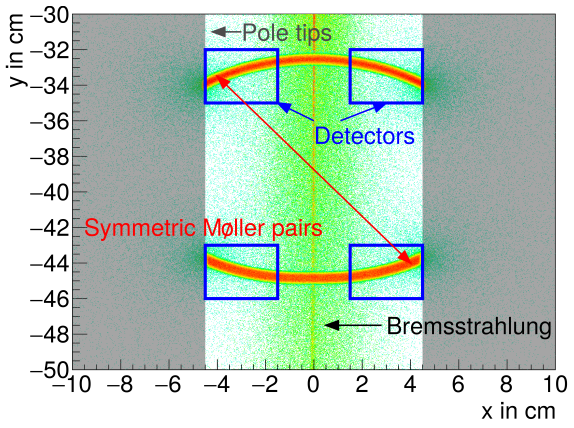

Figure 4.8: Hit distribution in the plane of the Møller detectors of simulated symmetric Møller events and simulated bremsstrahlung events.

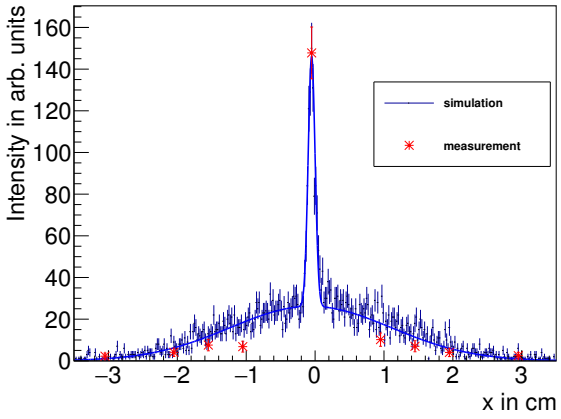

Figure 4.9: Simulated and measured post-bremsstrahlung electron beam profile.

of the degree of polarization. The detectors should therefore not be placed within the range of the post-bremsstrahlung electrons. To verify the simulation of post-bremsstrahlung electrons a dedicated measurement was done. In this measurement two lead glass detectors were moved in 1 cm steps towards the post-bremsstrahlung electron plane.

In figure 4.9 the measured rates are normalized to the extracted current from the accelerator and plotted in comparison to the simulated distribution. Measured and simulated data were scaled to the same peak height. The simulated data can described by the sum of two Gaussian functions, one for the post-bremsstrahlung electron peak and one for the broader background. The Gaussian fitted to the peak has a σ of 0.5 mm, and the one fitted to the background a σ of 1.2 cm. It seems that the background predicted by simulation is larger than the measured one. This might be caused by counting problems of the test detectors in the peak region, where a mean rate of 100 kHz was measured.

To be on the safe side the Møller detectors are placed outside the region of ±1.5 cm around the post-bremsstrahlung electron plane. The remaining space of ±(1.5 cm to 4.5 cm) can be used to position the detectors.

Simulating asymmetric Møller electrons in addition to the symmetric ones, the acceptance of the simulated detector setup in scattering angle and momentum of the scattered electrons can be determined. The effective analyzing-power a_{zz} of the setup, can also be measured by calculating the analyzing-power per scattering angle bin and taking the weighted average.

To cover the parts of the circle of symmetric Møller electrons, four detectors with a surface area of $3{\times}3\,\mathrm{cm}^2$ are needed. They are positioned as indicated in figure 4.8. With this setup the scattering angles and momenta of the scattered particles are detected as shown in figure 4.10a and 4.10b.

The results from this simulation, performed for different primary electron beam energies E_0, are listed in table 4.1.

4.5.3 Møller Target

To determine the degree of polarization of the electron beam with Møller scattering, the electron beam needs to be scattered off a polarized electron target with known polarization. One of the easiest ways to get a polarized electron target is to use a magnetized ferromagnetic foil, because the magnetization is related to the polarization of the electrons via the gyromagnetic moment, g'. In a ferromagnetic foil

E_0	a_{zz}	Δa_{zz}
1.24 GeV	-0.7763	0.0052
1.73 GeV	-0.7772	0.0044
2.45 GeV	-0.7760	0.0041
2.90 GeV	-0.7748	0.0040
3.20 GeV	-0.7741	0.0040

Table 4.1: Effective analyzing powers calculated in simulation for different primary beam energies and the corresponding statistical error.

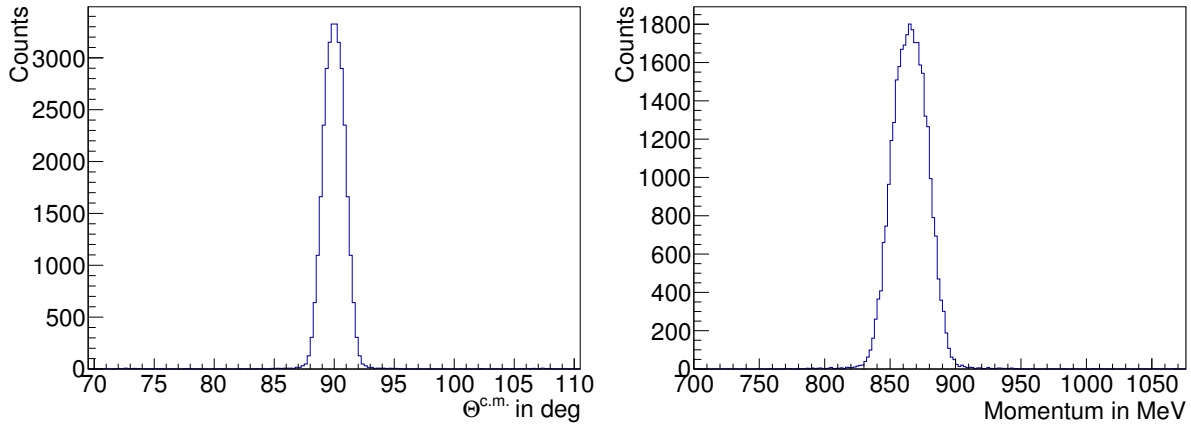

(a) $\Theta^{c.m.}$ distribution

(b) Momentum distribution

Figure 4.10: $\Theta^{c.m.}$ and momentum distributions of detected Møller pairs, determined in simulations, for E_0 = 1.7 GeV. In each histogram both detected electrons are filled.

the polarizable electrons are the uncoupled ones, those without a spin partner. Therefore the maximum degree of polarization corresponds the the number of uncoupled electrons divided by the total number of electrons per atom. For example iron has 26 electrons, 24 of them populate the K, L, M shells as spin couples. The remaining two remain uncoupled in the N shell. Therefore the maximum electron polarization achievable in iron is about $2/24 = 8.3\,\%$. To decide on a target material one can compare the maximum polarizabilities of different materials. In figure 4.11 magnetization curves for different ferromagnetic alloys is plotted, from which one can read off the maximum magnetization. From the plotted curves, Vacoflux 50 has the highest magnetization, and also saturates at smaller magnetic fields. Therefore this material was chosen to be used as a Møller target. Vacoflux 50 is a soft magnetic cobalt-iron-alloy, composed of 49.0 % cobalt, 1.9 % vanadium and 49.1 % iron. The saturation of the magnetization makes the measurement robust against fluctuations of the applied current.

The ferromagnetic foil can be magnetized in two different orientations: in plane and out of plane. To magnetize a iron foil out of plane to saturation, a magnetic field of 2.25 T is needed. Other materials require similar field strength. As this is the saturation magnetization of iron, this field strength can not be achieved by placing the foil in the gap of a magnet with iron core, where the field strength must be lower than within the iron core. Therefore a super conducting magnet, with all the required infrastructure, would be needed. As this is no option for the BGO-OD experiment, out of plane polarization is not applicable for this Møller target.

For in-plane magnetization only a small magnetic field of about 100 Gaus is needed. This field can be produced easily by a solenoid within the vacuum tank. Still there was not enough space available

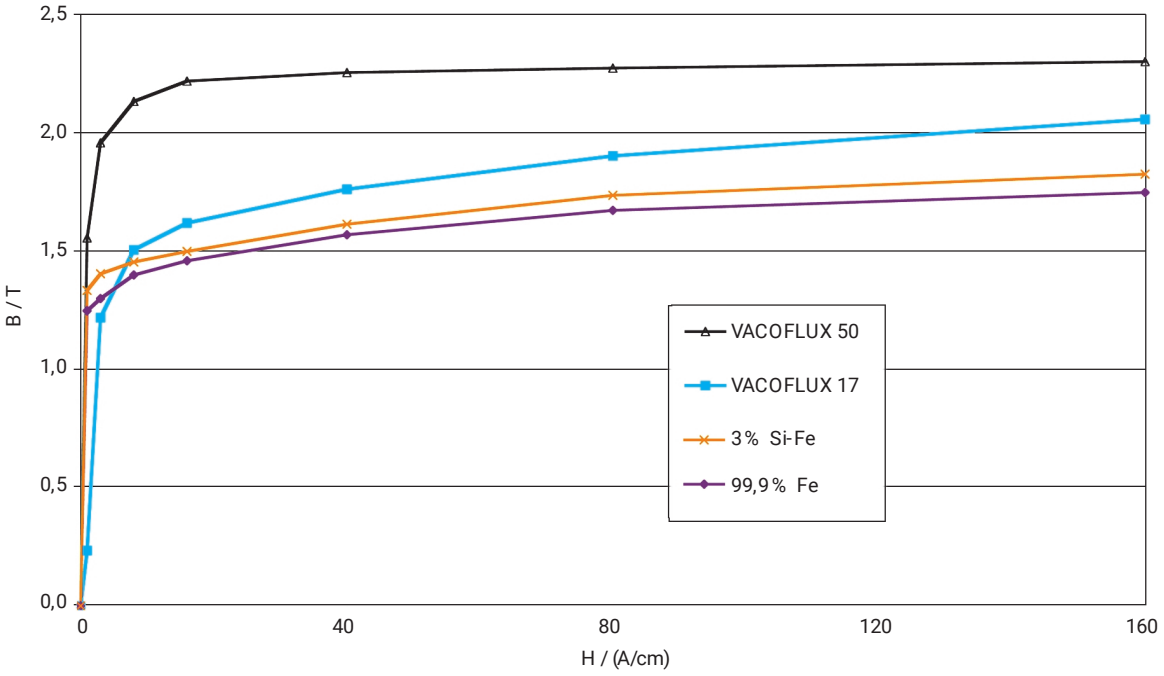

Figure 4.11: Comparison of initial magnetization curves of different ferromagnetic alloys, taken from [VAC].

in the existing vacuum tank for this method. Therefore the existing vacuum tank was replaced by one providing more space on the inside, while still fitting in the same space between tagging magnet and beam position cavity. The new vacuum tank, built as part of this thesis, is described in appendix B.

The disadvantage of in-plane magnetization for longitudinal foil polarization, is that the foil cannot be oriented perpendicular to the electron beam anymore. At the BGO-OD experiment the foil will be oriented at an angle of $\alpha = 20°$ to the beam axis, as shown in figure 4.12, similar to other Møller polarimeters where the in-plane polarization method is used, e.g. [Kam10]. The angle of 20° is chosen such that the electron beam cannot hit the solenoid nor the target tray. Due to the angle between polarization plane in the ferromagnetic foil and the electron beam, equation 4.17 needs to be modified to:

$$A_{zz} = a_{zz} P_z^{beam} P^{target} \cos\alpha + a_{xx} P_x^{beam} P^{target} \sin\alpha. \tag{4.19}$$

Where P_z^{target} was replaced by $P^{target}\cos\alpha$ and P_x^{target} was replaced by $P^{target}\sin\alpha$. When measuring the polarization at angles α and $-\alpha$ the second term of formula 4.19 can be eliminated by averaging over both measurements. This results in equation 4.20 for the degree of electron beam polarization.

$$P_z^{beam} = \frac{A_{zz}(\alpha) + A_{zz}(-\alpha)}{2 a_{zz} P^{target} \cos\alpha} \tag{4.20}$$

To operate the solenoid magnet, a bipolar power supply with USB interface is used. This power supply, a KORAD KA3005P [SHE], is connected to a Raspberry Pi 1 B+ [Ras] single board computer, which provides network access to control the power supply via the experiment slow-control. The power supply is operated in constant current mode with a current of 1.5 A, which is well above saturation [Brü14].

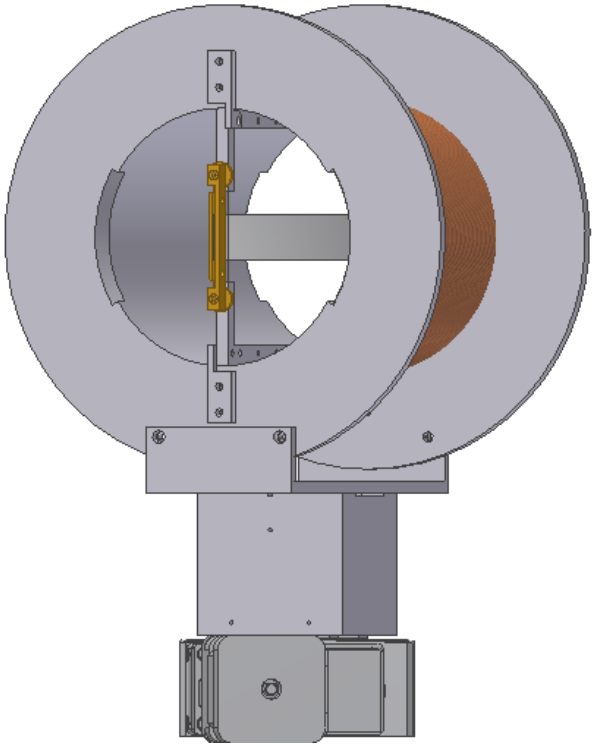

Figure 4.12: Schematic drawing of the Møller target foil inside the solenoid magnet coil, on top of the rotation stage.

Method of Determination of Polarization from Magnetization

For the determination of the polarization degree of the target foil, an inductive method was chosen. These measurements were performed on a set of Vacoflux 50 [VAC] foils with different thicknesses during the diploma thesis of Holger Eberhardt [Ebe06] and the bachelor thesis of Tobias Brück [Brü14].

The degree of target polarization is defined as the asymmetry of parallel and anti parallel electron spins in the target:

$$P^{target} = \frac{N_+ - N_-}{N_+ + N_-}$$

, where N_+ is the number of spins oriented in the predominant direction, and N_- is the number of spins oriented against the predominant direction. When neglecting the orbital momentum, the degree of polarization is also given by the ratio of the spin caused magnetization M_S, and the maximal possible magnetization M_{max}:

$$P^{target} = \frac{M_S}{M_{max}}. \tag{4.21}$$

Where M_{max} can be calculated from:

$$M_{max} = N_e \cdot \mu_B, \tag{4.22}$$

where N_e is the number of electrons per volume and μ_B the Bohr magneton.

When also considering orbital momentum L, one has to replace M_S in equation 4.21 by the total magnetization $M = M_S + M_L$. With the gyromagnetic moment $g\prime$ it is possible to disentangle both

contributions:

$$g' = \frac{M_S + M_L}{L + S}. \tag{4.23}$$

By expressing the angular momenta by the caused magnetization, one can solve equation 4.23 for M_S. With:

$$S = \frac{1}{2} M_S, L = M_L, \tag{4.24}$$

one obtains:

$$M_S = \frac{g\prime - 1}{g\prime} 2M. \tag{4.25}$$

Which can be inserted into 4.21:

$$P^{target} = \frac{g' - 1}{g'} 2 \frac{M}{N_e \cdot \mu_B}, \tag{4.26}$$

where N_e is given by:

$$N_e = \frac{Z N_A \rho}{A}, \tag{4.27}$$

where Z is the number of charged nucleons, ρ the density of the target material, N_A the Avogadro constant and A the molar mass.

With equation 4.26 it is possible to determine the degree of polarization from the measured magnetization of the target material and some constants.

Determination of Magnetization

To measure the magnetization of the target foil the method described in [Ebe06] is used.

The target foil is placed in an invertible solenoid magnetic field. When inverting the magnetic field, a current is induced in the target foil for the time of the inversion. This current spike is measured with a pick-up coil around the target foil. The integral of the voltage induced in the pick-up coil is equal to the total change of the magnetic flux:

$$\int dt U_{ind} = -\Delta\Phi \cdot n = 2n \cdot \Phi. \tag{4.28}$$

$\Phi = \int_A \vec{B} d\vec{A}$ is the magnetic flux through the pick-up coil and n the number of windings of the pick-up coil. This flux is composed of the flux through the target foil, but also the flux through the air inside the pick-up coil. Therefore Φ is given by [Ebe06]:

$$\Phi = x^{foil} B + (x^{air} - x^{foil}) \mu_0 H^{coil}. \tag{4.29}$$

Where x^{foil} is the cross section of the target foil, x^{air} is the cross section of the air within the coil, μ_0 is the vacuum permeability and H^{coil} is the strength of the magnetic field inside the pick-up coil.

By using the following relation for the magnetic flux density:

$$B = \mu_0 (H^{foil} + M) \tag{4.30}$$

and the magnetic flux without target foil:

$$\Phi_0 = \frac{1}{2} \int dt U^0_{ind} = x^{coil} \mu_0 H^{air}$$

one can obtain the magnetization, M, by taking the difference:

$$\begin{aligned}\Phi - \Phi_0 &= \frac{1}{2}\left(\int dtU_{ind} - \int dtU^0_{ind}\right) \\ &= \mu_0\left[x^{foil}M - x^{foil}(H^{coil} - H^{foil}) - x^{coil}(H^{air} - H^{coil})\right].\end{aligned} \tag{4.31}$$

The terms $x^{foil}(H^{coil} - H^{foil})$ and $x^{coil}(H^{air} - H^{coil})$ are small and therefore are neglected in the following calculations. Nevertheless this simplification has to be considered in the determination of the systematic error, as it was done in [Ebe06].

By solving equation 4.31 for M and inserting it into equation 4.26 one obtains the target foil polarization from the integral of the induced voltage when inverting the field of the solenoid magnet:

$$P^{target} = \frac{A}{ZN_a\mu_B\mu_0}\frac{g'-1}{g'}\frac{1}{n}\frac{1}{x^{foil}\rho}\left(\int dtU_{ind} - \int dtU^0_{ind}\right).$$

Setup to Measure the Magnetization

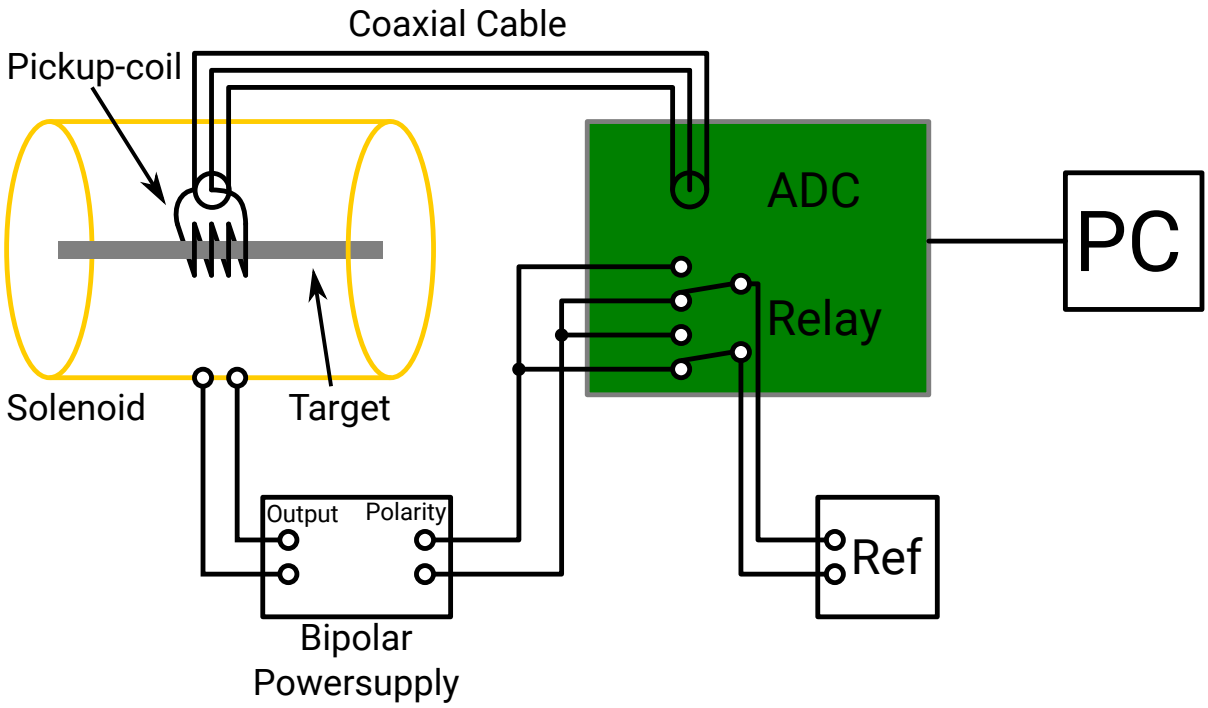

Figure 4.13: Schematic drawing of the setup to determine the target foil magnetization.

The measurement setup was built by Holger Eberhardt to measure the magnetization of the target foil of the Crystal Barrel Møller polarimeter [Ebe06]. The solenoid magnet used in the BGO-OD Møller polarimeter is used to provide the magnetizing field. A pick-up coil with 1000 windings is connected to an 18 bit ADC [6] on a readout board via a shielded cable. The readout board is connected the parallel port of a PC. Via the PC connection, a relay on the readout board can be used to change to polarity of the solenoid magnet. To avoid high currents on the readout board, the solenoid is driven by a Kepco

[6] MAX132[Max]

BOP36-5M bipolar operational power supply/amplifier, and only the reference voltage for this power supply is controlled by the readout board. The reference voltage is chosen such, that it is just sufficient to control the bipolar power supply and is provided by a Voltcraft PS 3610 DC power supply. A schematic drawing of the setup is shown in figure 4.13.

Results of the Determination of Target Polarization

For the Møller polarimeter of the BGO-OD experiment foil number 5 from the foils used in the measurements of T. Brück [Brü14] and H. Eberhardt [Ebe06] is used. T. Brück determined the degree of polarization at saturation of this foil to:

$$8.282\,\% \pm 0.070\,\%.$$

The different contributions to error of the determination of the target polarization might not be independent of each other. Therefore a quadratic summation of the different errors might not be correct. In table 4.2 the different contributions are listed, together with their linear and quadratic sum. The error above is given by the quadratic sum of the different error contributions.

Error cause	Relative error in %
Measurement of foil length l	0.25
Measurement of foil mass m	0.1
Uncertainty of g'	0.7
Error of the measurement of U_{ind}	0.28
Correction due to the demagnetizing field	0.28
Total error (linear summation)	1.61
Total error (quadratic summation)	0.85

Table 4.2: Summary of error contribution to the measurement of the Møller target foil polarization, determined by [Brü14].

4.5.4 Møller Detectors

Detectors for Møller polarimeters were already built for several experiments. Often lead glass is used in these detectors. Lead glass does not scintillate and produces light by Cerenkov radiation [Čer37]. In the environment most Møller polarimeters are built, many low energetic particles are produced due to the high flux of the primary electron beam. Because of the intrinsic threshold of a Cerenkov detector, all low energetic particles ($p_{thresh} = \sqrt{c_0^2 m_e^2/(n^2+1)} \approx 15.8\,\text{MeV}$ [Mic96]) do not even produce light in the detector and therefore can not produce unwanted signals. Scintillating detectors can produce signals for electrons of less than 10 keV. During the diploma thesis of Holger Eberhardt [Ebe06] lead glass and plastic scintillator materials were tested for the Crystal Barrel Møller polarimeter and it was found that lead glass is best suited for this environment. At the BGO-OD experiment, lead glass[7] is therefore also used for the detectors of the Møller polarimeter.

The detectors are installed directly in front of the tagging detector and ARGUS, at the x and y positions indicated in figure 4.14. To gain about 15 cm of additional space, the photomultiplier tubes of the detectors are mounted sideways. The detectors were assembled in the bachelor thesis of Georg

[7] SF-5 lead glass of previous experiment produced by JENAer GLASWERK SCHOTT & GEN.

Scheluchin [Sch13]. In addition he investigated how to optimize the light output of the detectors. It was found that using a prism to deflect the light to the photomultiplier tube and painting the lead glass and the prism white, for diffuse reflection, provided the best results. Putting the photomultiplier tube sideways has a second advantage. The photomultiplier tube is located in the "shadow" of the tagging magnet iron and therefore shielded from particles originating from the bremsstrahlung radiator. This reduces the amount of background hits in the detector.

The active volume of the four detectors are $3 \times 3 \times 3\,\mathrm{cm}^3$ lead glass cubes. The lead glass cubes were water jet cut. They were not polished afterwords, as all visible faces were later painted white for diffuse reflection anyway. A prism [Kni] is glued to each lead glass cube with optical cement. The light produced by the particles is detected with a 9111B photomultiplier tube from ET Enterprises [ET], which is attached to the prism by a silicon cookie. The assembly of one detector is shown in figure 4.15. Electrons hitting the detector will produce an electromagnetic shower. In lead glass the maximum of the energy deposition by the electromagnetic shower, and therefore also of the produced Cerenkov light, is reached after ~4.9 radiation lengths [Oli+14, eq. 32.37][8] of lead glass. With one radiation length equal to 1.265 cm, the maximum of the energy deposition in the electromagnetic shower exceeds the 3 cm of lead glass. By adding 1.5 cm of lead, corresponding to 2.67 radiation lengths, in front of the lead glass cube, the electromagnetic shower is first produced in the lead, and therefore more particles contribute to the Cerenkov light in the lead glass. With the addition of the 1.5 cm of lead, and the prism, and painting the lead glass cube and the prism white, increased the signal amplitude of each photomultiplier tube by a factor of 2 [Sch13].

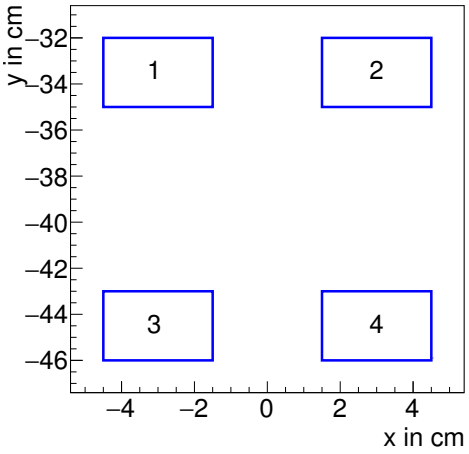

Figure 4.14: Arrangement of the 4 Møller detectors in the x-y-plane. $(x, y) = (0, 0)$ corresponds to the beam axis.

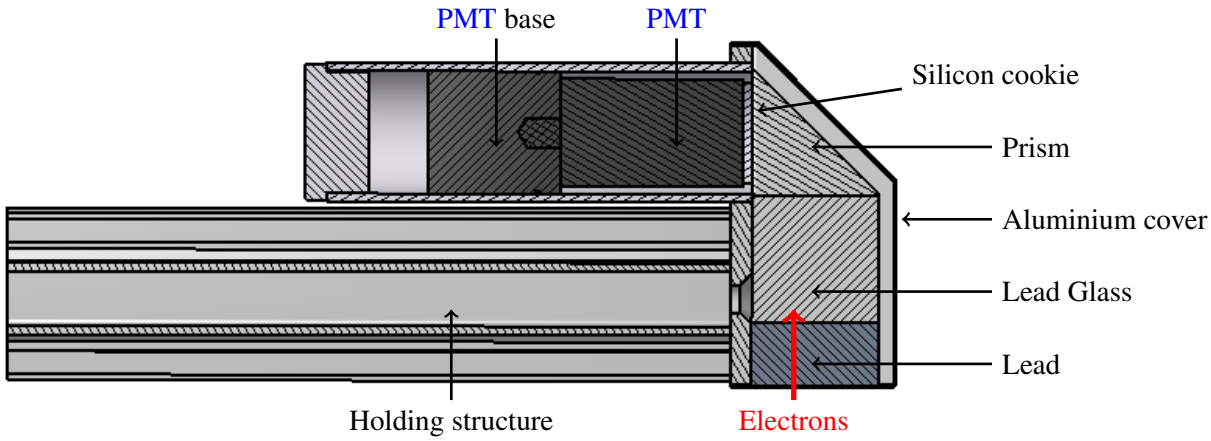

Figure 4.15: Schematic cut through drawing of one Møller detector assembly.

The processing of the signals of the four detectors is done by a jDisc module. The jDisc, as already mentioned in section 3.2.1, is a TDC implemented in a FPGA module, using a discriminator mezzanine

[8] Using $y = \frac{E}{E_c}$, E: 865 MeV and E_c: from http://pdg.lbl.gov/2015/AtomicNuclearProperties/HTML/lead_glass.html

as input. The discriminator mezzanine contains a ToT discriminator that converts the analog signal, produced by the detector, to a digital signal, if it exceeds a certain threshold. The length of the produced digital signal corresponds to the time that the analog signal exceeded the discriminator threshold. Both edges of this digital signal are recorded by the TDC logic in the FPGA, so that the ToT can be reconstructed from the difference of the two TDC entries of both edges in the later data processing. As the ToT information is correlated to the signal amplitude, it is possible to set the discriminator threshold according to these spectra. The threshold values used for data taking are listed in table 4.3.

Detector	Threshold in mV
1	-40
2	-20
3	-25
4	-25

Table 4.3: Discriminator thresholds of the four detectors of the BGO-OD Møller polarimeter. The values are so different due to manufacturing tolerances of the PMTs.

In addition to the TDC, a 200 MHz scaler and the coincidences logic for the Møller detector is also implemented. As illustrated in figure 4.16, the coincidence between the corresponding detectors is built and scaled for each helicity setting of the accelerator individually.

To decide which helicity the electron beam currently has, two digital signals are provided by ELSA, one signal for one helicity state and one for the other helicity state labeled helicity+ and helicity-. Each signal is high as long as the corresponding helicity is provided by the electron source of ELSA. The number of coincident events corresponding to a symmetric Møller pair in two detectors, is counted individually for each helicity state by a separate scaler. When the helicity switches from one state to the other, the scaler channel switches automatically.

In addition to the helicity signal two further signals (which are not mentioned in figure 4.16) are provided by the accelerator: one signal indicating the start of the extraction of the electron beam and one for the end of the extraction. As only events occurring during the extraction of the electron beam can contain information about the polarization of the electron beam, the scaler are only active when the electron beam is extracted to the experiment. A gate signal is generated therefore from the spill start and stop signal, which gates all scaler.

These signals are provided by the ELSA infrastructure. To avoid huge ground loops, which would produce noise on the signals measured by the FPGA, they need to be electrically isolated from the experiment. This is achieved by NIM-Isolators which were developed in the framework of this thesis and are described in appendix C.

To get feedback on the degree of polarization, the accelerator operator also needs the signals from the Møller polarimeter and the tagging detector to optimize the accelerator settings. Therefore signals from the experiment have to be sent to to ELSA. These signals are transmitted to ELSA using a second NIM-Isolator. The signals sent to ELSA are:

- Or of the tagging detector channels 57 to 64,
- Or of both Møller coincidence signals,
- Or of both Møller 205 ns delayed coincidences.

Plotted in figure 4.17 is the time difference, between two corresponding detectors, from the times measured by the TDC. There is a peak close to a time difference of 0 ns and a constant background

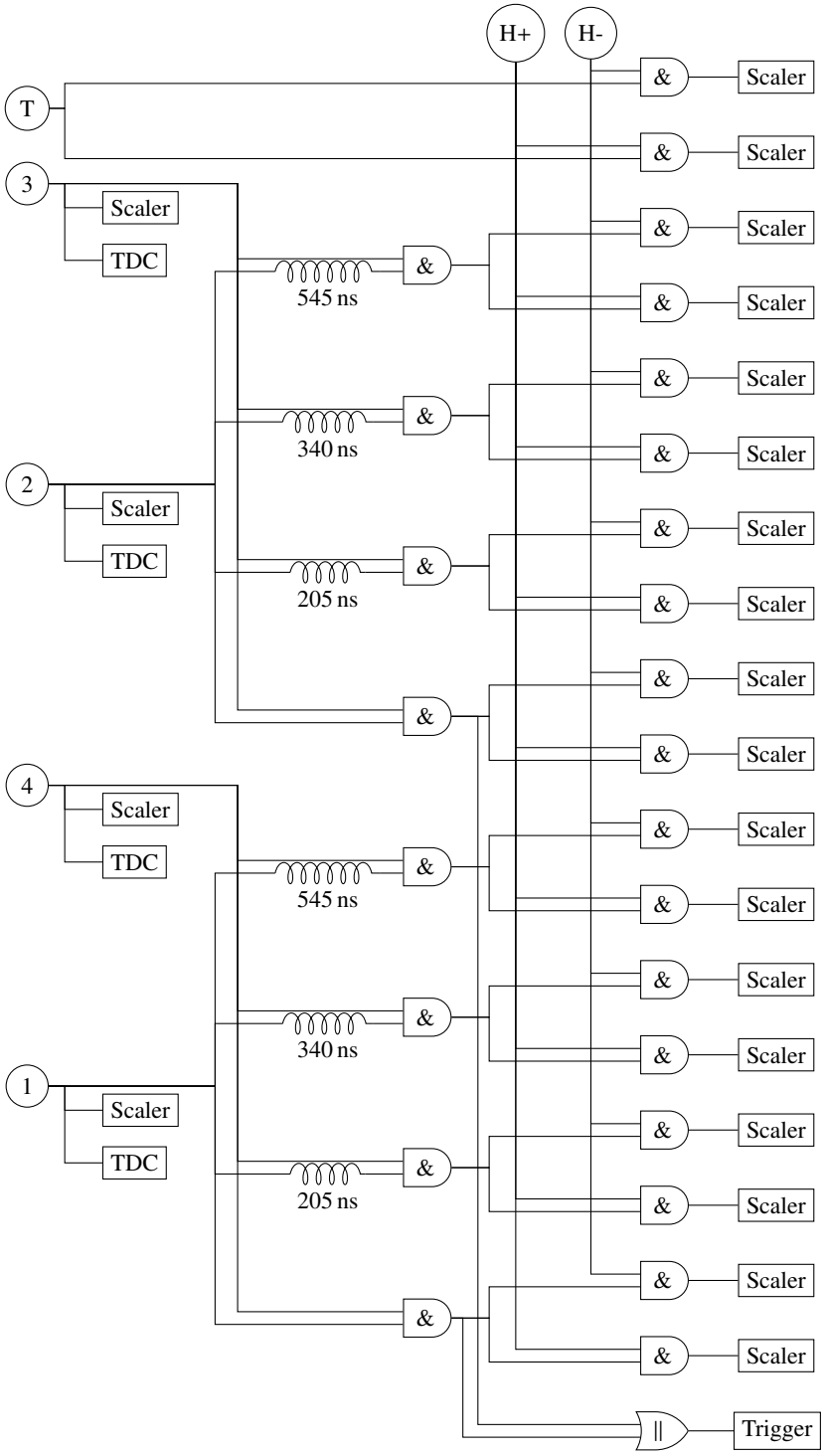

Figure 4.16: Logic diagram of the Møller detector readout. Inputs are indicated as circles. Inputs 1-4 are the signals of the four Møller detectors, input T is the or of all tagger channels for normalization and H+ and H- are the helicity signals provided by the accelerator. All inputs are discriminated by a leading edge discriminator and recorded with scaler and TDCs (not indicated for tagger and helicity inputs). Coincidences are made between discriminated signals of detectors 1 and 4, as well as detectors 2 and 3. These coincidences are counted by two scaler each, one scaler for each helicity. In addition to these coincidences, coincidences with one of the two signals delayed (by 205 ns, 340 ns and 545 ns) are made and also scaled. A trigger signal is provided by the module, which is derived from the or of the two undelayed coincidence signals. Not indicated in the figure are also the spill start and stop signals which are used to gate the scaler, so that the scaler do only count when beam is extracted to the experiment.

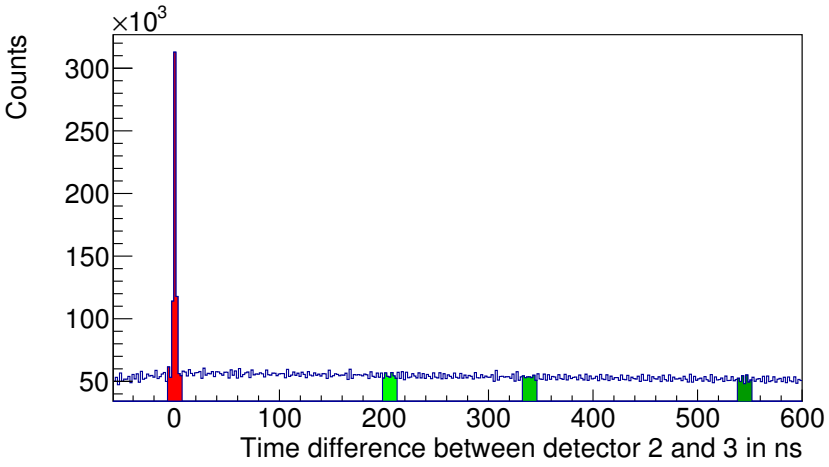

Figure 4.17: Time difference between two Møller detectors, recorded by the TDC. Clearly visible is the peak of coincident events on top of a flat background. Indicated in red is the coincidence time window. Indicated in green are the the delayed coincidences used for the sideband subtraction.

corresponding to uncorrelated events. The background beneath the peak needs to be subtracted to get the real number of coincident events. To do this it is assumed that the number of accidental coincidences is as large as the number of hits in any same-sized range beside the coincidence peak (side-band). By subtracting the side-band from the peak, one gets the number of real coincident events. In the FPGA-logic this is implemented by delaying the signal of one detector. In figure 4.17 this would shift the coincidence window to larger (or smaller depending on the order in the difference) times, indicated by green color. By counting the events in this time window one gets a measure for the number of background events below the signal peak. In the post processing of the data the amount of background can then be subtracted from the signal.

The current of the electron beam, and therefore the number of electrons, is not constant. Therefore it is required to normalize the counted events to the electron beam current. The rate of detected electrons in the tagging detector is used, as it is known that this is proportional to the electron beam current. To use this for the normalization of the count rates of the Møller detectors, the logic or of the signals of channels 57 to 64 of the tagging detector are counted by the same module as the signals of the Møller detectors. That way it is assured that the signal and the normalization is latched synchronously and therefore always the same time-span is covered by the signal and normalization.

4.5.5 Measurements

The first measurements with a polarized electron beam and the fully assembled Møller polarimeter was performed in March 2015. A second measurement was performed in June 2015 at the Crystal Barrel experiment. During the second measurement the BGO-OD Møller detector setup was compared to the existing Crystal Barrel polarimeter[Kam10]. In the first measurement in March, the setup described in the previous sections was used. In the second measurement, the BGO-OD Møller detectors were installed in the experimental area of the Crystal Barrel experiment.

Detector and Electronics Test at the Crystal Barrel experiment

During the June 2015 test measurements, the detectors were installed in between the tagging detector of the Crystal Barrel experiment and their Møller polarimeter. The required position of the BGO-OD Møller detectors in the Crystal Barrel setup was determined analogous to the method described in section 4.5.2. The setup for this measurement is shown in figure 4.18.

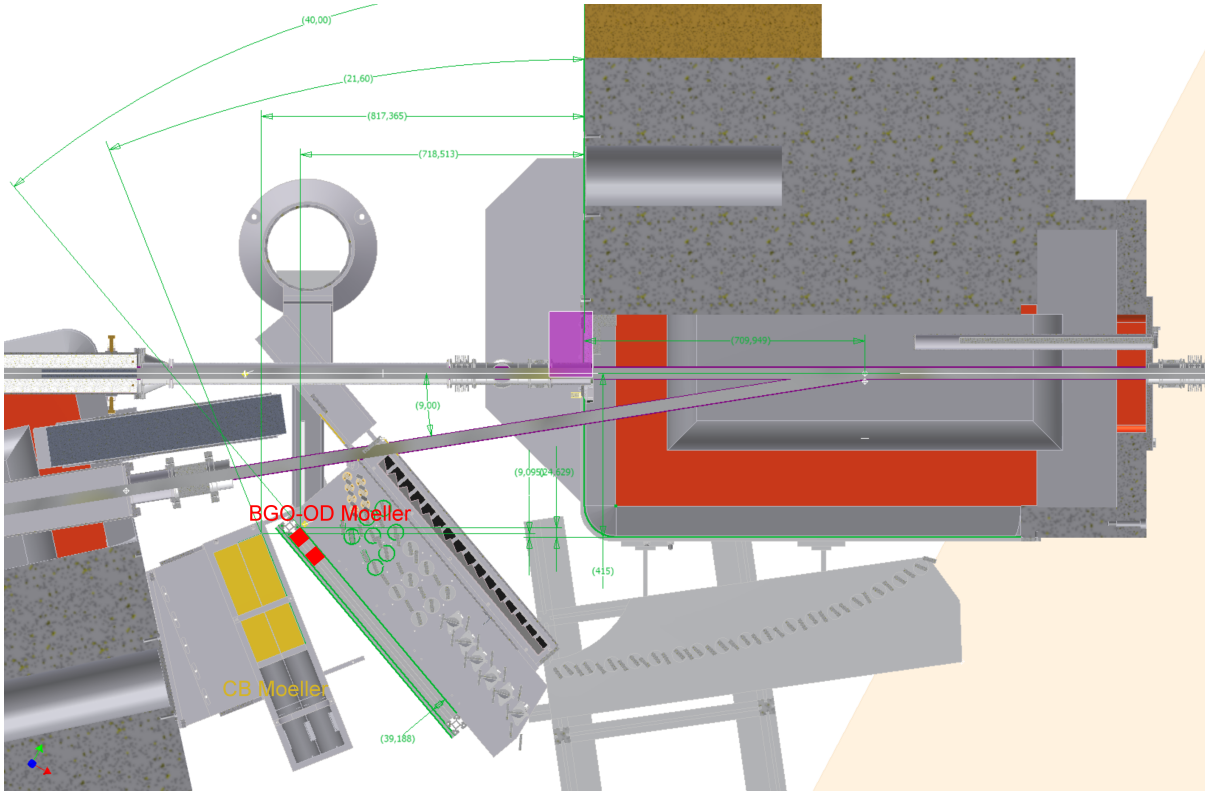

Figure 4.18: Schematic drawing of the setup of the BGO-OD Møller detectors at the Crystal-Barrel experiment. The BGO-OD Møller detectors were installed between the tagging hodoscope and the Crystal-Barrel Møller detectors. Background image provided by Dieter Walther [Wal14].

The BGO-OD Møller detectors were installed in a way that it was possible to install or remove them within 15 min. Due to this it was possible to perform several measurements with and without BGO-OD Møller detectors installed under the same electron beam conditions. This was needed to assure that the degree of polarization determined by the Crystal Barrel Møller polarimeter was not influenced by the installation of the BGO-OD Møller detectors. The only visible influence, of the BGO-OD Møller detectors on the measurement of the Crystal Barrel polarimeter, was an increase of accidental coincidences. This is expected due to the additional material installed in front of the Crystal Barrel Møller detectors.

After it was assured that the BGO-OD Møller detectors do not disturb the measurement of the Crystal Barrel Møller polarimeter, two tests were performed.

- The read-out electronics including the Møller logic of the BGO-OD Møller polarimeter was compared to the read-out electronics and logic of the Crystal Barrel Møller polarimeter. This was done by measuring the degree of polarization with the Crystal Barrel polarimeter once with the original electronics and then with the electronics of the BGO-OD Møller polarimeter under the

same beam conditions. No difference within the statistical errors was observed between both read-out electronics chains. This test was also performed because the Crystal Barrel collaboration considered modernizing the read-out electronics of their Møller polarimeter by replacing it with the same electronics used for the BGO-OD Møller polarimeter. This would reduce the amount of hardware from 3 NIM and 2 CAMAC modules to just one VME module.

- In a second test the degree of electron beam polarization, measured by the BGO-OD Møller polarimeter, was compared to the measurement of the Crystal Barrel Møller polarimeter. To exclude errors introduced by the read-out chain of the Crystal Barrel polarimeter, different read-out chains and normalizations were used. The different read-out chains were split behind the discriminator. One branch was the standard read-out chain of the Crystal Barrel Møller polarimeter with normalization to the rate detected in the tagging detector. The second branch was analyzed by the ELSA control system. The ELSA control system had direct access to a measurement of the extracted beam current. Therefore the control system can provide, in addition to a normalization to the rate in the tagging detector, a normalization to current measured by the Faraday cup in the extraction beam-line. As one can see in figure 4.19, all measurements agree within their statistical errors. What can also be seen from this plot is that the Crystal Barrel Møller polarimeter needs a shorter time for the same statistical error. Due to the much smaller size of the BGO-OD Møller detectors, compared to the detectors of the Crystal Barrel Møller polarimeter [9] this is expected.

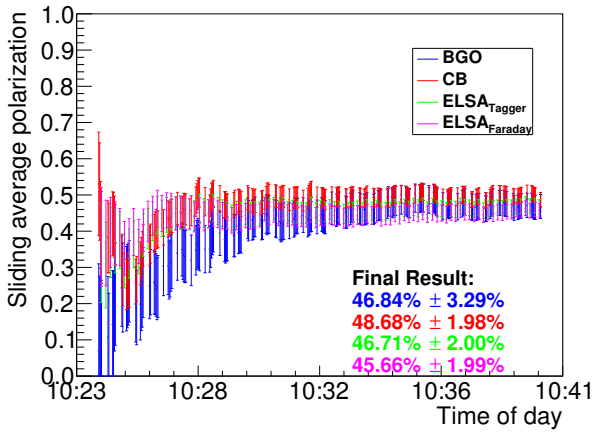

Figure 4.19: Comparison of the evolution of the sliding average degree of polarization, measured by the two different Møller polarimeters and different read out chains. Blue: BGO-OD Møller detectors with BGO-OD read out and normalization to the tagger rate. Red: Crystal-Barrel Møller detectors with Crystal-Barrel read out and normalization to the tagger rate. Green: Crystal-Barrel Møller detectors with ELSA read out and normalization to the tagger rate. Magenta: Crystal-Barrel Møller detectors with ELSA read out and normalization to the Faraday cup. The final values of each measurement are given in the bottom right box including statistical errors.

First Measurements at the BGO-OD experiment

The first measurement with the complete Møller polarimeter setup at the BGO-OD experiment was performed with an electron beam energy of 1.7 GeV. Several measurements of the degree of polarization of the electron beam were performed at different settings of the accelerator. The sliding average polarization of one such measurement is plotted in figure 4.20. After around 680 spills of the accelerator, a

[9] Size: $6.5 \times 6.5 \times 30\,\mathrm{cm}^3$ [Kam10].

polarization of 35.78 % with a absolute statistical error of 1.71 % could be measured. The accelerator was set up with a spill length of 5 s, so the 680 spills correspond to a measuring time of about 1 h.

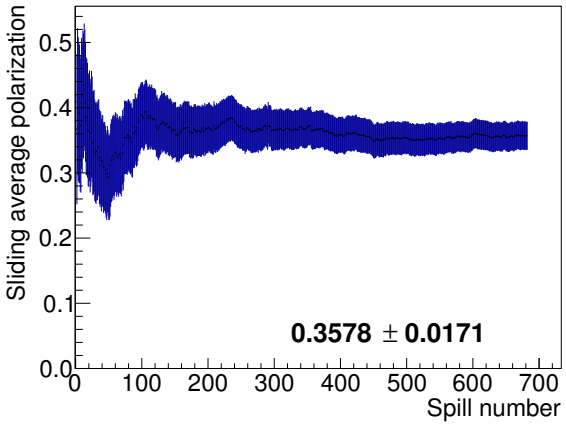

Figure 4.20: Evolution of the sliding average polarization measured in run 22740. In this measurement the degree of polarization was determined to 35.78 % ± 1.71 %.

In a second measurement, the degree of polarization of the electron beam was intentionally changed, by rotating the spin of the electron beam directly behind the electron source with the pairs of solenoid magnets mentioned in section 3.1. When rotating the spin of the electron beam, and measuring only the z-component of the polarization, one expects to measure a sinusoidal dependency on the rotation angle, as sketched in figure 4.21a. Unfortunately it was not possible to rotate the spin of the electron beam by 180° without loosing the beam. Therefore only rotation angles of −40° to 40° could be measured. The result is shown in figure 4.21b together with a sine function fitted to the data. With a reduced χ^2 of 1.25 fit describes the data well, therefore one can conclude that the determination of the electron beam polarization worked well.

Unfortunately the polarized electron beam properties were not sufficient for hadron physics experiments at the BGO-OD experiment. Shown in figure 4.22a and 4.22b are the measured electron beam profiles in the horizontal and vertical direction. The beam diameter is very large ($\sigma_y = 3.9\,\text{mm}$), in particular in the vertical direction. Usually the beam diameter is in the order of $\sigma = 1\,\text{mm}$. To improve the beam shape, the addition of further focusing magnets in the extraction beam line is required.

4.6 Systematic Errors

Every measurement has a certain uncertainty. Despite the statistical uncertainty of the polarization measurement, which can be reduced by longer measurement times, it is essential to know the systematic uncertainties. In this section several sources of systematic uncertainties are discussed.

4.6.1 Levchuk Effect

Chr. Møller based his calculations of the Møller cross section on the assumption that the momentum of loosly bound or free electrons can be neglected [Møl32, p. 557]. In [Lev94] L.G. Levchuk pointed out that neglecting the momentum of the target electron can result in “an essential overestimate of the asymmetry”, if the Møller electron pairs are selected by angle.

The momentum distribution of electrons in the target material depends on the atomic shell, where only electrons in the outer shells contribute to the target polarization. Electrons on the inner shells do

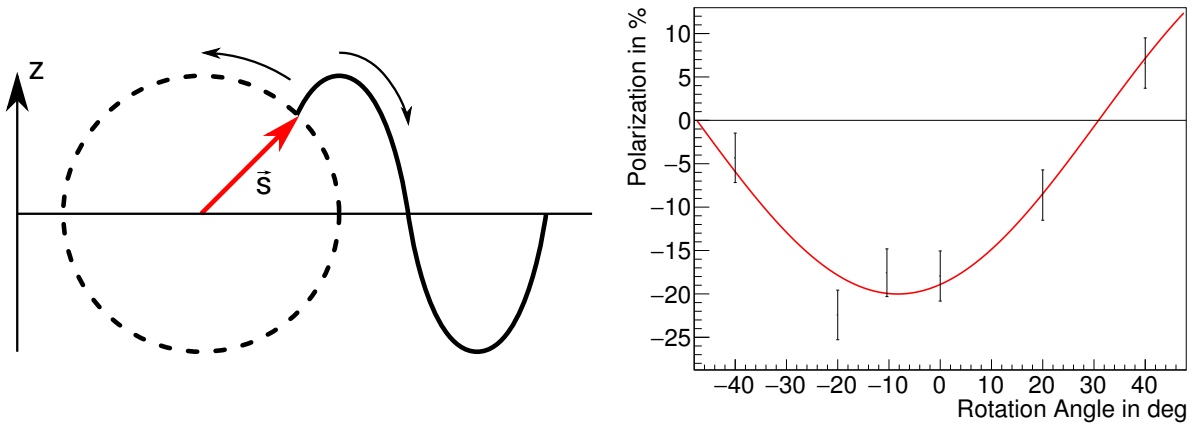

(a) Expectation

(b) Measurement

Figure 4.21: Measurement of the degree of longitudinal electron beam polarization in dependence of the rotation angle of the electron spin. In (a) the red arrow indicates the spin orientation. When rotating the spin, the projection of the z component of the spin follows a sine function. (b) presents the actual measurement results (black points), fitted with a sin function (red curve).

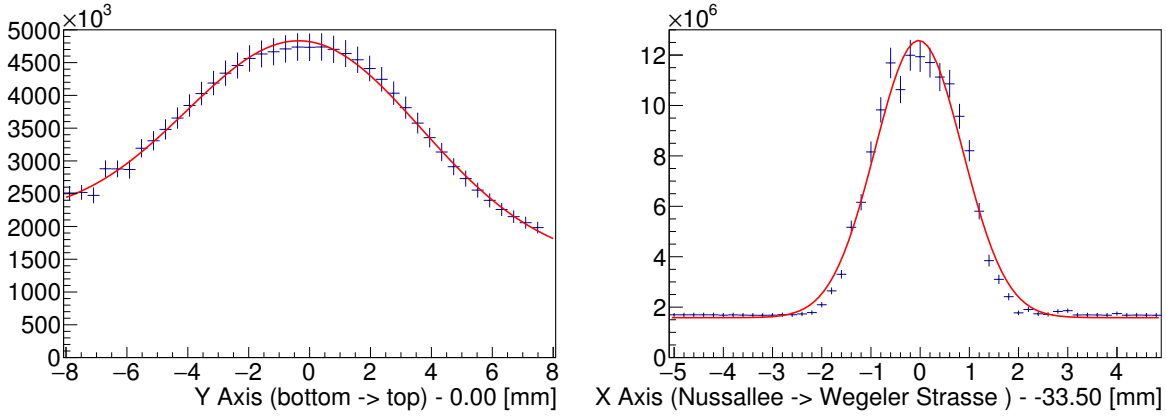

(a) Vertical electron beam profile

(b) Horizontal electron beam profile

Figure 4.22: Electron beam profile in (a) y and (b) x measured by moving a steel wire through the electron beam and measuring the total rate in the tagging detector.

not contribute, as their spins are coupled. The binding energy of the inner electrons is higher than the binding energy of the outer electrons, therefore also their average momentum is higher. This means that the unpolarized target electrons have higher average momentum than polarized target electrons. When scattering off moving target electrons instead of those at rest, the resulting scattering angles will be different. Therefore polarized and unpolarized target electrons contribute differently to the measured asymmetry, which results in a wrongly measured degree of electron beam polarization.

The BGO-OD Møller polarimeter is especially designed with this effect in mind and therefore selects the electron pairs by momentum. Due to the constrained space in the BGO-OD experimental area, also the angular acceptance of the polarimeter is constrained. To study the effect described by Levchuk on the measured asymmetry with the BGO-OD Møller polarimeter, the simulation described in section

4.5.2 is extended to include the target electron momentum distribution. As iron and cobalt (the two main components of vacoflux) differ only in one electron on the M shell, the momentum distributions for iron and cobalt are very similar. Therefore in the simulation, the momentum distributions of pure iron are used. The distribution of the electron momenta in the K and L shells are approximated by the analytic functions provided by Y.F. Chen, C.M. Kwei and C.J. Tung [CKT93]:

$$I_i(p) = 4\pi p^2 \rho_i(p) = \frac{32}{\pi} \sum_{j=1}^{2} \frac{A_{ij}\zeta_{ij}^5 p^2}{(\zeta_{ij}^2 + p^2)^4}, \tag{4.32}$$

where $i \in \{K, L\}$, p the electron momentum. $A_{i1} = 1 - A_{i2}$ and ζ_{ij} are given in table 4.4.

Element (Z)	A_{K1}	ζ_{K1}	ζ_{K2}	A_{L1}	ζ_{L1}	ζ_{L2}
Fe (26)	0.6530	23.895	28.332	0.9623	10.283	21.878
Co (27)	0.7137	25.063	29.843	0.9591	10.724	21.647

Table 4.4: Parameters for equation 4.32 from Y.F. Chen, C.M. Kwei and C.J. Tung [CKT93]

Similar to the calculations by S. Kammer [Kam10], the distribution for the M and N shells are taken by scaling the distribution of the L shell such, that the maximum of the distribution corresponds to the value given in [Kam10] and the integral is normalized to the same value as the integral of distributions for the K and L shell. To achieve this for the M shell, the momentum is scaled by $1/3.8$ and the overall function is scaled by 14.44, for the N shell the momentum is scaled by $1/18$ and the overall function is scaled by 324.00. The momentum distributions for the K, L and M shells are shown in figure 4.23.

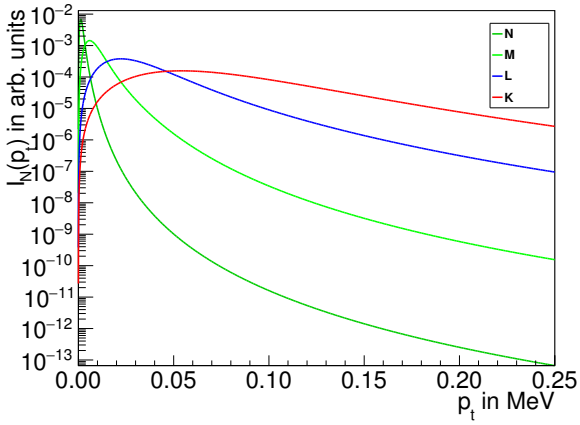

Figure 4.23: Probability distribution for the electron momenta in single shells of an iron atom, according to equation 4.32.

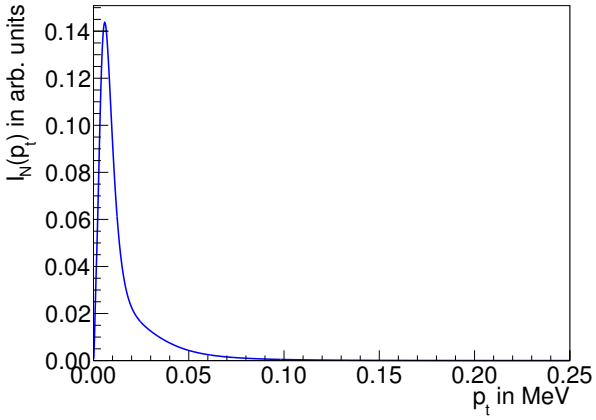

Figure 4.24: Summed probability distribution of electron momenta for 2 K shell electrons, 8 L shell electrons and 14 M shell electrons.

As the different shells are populated with a different number of electrons, when adding up the distributions, they are scaled by the number of electrons populating the particular shell. The overall momentum distribution is given in figure 4.24.

To determine the effect of a given momentum distribution on the measured asymmetry, the number of detected Møller pairs (N) are counted. When changing the momentum distribution, the effective analyzing power may change. To check that this is not the case, the effective analyzing power is determined for each momentum distribution. To determine the change in the asymmetry, one has to correlate the effect on the different atomic shells to the asymmetry. As the numerator of the asymmetry ($N^{\uparrow\downarrow} - N^{\uparrow\uparrow}$)

is affected only by the polarized electrons, and the denominator ($N^{\uparrow\downarrow} + N^{\uparrow\uparrow}$) only by the unpolarized electrons one can rewrite equation 4.17 as:

$$A_{zz} = \frac{N_N}{2N_{KLM}}, \tag{4.33}$$

where N_N and N_{KLM} are the counts originating from the N or K,L and M shells. When using formula 4.33 to calculate the relative change in the asymmetry one gets:

$$\frac{\Delta A_{zz}}{A_{zz}} = \frac{A_{zz} - A_{zz}^{Levchuk}}{A_{zz}} \overset{eq.4.33}{=} \frac{\frac{N_N}{2N_{KLM}} - \frac{N_N(1+\Delta N_N)}{2N_{KLM}(1+\Delta N_{KLM})}}{\frac{N_N}{2N_{KLM}}} = 1 - \frac{1+\Delta N_N}{1+\Delta N_{KLM}}, \tag{4.34}$$

where A_{zz} is the asymmetry unaffected by the Levchuk effect, $A_{zz}^{Levchuk}$ the effected one, and ΔN_N and ΔN_{KLM} are the relative changes in the counts due to the Levchuk effect.

When assuming that scattering off electrons in all shells is equally possible and using the relative count changes from the simulation (given in table 4.5), one can determine the expected relative error of the measured asymmetry ($\frac{\Delta A_{zz}}{A_{zz}}$) as $-0.51\,\% \pm 0.97\,\%$. With this value the contribution to the systematic error from the Levchuk effect is larger than for other Møller polarimeters (e.g. [Kam10]), but still smaller than the contribution from the target polarization measurement.

Shell	$\Delta N/N$	stat. error	eff. a_{zz}	Δa_{zz}
Without Levchuk effect	-	0.56 %	-0.7772	0.0044
K	−11.66 %	0.60 %	-0.7765	0.0047
L	−0.78 %	0.57 %	-0.7768	0.0044
M	−1.15 %	0.57 %	-0.7771	0.0044
N	−0.38 %	0.56 %	-0.7771	0.0044
2K + 8L	−3.23 %	0.57 %	-0.7767	0.0044
2K + 8L + 14M	−0.88 %	0.57 %	-0.7770	0.0044
2K + 8L + 14M + 2N	−0.42 %	0.56 %	-0.7770	0.0044

Table 4.5: Simulated relative change in the number of detected Møller pairs, depending the the atomic shell they originate from.

4.6.2 Positioning Uncertainties

The installation of the detectors was performed as precise as possible, but a misalignment in the order of 1 or 2 mm can not be excluded. The effect of such a misalignment needs to be investigated.

The positioning of the target foil is accurate with a much higher precision of 0.2 mm and therefore can be neglected, compared to the positioning uncertainties of the detectors. The uncertainty of the inclination angle of the target foil is given by the corresponding Goniometer precision. From the manufacturer's data sheet the precision of the rotary stage is given to 0.03° [New13]. The largest uncertainty of the target positioning stems from the scattering vertex position. Due to the beam spot size of $\sigma = 2$ mm and the inclination angle of 20°, the uncertainty in the z-component of the vertex will be about 3 mm. A shift of the vertex in x- or y-direction would nearly correspond to a shift of all detectors in one direction, which has a smaller effect one measured asymmetry than the asymmetric shifts investigated in this section.

To investigate the effect of these uncertainties, the simulation was performed for several misaligned configurations, shown in figure 4.25. A misalignment of 3 mm was simulated in x and y (positions a-d)

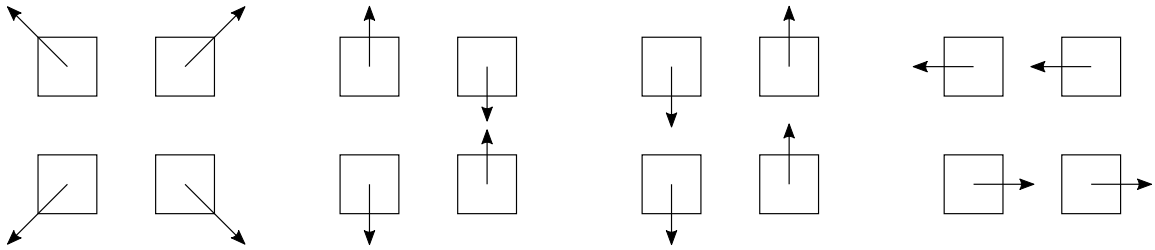

(a) (b) (c) (d)

Figure 4.25: Four possible misalignments of the BGO-OD Møller detectors.

Position	$\frac{\Delta A}{A}$
a	0.76 % ± 1.21 %
b	-0.90 % ± 1.14 %
c	-1.86 % ± 1.15 %
d	1.06 % ± 1.12 %
z	1.55 % ± 1.13 %
average	1.23 % ± 1.48 %

Table 4.6: Errors from different misalignments (a to d), shown in figure 4.25, and a misalignment of radiator position in the z coordinate.

and z (position z), including the Levchuk effect from section 4.6.1. The results of these simulations on the measured asymmetry are summarized in table 4.6. The influence of these shifts on the effective analyzing power a_{zz} is at most 0.04 % and therefore negligible.

4.6.3 Systematic Error

The accuracy of the determination of the degree of electron beam polarization (see equation 4.20) depends on the accuracy of the target polarization, $|P^{target}|$, the effective analyzing power, a_{zz}, the inclination angle, α and the count rate asymmetry, A_{zz}. The error on A_{zz} in not only determined by statistics, but also by the detector positioning.

Target Polarization

As discussed in section 4.5.3, the relative error of determining the target polarization is 1.61 % assuming linear or 0.85 % assuming quadratic summation. For the total systematic error, the target polarization error determined by linear summation of the several error contributions is used.

Effective Analyzing Power

The effective analyzing power, a_{zz}, is determined in Monte-Carlo simulations, as described in section 4.5.2. Due to the limited number of simulated events, the coefficient can only be determined within a certain error. With the statistics used to determine the effective analyzing power, the error is given as 0.56 %.

Inclination Angle

The error of the inclination angle is 0.03°, which corresponds to 0.04 % relative error.

Count Rate Asymmetry

The error of the count rate asymmetry is mainly given by the statistical uncertainty. Due to errors in the positioning, discussed in section 4.6.2, an additional systematic uncertainty of 1.23 % ± 1.48 % is added. Due to the relatively low statistical accuracy this error was determined, in the total systematic error the maximal possible value of 1.23 % + 1.48 % will be considered.

Total Systematic Error

To determine the accuracy of the electron beam polarization measurement from the different contributions, Gaussian propagation of errors is used. Using formula 4.20 one gets the equation 4.35 for the total error:

$$\Delta P_z^{beam} = \sqrt{\left(\frac{\Delta A_{zz}(\alpha)}{2a_{zz}P^{target}\cos\alpha}\right)^2 + \left(\frac{\Delta A_{zz}(-\alpha)}{2a_{zz}P^{target}\cos\alpha}\right)^2 + \left(\frac{(A_{zz}(\alpha)+A_{zz}(-\alpha))\Delta a_{zz}}{2a_{zz}^2P^{target}\cos\alpha}\right)^2 + \left(\frac{(A_{zz}(\alpha)+A_{zz}(-\alpha))\Delta P^{target}}{2a_{zz}P^{target2}\cos\alpha}\right)^2 + \left(\frac{(A_{zz}(\alpha)+A_{zz}(-\alpha))\sin\alpha\Delta\alpha}{2a_{zz}P^{target}\cos^2\alpha}\right)^2}. \tag{4.35}$$

As the actual asymmetry is needed for the calculation, the error is calculated for run 22740, with a measured asymmetry of 0.021677, which was presented in section 4.5.5. As during one run only one inclination angle was measured, equation 4.35 simplifies to equation 4.36:

$$\Delta P_z^{beam} = \sqrt{\left(\frac{\Delta A_{zz}(\alpha)}{a_{zz}P^{target}\cos\alpha}\right)^2 + \left(\frac{A_{zz}(\alpha)\Delta a_{zz}}{a_{zz}^2P^{target}\cos\alpha}\right)^2 + \left(\frac{A_{zz}(\alpha)\Delta P^{target}}{a_{zz}P^{target2}\cos\alpha}\right)^2 + \left(\frac{A_{zz}(\alpha)\sin\alpha\Delta\alpha}{a_{zz}P^{target}\cos^2\alpha}\right)^2}. \tag{4.36}$$

This results in the following value for the systematic error in absolute percent points:

$$\Delta P_z^{beam} = \sqrt{0.0097^2 + 0.0020^2 + 0.0058^2 + 0.0001^2} = 1.15\,\%. \tag{4.37}$$

Being more pessimistic about the errors and calculating the total systematic error by linear summation of the individual error contributions, gives the following systematic error:

$$\Delta P_z^{beam} = 0.0097 + 0.0020 + 0.0058 + 0.0001 = 1.76\,\%. \tag{4.38}$$

The largest contribution to the systematic error comes from the positioning uncertainty of the detectors, the second largest contribution comes from the uncertainty of the determination of the target foil polarization. The relative contributions to the systematic uncertainties are listed in table 4.7.

With the Møller polarimeter, build during this thesis, the degree of electron beam polarization of run 22740 was determined to:

$$P^{beam} = (35.78 \pm 1.71_{stat} \pm 1.15_{sys})\%. \tag{4.39}$$

Error Contribution	Absolute Error Contribution	Relative Error Contribution
Measured asymmetry	0.97 %	2.71 %
Analyzing power	0.2 %	0.5 %
Target polarization	0.58 %	1.62 %
Inclination angle	0.01 %	0.03 %

Table 4.7: Summary of the different contributions to the systematic uncertainty of the electron beam polarization measurement.

CHAPTER 5

Analysis of $\gamma p \rightarrow K^+\Lambda$ at extreme forward angles

Extensive measurements of the differential cross section for the reaction $\gamma p \rightarrow K^+\Lambda$ have been made [Gla+04; Lle+07; Lle+09; McC+10; Bra+07; Pat+16; Sum+06; Jud+14], however at extreme forward angles ($\Theta^{c.m.}_{K^+} < 20°$), there is very little data available. These extreme forward angles are very important to constrain the existing models, as presented in chapter 2. With the magnetic forward spectrometer, the BGO-OD experiment is perfectly suited to investigate this channel at these angles. With linearly and circularly polarized photon beams and the self analyzing weak hyperon decay, several observables can also be measured.

In this chapter, the differential cross section at extreme forward angles is determined, where the K^+ is detected in the forward spectrometer of the BGO-OD experiment. In the center of mass frame of this reaction, the forward spectrometer covers angles of $\Theta^{c.m.}_{K^+} < 25°$, and complements existing data, which covers angles of $\Theta^{c.m.}_{K^+} > 20°$. The data analyzed in this chapter was taken in June/July 2015, and is 250 h of data with an incident electron beam energy of 2.9 GeV. The photon beam was linearly polarized with the maximum of polarization set to 1.55 GeV, in two different polarization planes. For this analysis both polarizations were added together as no polarization information is needed when determining the cross section. In the following sections it is explained how the K^+ was identified in the forward spectrometer, how the number of reconstructed $K^+\Lambda$ events is extracted, and finally the resulting cross sections are shown and systematic errors are discussed.

5.1 K^+ Selection in the Forward Spectrometer

As a first step in the analysis, the individual detector hit positions are combined to determine particle trajectories, as described in section 3.4. All trajectories corresponding to one reaction need to be selected. This is achieved by several general timing cuts, performed on the particle tracks. These cuts are used by most analysis at the BGO-OD experiment and are listed in table 5.1. The cuts are based on the individual detector resolutions and the different flight times of the different particle types.

Track type	Involved detectors	Cut
Tagger track	tagging detector and ARGUS	±1.5 ns
Central track	BGO-ball and scintillator barrel	±5 ns
Intermediate track	SciRi	±50 ns
Forward track	SciFi2 and MOMO	-2 ns to 8 ns

Table 5.1: Timing cuts applied to the different trajectory types, and the detectors involved in constructing these trajectories.

In addition to the general timing cuts, a cut was performed to remove tracks in the forward spectrometer, which do not correspond to the event selected with the timing cuts. As the flight times of particles in the forward spectrometer are much longer than in the central calorimeter, the timing cuts must be wide and therefore still accept particles from events originating from reactions from a different beam photon. The cut is applied to the average time, t, the particle passed the MOMO and SciFi2 detectors, in dependence of β. It is given by equation 5.1 and shown graphically in figure 5.1a.

$$\beta < 1.2 - (0.15 \cdot t) \tag{5.1}$$

As all particles with the same β should pass the MOMO and SciFi2 detectors at the same time, particles which do not pass the detectors in the right time-window do not correspond to the selected event. As β is inversely-proportional to the time, t, which can also be seen in figure 5.1a. In addition to the expected $1/t$ curve, additional enhancement of events are seen in the top right area of this plot, for example at $t = 6\,\text{ns}$, $\beta = 0.8$. These events correspond to particles which do not belong to the currently considered event, and are produced from earlier or later electron bunches from the accelerator[1]. The applied cut rejects some events around $\beta = 1$, but it has shown that in this part only background events are located and no real K^+ are cut away. The influence of this cut on a β versus momentum plot for particles in the forward spectrometer is shown in figures 5.1b and 5.1c. Background events are rejected and the kaon band becomes visible between the pion and the proton band.

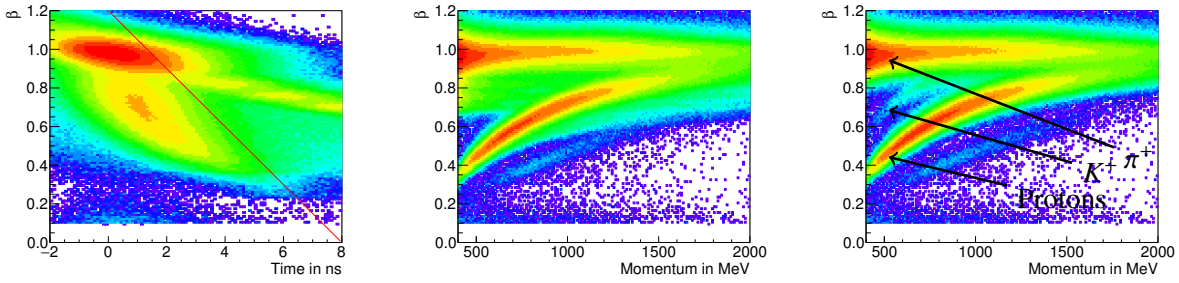

(a) (b) (c)

Figure 5.1: In (a) β of particles in the forward spectrometer against the average time the particle is detected in the MOMO and SciFi2 detectors is shown. The red line indicates the cut applied to remove particles originating from different event than the currently considered one. The result of this cut on β against momentum of a particle in the forward spectrometer is shown in (b) and (c). The situation before the cut is shown in (b), a pion and proton band is visible. The result is shown in (c), where between pion and proton band the charged kaon band is now visible.

To select K^+ in the forward spectrometer, the mass, m, of detected, positively charged particles in the forward spectrometer, is determined from their β and four-momentum, p, with equation 5.2.

$$m = \sqrt{\left(\frac{p}{\beta}\right)^2 - p^2} \tag{5.2}$$

K^+ candidates are selected by a $1\,\sigma$ cut around their mass peak. In real data the K^+ are only visible between the proton and pion mass peaks at low momenta, where the mass resolution is better than for higher momenta, as one can see in figure 5.2a and 5.2b. Figure 5.2b also shows that, at higher momenta, within the selection cut, many pions will be included. To confirm that the chosen cut also fits to kaons with higher momenta, the mass peak calculated from real data was compared to simulated data. The

[1] The bunch distance is 2 ns

mean and σ of a Gaussian fit to the K^+ mass agree between real and simulated data. It is therefore assumed that this is also valid for higher momenta.

That this cut is properly selecting the kaons also in real data, can be verified in figure 5.3. In this figure β against momentum is plotted for events, where a decay-γ of the Σ^0 of the competing reaction $\gamma p \to K^+\Sigma^0$, where the Σ^0 decays to $\Sigma^0 \to \Lambda\gamma$, was detected, as described later in section 5.3.5. This requirement suppresses the pion band in this plot. As one can see in figure 5.3, the kaon band is well within the cut, indicated by the two red lines.

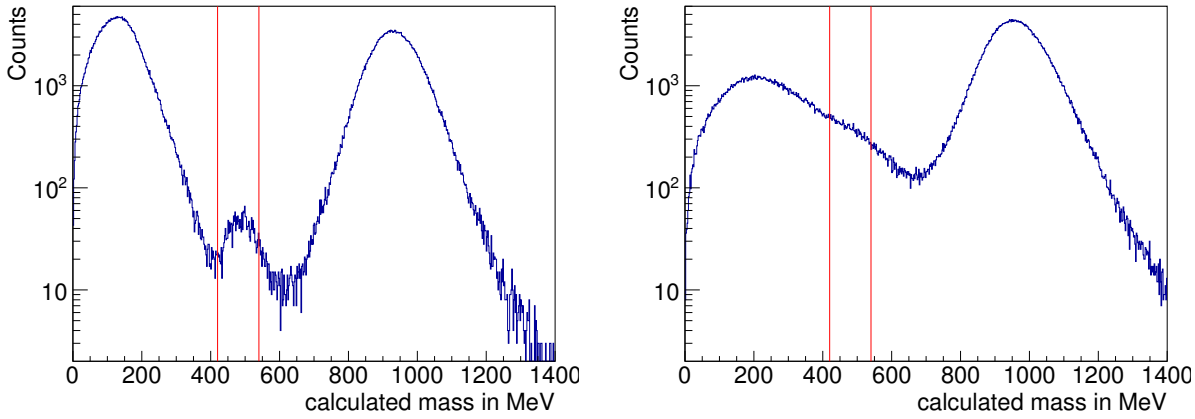

(a) p = 360 MeV to 700 MeV (b) p = 700 MeV to 1 500 MeV

Figure 5.2: Mass of the particle in the forward spectrometer is calculated from β and momentum for different momenta ranges. For low momenta (a) the kaon mass peak around 493 MeV is well visible. For higher momenta (b) the kaon mass peak can not be distinguished from the tail of the pion mass peak. The red lines indicate the cut used in the analysis to select the K^+.

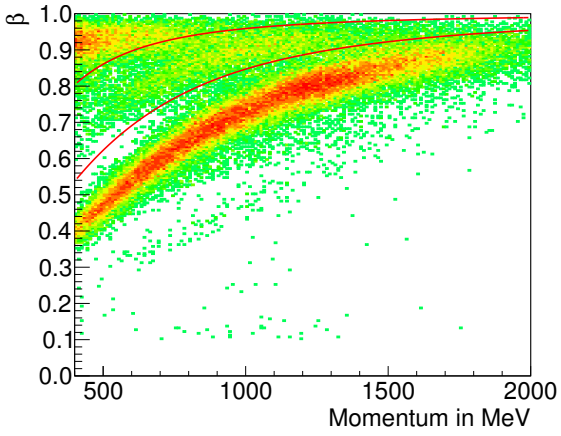

Figure 5.3: β against momentum of particles in the forward spectrometer, when detecting a $K^+\Sigma^0$ event (which is introduced later in section 5.3.5). Due to this requirement the π^+ are suppressed and one can see that the cut, indicated by the red curves, selects the K^+ well, even at momenta higher than 1 GeV.

The requirement of an additional cut, to reduce the π^+ background in this plot, indicates that without such a cut, a certain amount of π^+ contamination is to be expected in the K^+ sample. This contamination will be larger for higher K^+ candidate momenta.

To identify the final state, the missing mass to the K^+ is used. When knowing the four-momenta of the

initial state of the reaction (beam photon and target proton at rest), and the four-momenta of one or more particles in the final state, one can calculate the mass missing to achieve four-momentum conservation:

$$M_{missing} = \sqrt{(p_{initial} - p_{reco})^2}, \tag{5.3}$$

where $p_{initial}$ is the four-momentum of the initial state, p_{reco} the reconstruct four-momentum in the final state, and $M_{missing}$ the missing mass. In the following, when referring to a mass missing to a particle, the mass missing from this particle to the initial state, to achieve four-momentum conservation, is meant.

The K^+ missing mass is shown in figure 5.4a, with an additional requirement that the energy of the beam photon (E_γ) exceeds 900 MeV, which is slightly below the threshold for this reaction of E_γ = 911 MeV and therefore rejects events where $K^+\Lambda$ events cannot be produced. In this spectrum peaks are visible at the mass of Λ (1 116 MeV) and Σ^0 (1 193 MeV). Also visible are peaks at the masses of $\Sigma(1385)$, $\Lambda(1405)$ and $\Lambda(1520)$. Analysis of simulated data demonstrated that $K^+\Lambda$ events leave less

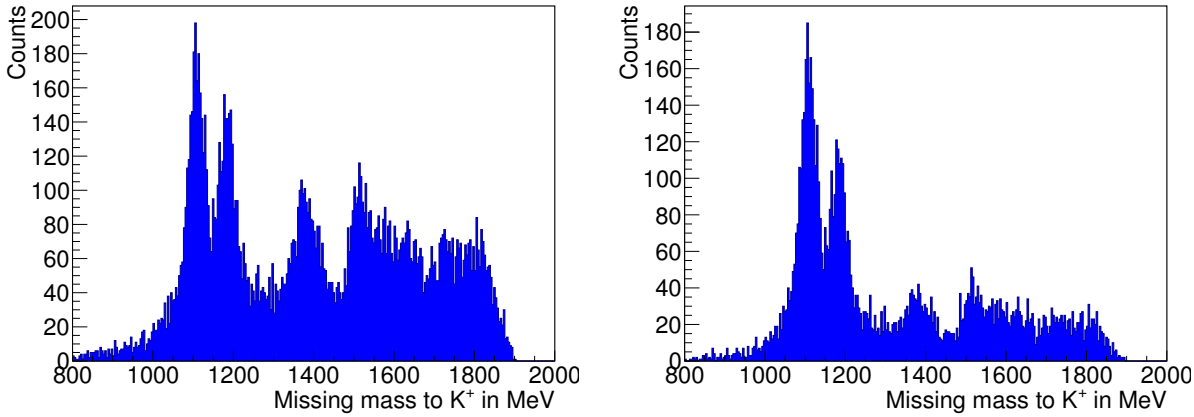

(a) (b)

Figure 5.4: Mass missing to the K^+ candidate in the forward spectrometer. All events in (a) and events where there was less than 250 MeV deposited energy in the BGO-ball in (b).

than 250 MeV in the BGO-ball. Therefore to suppress the number of events from these higher hyperon states, a cut on the maximum energy deposited in the BGO-ball of 250 MeV was applied. As one can see in figure 5.4b, the cut removes mainly events corresponding to the higher hyperon states, and the peaks of Λ and Σ^0 stay the same.

5.2 $K^+\Lambda$ Identification

To further reduce background from misidentified channels, the π^0 from the decay $\Lambda \to n\pi^0$ (branching ratio 35.8 % [Oli+14]) was identified in the BGO-ball. The π^0 decays into two photons. To identify it, the invariant mass of all combinations of two neutral central tracks is built according to equation 5.4:

$$m_{\pi^0} = \sqrt{(E_1 + E_2)^2 - (\vec{p_1} + \vec{p_2})^2}, \tag{5.4}$$

where $\vec{p_{1/2}}$ are the three momenta and $E_{1/2}$ the energies of each photon. Due to the branching ratio of the decay of 35.8 % the statistics are reduced, but due to the lower background the systematic uncertainties are much better under control. In a future analysis this requirement may be released to increase the

statistics by more than a factor of 2.

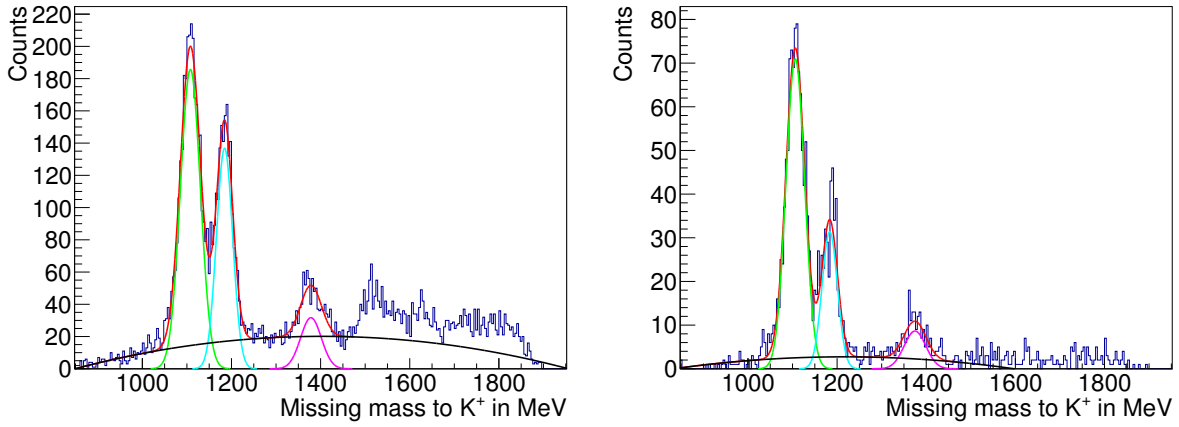

(a) (b)

Figure 5.5: Missing mass to the K^+ candidate in the forward spectrometer, with a momentum of 450 MeV to 1 000 MeV, and the beam photon. Plotted for the cases with (a) and without (b) the requirement of the π^0 in the BGO-ball. The peaks of Λ (green), Σ^0 (cyan) and $\Lambda(1405)$ and $\Sigma(1385)$ (magenta) are fitted with a Gaussian each and the background (black) below the peaks is fitted by a polynomial of second order.

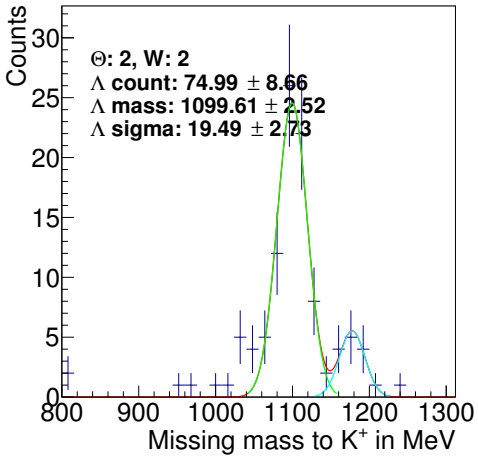

Figure 5.6: Missing mass from the K^+ to beam photon for $\Theta^{c.m.}_{K^+} = 3°$ to $6°$ and $W = 1\,700$ MeV to $1\,800$ MeV. Fitted are two Gaussian functions (red), where the individual Gaussians are shown in green (Λ) and cyan (Σ^0).

In figure 5.5, the missing mass to the K^+ candidate in the forward spectrometer is plotted with and without requiring a π^0 in the BGO-ball. The relative height of the background, which is approximately fitted by the black curve, is reduced significantly. The peaks of Λ and Σ^0 can not completely be separated by simply cutting between both peaks. To extract the number of $K^+\Lambda$ events, the Λ and Σ^0 peak are fitted with Gaussian functions and the number of $K^+\Lambda$ events is extracted from the integral of the corresponding Gaussian function, divided by the bin width. This extraction is performed in 3° $\Theta^{c.m.}_{K^+}$ and 100 MeV center of mass energy bins, $W = \sqrt{s}$. [2] In figure 5.6, one example $\Theta^{c.m.}_{K^+}$, W bin is shown, fitted with two Gaussian functions. For the first two W bins, 1 600 MeV to 1 700 MeV and 1 700 MeV to

[2] The Mandelstam s, see equation 1.1

1 800 MeV this works very well. For the higher W bin from 1 800 MeV to 1 900 MeV, the resolution is worse and both peaks can not be distinguished clearly. Even higher W are not considered in this work, as the statistics in these bins is not sufficient for this analysis.

5.2.1 $\pi^+\pi^0 n$ Contamination

To better distinguish both peaks the identification of the final state is further improved. In section 5.1 the contamination of selected K^+ candidates by misidentified π^+ in the forward spectrometer was mentioned. After requiring the detection of the π^0 from the decay of the Λ, it is possible to further constrain the reaction identification, by looking at the missing mass to the K^+ and π^0 combined system. In the case of a $K^+\Lambda \to K^+\pi^0 n$ event, the missing mass of the K^+ candidate and the π^0 should be the mass of the neutron.

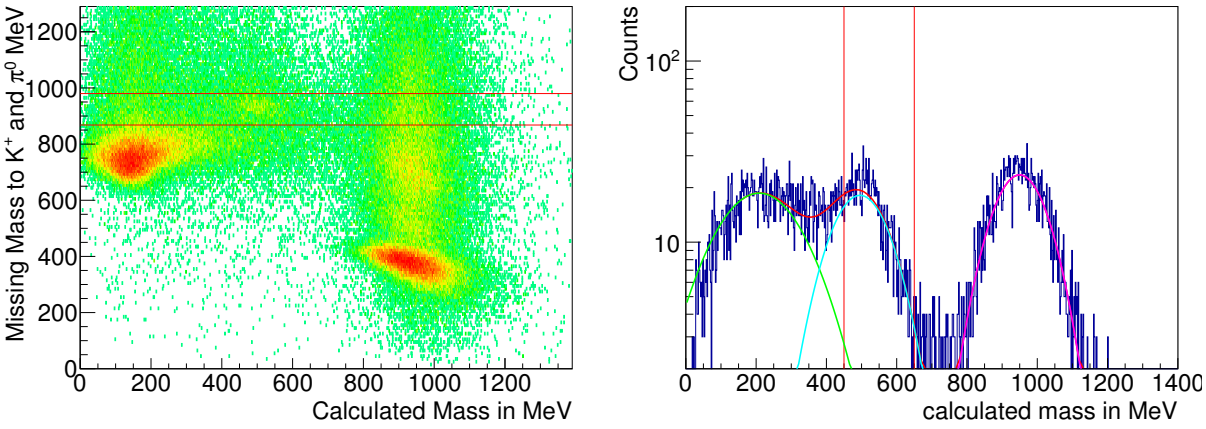

(a) (b) p = 700 MeV to 1 500 MeV

Figure 5.7: Cut on the missing mass to the $K^+\pi^0$ system. In (a) the missing mass to the $K^+\pi^0$ system is plotted against the mass of the particle detected in forward spectrometer, calculated from β and momentum. The red lines indicate the applied cut. In (b) the calculated mass of the particles detected in the forward spectrometer is plotted in the same momentum range as in figure 5.2b.

In figure 5.7 the missing mass to the $K^+\pi^0$ system is plotted against the mass of the particle detected in the forward spectrometer, calculated from its β and momentum. Three peaks are visible in figure 5.7a, corresponding to the π^+, K^+ and proton. Only the K^+ peak is located at missing mass corresponding to the neutron mass, both other peaks are having lower missing masses. Therefore a 1 σ cut is applied around the neutron mass.

When comparing the spectrum of calculated masses (figure 5.7b) of particles in the forward spectrometer after this cut, with the previous figure 5.2b of the same momentum range, a peak at the mass of the K^+ is now clearly visible. Still a certain amount of π^+ might be misidentified as K^+. By fitting the peaks of π^+, K^+ and proton with Gaussian functions and calculating the fraction of π^+ below the K^+ peak within the chosen cuts, one gets a contamination of 7.8 %. Therefore the cut on the K^+ mass is shifted slightly to higher calculated masses of 450 MeV to 650 MeV to remove this contamination. An overview of all $\Theta^{c.m.}_{K^+}$ and W bins after applying this addition cut is shown in appendix E.

5.3 Cross Section

The cross section of a reaction is a measure of the probability that this reaction will happen per incident particle and reaction center, as indicated in equation 5.5:

$$\sigma = \frac{N_{reactions}}{N_{photons}} \frac{1}{\rho_A}, \tag{5.5}$$

where $N_{reactions}$ represents the number of reactions, $N_{photons}$ the number of incoming photons, and ρ_A the area density of the target. Not all reactions are detected, due to geometrical constraints or cuts in the analysis which cut away background but also some part of the signal. This is taken into account by the reconstruction efficiency, ϵ. In addition, the cross section will not be independent of W or Θ, therefore the cross section is measured differentially in both variables.

The differential cross section of the reaction $\gamma p \rightarrow K^+\Lambda$, as a function of $\Theta^{c.m.}_{K^+}$ and W, in this work, is calculated according to equation 5.6:

$$\frac{d\sigma}{d\Omega}_{K^+\Lambda}(\Theta^{c.m.}_{K^+}, W) = \frac{N_{K^+\Lambda}(\Theta^{c.m.}_{K^+}, W)}{\epsilon_{K^+\Lambda}(\Theta^{c.m.}_{K^+}, W) N_{photons}(W) \rho_A \Omega(\Theta^{c.m.}_{K^+})}, \tag{5.6}$$

where $N_{K^+\Lambda}(\Theta^{c.m.}_{K^+}, W)$ corresponds to the number of reconstructed reactions per Θ and W bin, $\epsilon_{K^+\Lambda}(\Theta^{c.m.}_{K^+}, W)$ corresponds to the reconstruction efficiency for this reaction per Θ and W bin, $N_{photons}(W)$ corresponds to the number of incident photons that could have produced the reaction per W bin, ρ_A is the area density of the liquid hydrogen target, and $\Omega(\Theta^{c.m.}_{K^+})$ is the solid angle, which in this case is given by the integral $\Omega = \int_0^{2\pi} d\phi \int_{\Theta_1}^{\Theta_2} \sin\Theta d\Theta = 2\pi[\cos\Theta]_{\Theta_1}^{\Theta_2}$. The following sections describe how these parameters are determined.

5.3.1 Target Area Density

The target area density, ρ_A, for the $l = (6.0 \pm 0.1)$ cm liquid hydrogen target is given by equation 5.7:

$$\rho_A = \frac{l\rho N_A}{A} = (2.538 \pm 0.042) \times 10^{23}\,\text{cm}^{-2} = (2.538 \pm 0.042) \times 10^{-7}\,\mu\text{b}^{-1}, \tag{5.7}$$

where ρ is the density of liquid hydrogen, N_A the Avogadro constant and A the molar mass of hydrogen.

5.3.2 Incident Photon Flux

The number of incident photons, $N_{photons}$, is determined using the photon flux monitor (see section 3.2.1). With P_γ described in section 3.2.1, and the number of photons tagged by the tagging detector, the photon flux can be determined for each W bin of the analysis. Determining the effective P_γ for the beam time used in this analysis is part of the ongoing master thesis of Katrin Kohl [Koh16], an energy independent effective P_γ of 10 %, which fits to the current state of Katrin Kohls analysis, is used. This value is lower than one would usually expect and was caused by a misaligned photon collimator. The value of 10 % is determined in different analysis and is assumed to be correct within a relative error of 10 %. Figure 5.8 shows $N_{photons}$ for each individual W bin, for the complete data set used in this analysis.

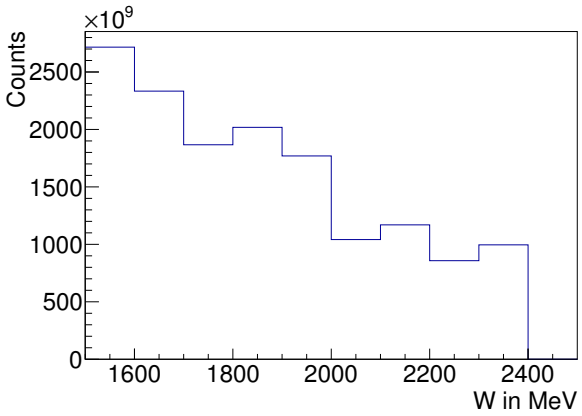

Figure 5.8: Number of photons incident on the target per W bin, for the whole analyzed data set. The step around $W = 2\,000\,\text{MeV}$ corresponds the the coherent enhancement from the production of linearly polarized photon beams.

5.3.3 Reconstruction Efficiency

The simulation of the BGO-OD experiment tries to perfectly model the behavior of all detectors of the experiment. Therefore the simulated individual energy deposits are converted to the same format of ADC and TDC information, that is produced by the real experiment. In this step the energy depositions and times are smeared out according to the resolution of the detector. Also the detector efficiency is considered and hits are discarded accordingly.

The detection efficiency is determined using simulated $\gamma p \to K^+\Lambda$ events. By dividing the number of reconstructed events in each $\Theta^{c.m.}_{K^+}$ and W bin by the number of generated events in this bin, the reconstruction efficiency is determined. The determined reconstruction efficiency varies between 2 % to 9 %. Without requiring the π^0 from the $\Lambda \to \pi^0 n$ decay, a reconstruction efficiency of 3 % to 30 % is achieved. The values determined for each $\Theta^{c.m.}_{K^+}$ bin, averaged over W, are shown in figure 5.9.

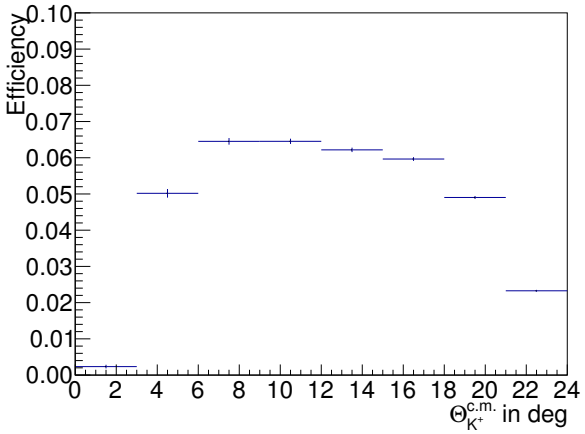

Figure 5.9: Reconstruction efficiency in dependency of $\Theta^{c.m.}_{K^+}$, averaged over all W bins.

Driftchamber efficiency

The efficiency of the drifchambers, MOMO and SciFi2 needed to be determined in the real data to ensure that the same efficiencies were used for simulated data. MOMO and SciFi2 efficiencies were determined to be 80 % and 97.5 % respectively [Jud16]. Part of this thesis work was to determine the driftchamber efficiencies.

The method used to determine the efficiency is described below: if a track passed through the driftchambers, it is checked for each driftchamber layer if it has seen a particle or not. To determine if a track has passed through the driftchambers, the reactions $\gamma p \rightarrow p\pi^0/\eta \rightarrow p\gamma\gamma$ were investigated. Track candidates are found by reconstructing a π^0 or η from the invariant mass of two γ in the BGO-ball and checking if the missing mass to this meson goes in the direction of the forward spectrometer. For these track candidates, it was checked if corresponding clusters in the MOMO, SciFi2 and TOF detectors were found. If such clusters were found, the particle must have crossed the driftchambers and therefore this track was used for the efficiency determination. The same analysis was performed on simulated $\gamma p \rightarrow p\eta$ events to check for losses of efficiency stemming from the reconstruction algorithms or geometrical acceptance. The resulting efficiencies are calculated per driftchamber layer and fitted in dependence of β and Θ_p^{lab} by a two dimensional exponential function for each chamber. The resulting efficiencies are then used as efficiencies of each individual driftchamber layer in simulation. The results for real and simulated data after including the efficiency functions are shown in figure 5.10.

Due to not yet understood effects, the efficiency for simulated data still does not completely describe the behavior of the driftchamber efficiency in real data, but the deviation after including the efficiency in simulation is smaller. The deviation increases for increasing β and Θ_p^{lab} and is less than 18 % absolute efficiency. As for a driftchamber cluster only a hit in one of the layer is required, the effect on the total reconstruction efficiency is even smaller. The difference in the number of reconstructed forward tracks in simulated data with and without efficiency included, is just 1 %, for low W, and 5 %, for the highest W, smaller, when including the calculated efficiency function.

5.3.4 Systematic Uncertainties

During the determination of the differential cross section, beside the statistical uncertainty, several systematic uncertainties need to be considered. In the following they are summarized.

- The method of determining the number of reconstructed $K^+\Lambda$ events, $N_{K^+\Lambda}$, by fitting the peaks in the spectrum of the mass missing to the K^+, gives an uncertainty due to the uncertainties of the fit parameters. This uncertainty is determined for each bin individually and is in the order of 10 % to 20 % relative.

- The photon flux is not yet finally determined, a fixed value of 10 % is assumed. The uncertainty on this value is assumed to be 10 % relative.

- The size of the target cell is assumed to be precise within 1 mm, this results on an relative uncertainty of the target area density, ρ_A, of 1.7 %.

- In addition also the uncertainty from the not perfectly described efficiency of the driftchambers need to be considered. As mentioned in section 5.3.3, the efficiency per driftchamber layer is up to 18 % lower in simulated then in real data. Due to the redundancies in the driftchamber setup the number of reconstructed tracks, only deviates by 1 % to 5 %. Therefore 1 % to 5 %, depending on W, is considered as the uncertainty.

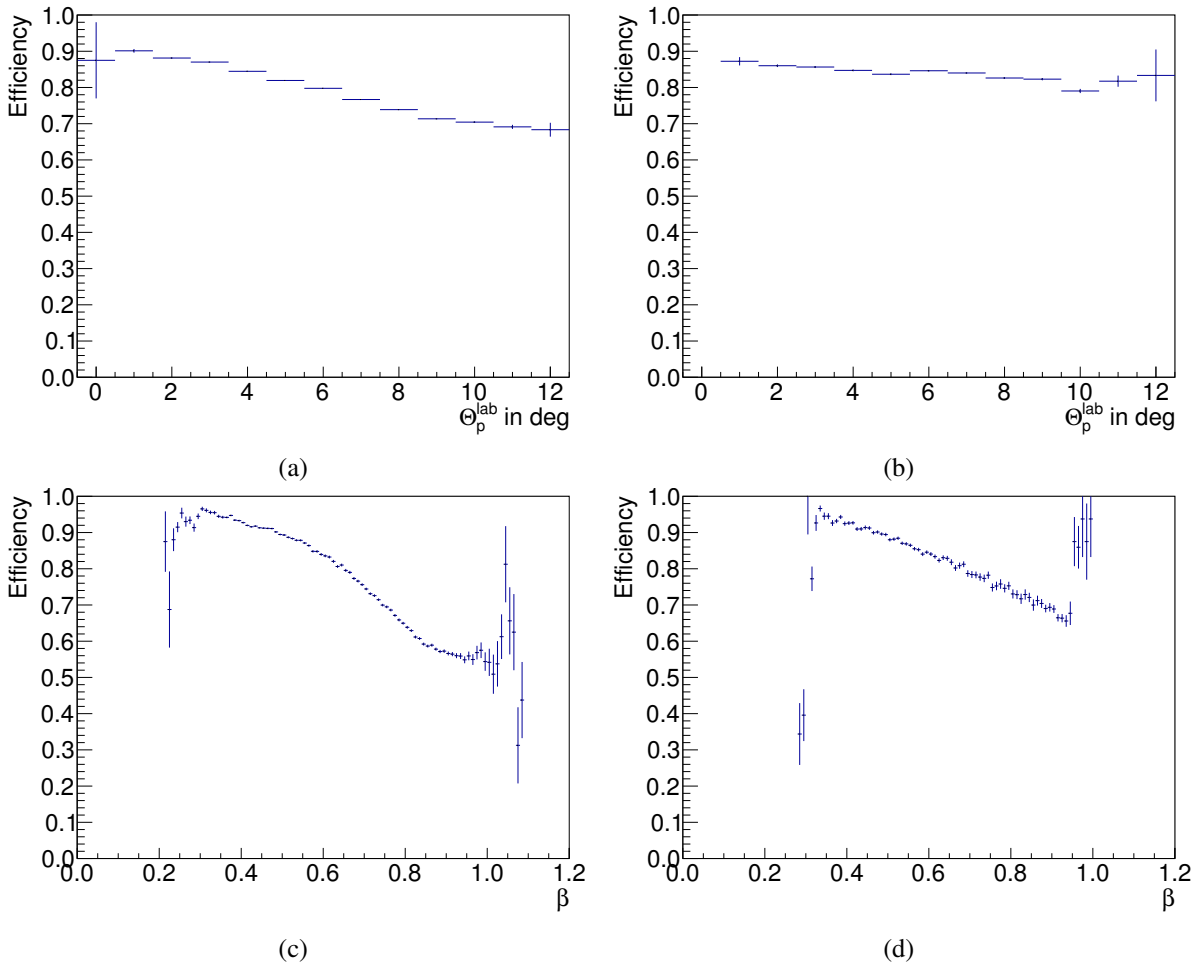

Figure 5.10: Driftchamber efficiency per layer, averaged over all chambers, in dependence of Θ_p^{lab} in real (a) and simulated data (b), and in dependence of β in real (c) and simulated data (d).

The individual contributions to the systematic uncertainty are summed up linearly, and are graphically presented together with the final cross sections in the final section 5.3.6.

5.3.5 $K^+\Sigma^0$ Contamination

For the final determination of the cross section, it is important that the reconstructed event sample is not contaminated by reaction from other reaction channels. The peaks in the spectrum of the missing mass to the K^+, corresponding to Λ and Σ^0, overlap. To study the influence of this overlap, both peaks need to be distinguished, in particular for higher momenta of the K^+. As the mass resolution of the forward spectrometer is better for low momentum particles, it is expected that both peaks get broader with higher momentum of the K^+, which can also be seen in simulated data (see figure 5.11). As the Σ^0 decays with a branching ratio of 100 % to $\gamma\Lambda$ [Oli+14], it is possible to distinguish both channels by identifying this decay-γ in the BGO-ball. In the rest frame of the Σ^0, the energy of this γ is equal to the mass difference between Σ^0 and Λ:

$$E_{decay-\gamma} = M_{\Sigma^0} - M_\Lambda = 77\,\text{MeV}. \tag{5.8}$$

All neutral particles detected in the BGO-ball are considered as Σ^0 decay-γ-candidates and are boosted

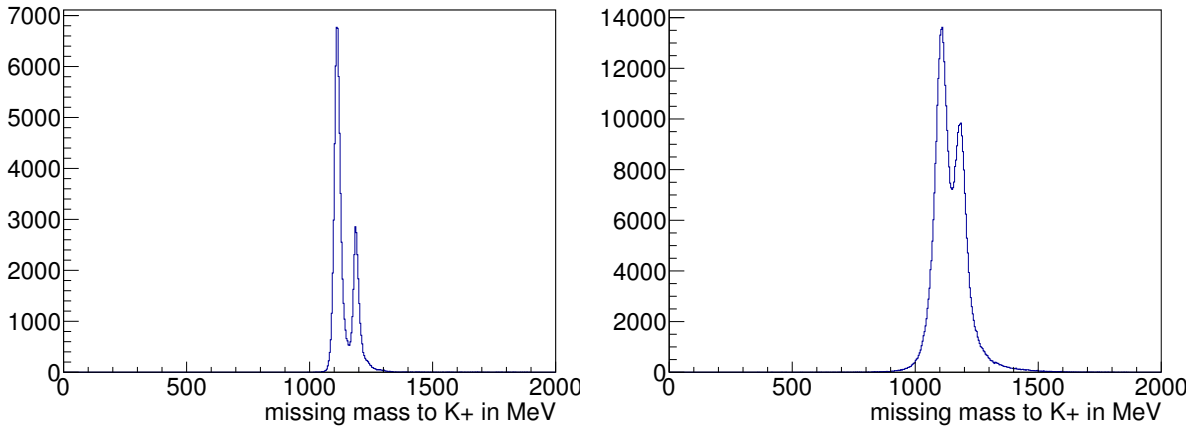

(a) p = 360 MeV to 700 MeV (b) p = 700 MeV to 1 500 MeV

Figure 5.11: In simulated data: Mass missing to the K^+ candidate in the forward spectrometer, for two different momentum ranges, 360 MeV to 700 MeV in (a) and p = 700 MeV to 1 500 MeV in (b). The mass resolution decreases with higher K^+ momentum.

into the rest frame of the Σ^0, using the missing four-momentum from the K^+ to the initial state. When plotting the energy of these particles in the Σ^0 rest frame against the mass missing from the K^++decay-γ system a clear peak at the expected energy of 77 MeV shows up, as shown in figure 5.12a. Below the peak a broad structure is visible. This band contains photons and neutrons from the decay of the π^0 from the decay of Λ. As these photons are missing to the Λ mass, they are showing up as diagonal band below the peak corresponding to the Σ^0 decay-γ, as can also be seen in simulations (figure 5.12d).

All events with a decay-γ candidate within $2\,\sigma$ around the peak, indicated by the red lines in figure 5.12a, are considered $K^+\Sigma^0$ events. These events can then be subtracted from all events.

Some decay-γ are not detected. The efficiency of detecting the decay-γ can be determined using simulated data. When simulating $K^+\Sigma^0$ events, this efficiency can be determined by counting the number of decay-γ that were detected, and dividing this by the number of identified K^+. This efficiency is determined in bins of $\Theta^{c.m.}_{K^+}$ and W.

In figure 5.13 the average detection efficiency for this decay-γ is shown in dependence of the center of mass energy W. In general, the detection efficiency is around 70 % and only a small dependence on W and nearly no dependence on $\Theta^{c.m.}_{K^+}$ is visible. The distribution was fitted with a second order polynomial function. This polynomial function is then averaged over the W range of the actual bin.

With the averaged value from the fit function, the distribution of identified Σ^0 can be scaled to match the integral of the $K^+\Sigma^0$ events not identified (see figure 5.14a). These scaled events are subtracted from the $K^+\Lambda$ candidate events, to completely remove the $K^+\Sigma^0$ yield (figure 5.14b). The identification of the $K^+\Sigma^0$ events was not background free, therefore also around 17.5 % of $K^+\Lambda$ events were also subtracted. This is taken into account, when calculating the reconstruction efficiency, as the same procedure was applied to simulated data.

The yield of $K^+\Lambda$ events, after applying this method is shown in 5.15, in comparison to the available data from CLAS [McC+10] and SAPHIR [Gla+04], as well as the result of the BG2014-02 Bonn-Gatchina PWA analysis [Sar+14; Gut+14]. When comparing this yield with the uncorrected one (shown in gray), one can see that the data in all bins stays unchanged within statistical errors. Therefore a contamination of reconstructed Λ with Σ^0 id considered to have no influence on the cross section within the statistical errors.

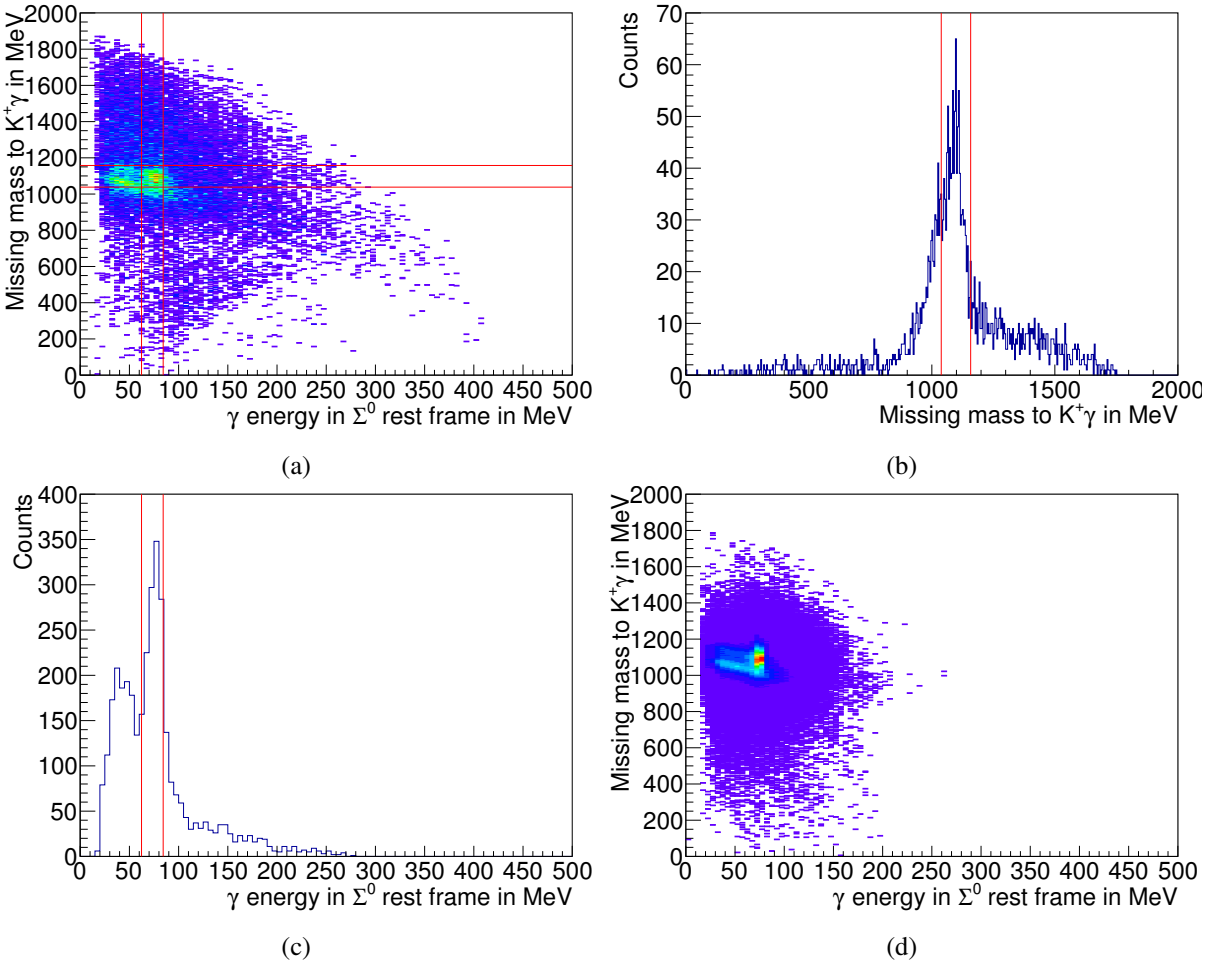

Figure 5.12: Identification of the Σ^0 decay-γ. The energy of the Σ^0 decay-γ candidate in the hyperon rest frame should correspond to the mass difference of Σ^0 and Λ of 77 MeV. Where the mass missing from this γ and the K^+ to the beam photon should correspond to the Λ mass. In (a) both quantities are plotted against each other. A clear peak can be seen in the missing mass, shown in (b), and the decay-γ energy, shown in (c). The band below the decay-γ peak corresponds to photons from the π^0 of the decay $\Lambda \to n\pi^0$, and is also seen in simulations, shown in (d). The red lines indicate the ranges to select the Σ^0 decay-γ.

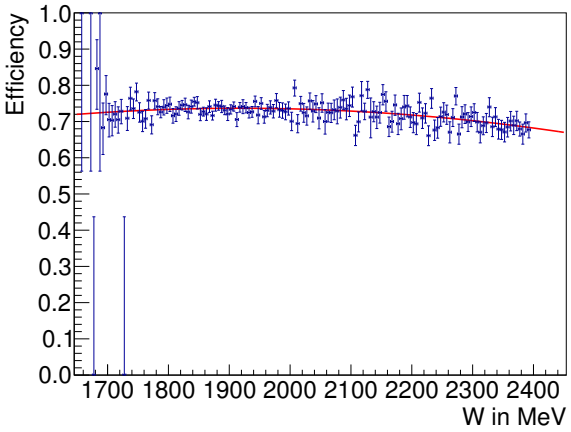

Figure 5.13: Σ^0 decay-γ identification efficiency against the center of mass energy W.

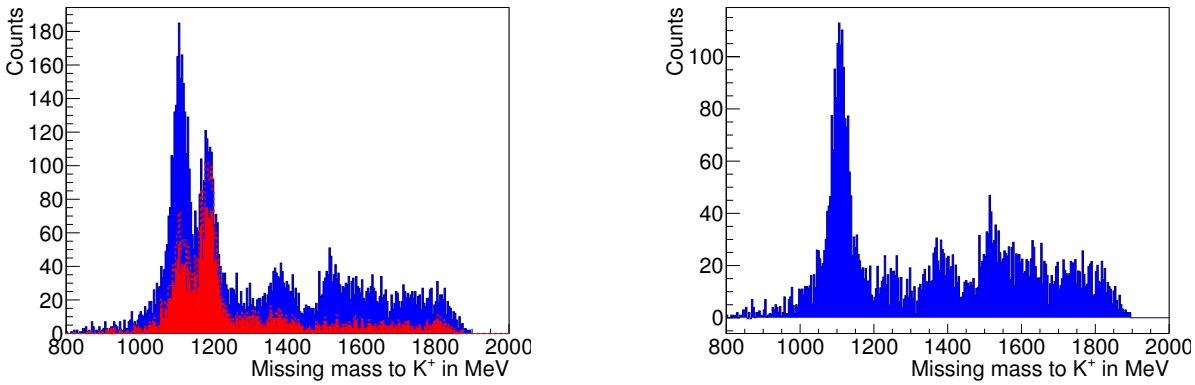

(a) (b)

Figure 5.14: Subtraction of Σ^0 events. In (a) all events are shown in blue, in red those events are shown, where a Σ^0 decay-γ was identified. The dotted red curve, shows these events scaled by the Σ^0 decay-γ detection efficiency. When subtracting them from all events, one gets the distribution in (b), where the Σ^0 is removed.

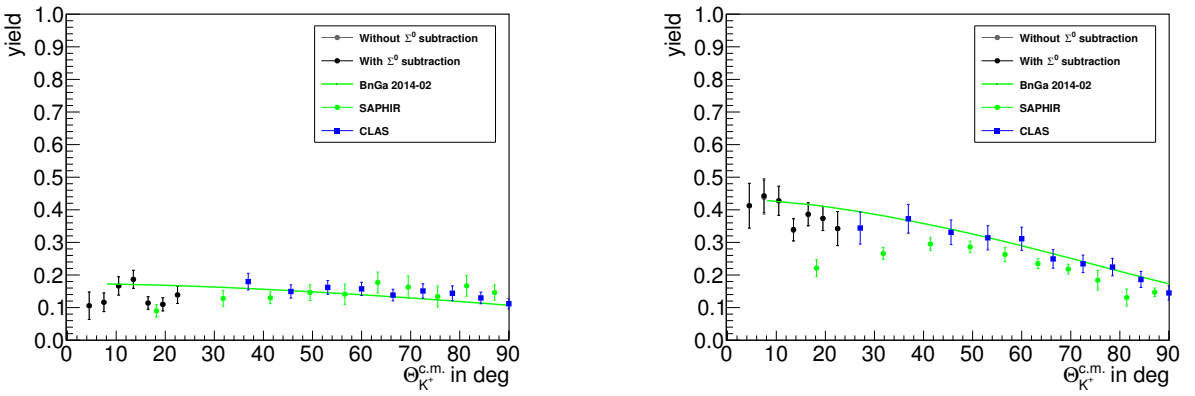

(a) $W = 1.6\,\text{GeV}$ to $1.7\,\text{GeV}$ (b) $W = 1.7\,\text{GeV}$ to $1.8\,\text{GeV}$

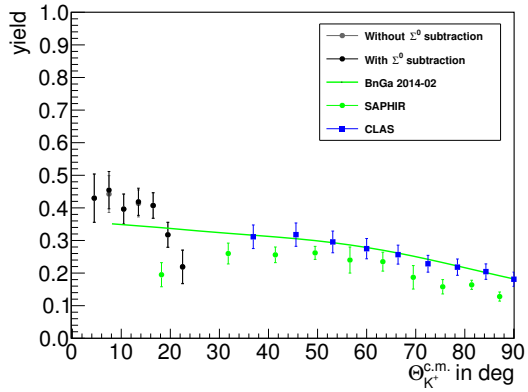

(c) $W = 1.8\,\text{GeV}$ to $1.9\,\text{GeV}$

Figure 5.15: $\gamma p \to K^+\Lambda$ yield after subtracting $K^+\Sigma^0$ events. Black dots represent this work after removing the $K^+\Sigma^0$ contribution, gray dots represent this work before removing the $K^+\Sigma^0$ contribution, which overlap in most bins, green dots present data from the SAPHIR collaboration [Gla+04] and blue squares present data from the CLAS collaboration [McC+10]. The green line presents the result of the Bonn-Gatchina PWA analysis [Sar+14].

5.3.6 $\gamma p \to K^+\Lambda$ Cross Section

The differential cross section, calculated from equation 5.6, is shown in figure 5.16. From these preliminary results it seems that the data from this work seems to agree with the prediction of the Bonn Gatchina PWA analysis. The systematic uncertainties are dominated by the still preliminary photon flux and the discrepancies in the driftchamber efficiencies between simulated and real data. Both uncertainties together make up half of the total systematic uncertainties and can hopefully be reduced soon.

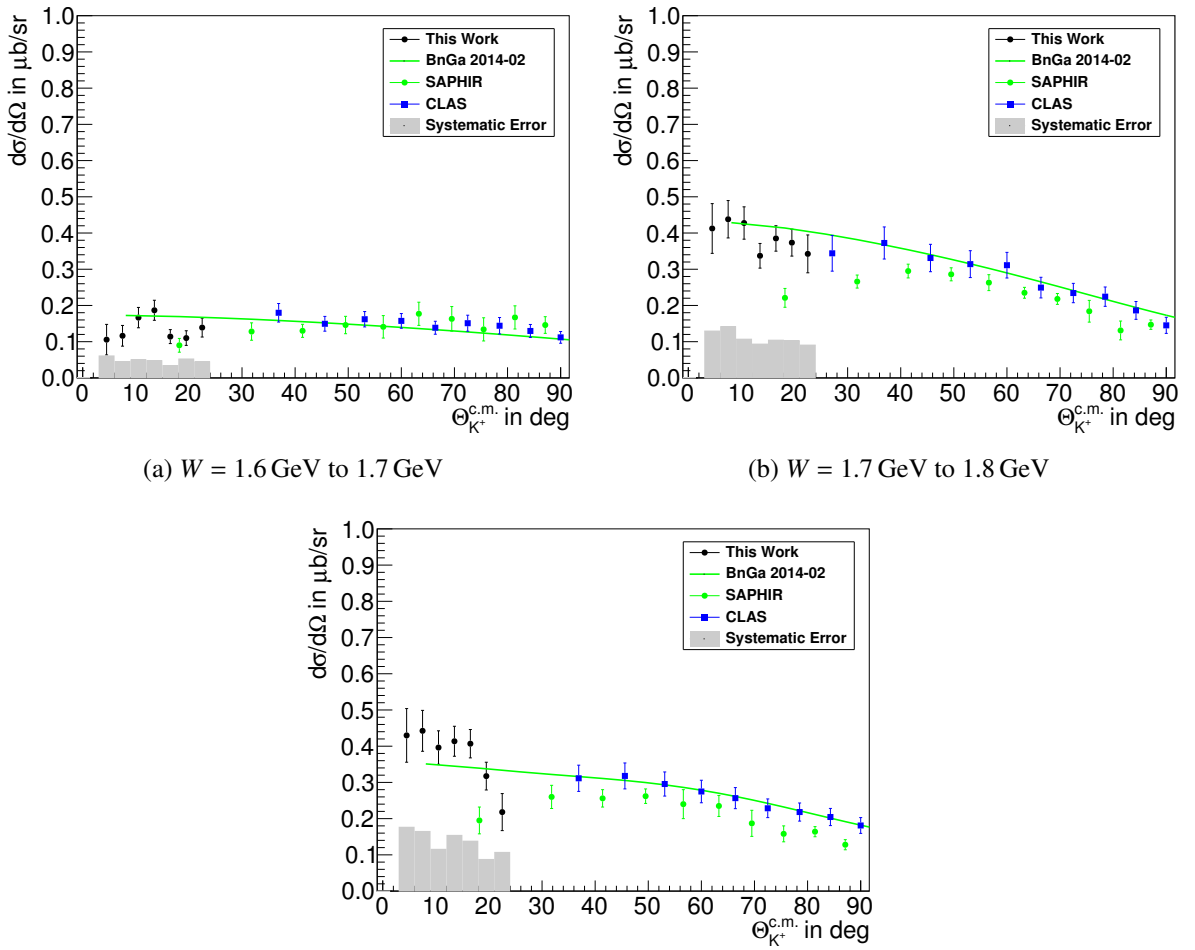

(a) $W = 1.6\,\text{GeV}$ to $1.7\,\text{GeV}$

(b) $W = 1.7\,\text{GeV}$ to $1.8\,\text{GeV}$

(c) $W = 1.8\,\text{GeV}$ to $1.9\,\text{GeV}$

Figure 5.16: $\gamma p \to K^+\Lambda$ cross section. Previous data and fits are the same as in figure 5.15.

In figure 5.17 the results of the $\Theta^{c.m.}_{K^+}$ bin from 3° to 6° of this thesis were added to figure 2.3. Unfortunately from these points it is not yet possible to make a strong argument for or against one of the models. Within $2\,\sigma$ of the statistical error the points fit to all models. Therefore the statistical error should be reduced in the future. Another beam time with 340 h of beam time is available for analysis, and due to no special requirements for the trigger condition, all future beam times will also contribute. Furthermore by improving the analysis to reconstruct both decay channel of the Λ, the statistics can again be improved by a factor of 2 to 3.

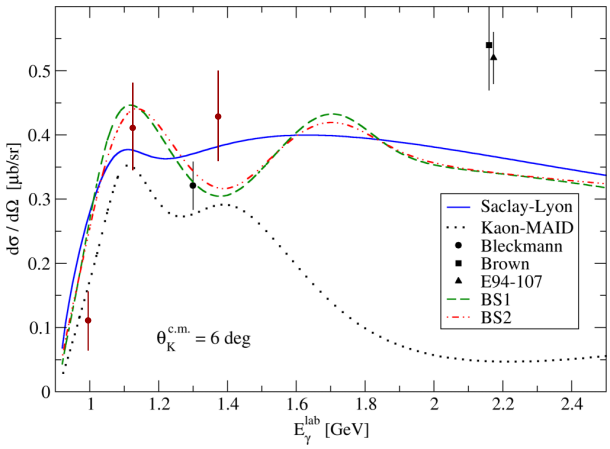

Figure 5.17: Data from this work (dark red points) added to figure 2.3.

CHAPTER 6

Summary and Conclusions

The BGO-OD experiment at the electron accelerator ELSA investigates meson photoproduction, with a real, tagged photon beam, produced via bremsstrahlung. It is particularly suited to associated strangeness photo production. With the combination of central electromagnetic calorimeter and a magnetic forward spectrometer, it is ideally suited for the investigation of reactions with low transverse momentum, where the associated high momentum particle will go in the forward spectrometer.

To be able to measure all complex amplitudes of a reaction, polarization degrees of freedom are essential. Therefore a Møller polarimeter was built for the BGO-OD experiment, which measures the degree of longitudinal polarization of the electron beam, which is converted to a circular polarized photon beam via bremsstrahlung. A simultaneous measurement with the polarimeter of the neighboring Crystal Barrel experiment showed a good agreement with the measured degree of polarization. Furthermore, the Møller polarimeter correctly determined the degree of polarization of the expected longitudinal polarization component, while rotating the electron spin at the electron source of the accelerator. The degree of electron beam polarization was determined to a statistical accuracy of 2 % relative with a measuring time of 1 h and a relative systematic accuracy of 1 %.

Circularly polarized photon beams allow the measurement of polarization observables. $\gamma p \to K^+\Lambda$ is one of the most measured photoproduction channels. Due to the self analyzing hyperon decay this channel is close to the complete experiment. Still missing is the full angular coverage. The coverage of the forward angular region is especially needed to understand the dominant t-channel contribution in this channel. In this thesis the K^+ was successfully reconstructed in the angular range of the forward spectrometer, which covers the yet uncovered extreme forward angles. The $K^+\Lambda$ and $K^+\Sigma^0$ reactions could be successfully distinguished, and differential cross sections were determined. The achieved statistical and systematic uncertainty are 10 % and 30 % respectively. Within these uncertainties the cross section fits to the prediction from the Bonn Gatchina PWA analysis.

To further improve the systematic uncertainties of the measured cross section, the analysis can be improved. Implementing the correct driftchamber efficiency in the simulation, will reduces the systematic uncertainties by 1 % to 5 %. Further, the finally determined photon flux will have an uncertainty smaller than 10 %, so when including this, the systematic uncertainty will be reduced too. Just these two optimizations will improve the systematic uncertainty by a factor of two. Furthermore the individual systematic uncertainties were added up linearly. As they are mostly independent of each other it might also be allowed to sum them up quadratically, which would also result in a much lower uncertainty of 15 % to 23 %. In addition 340 h of additional data are available for analysis. Also the requirement to detect the π^0 can be dropped, when improving the analysis further, which will significantly improve the statistical error significantly.

The Møller polarimeter built and the analysis performed in this thesis provide the basis for future analysis of different observables in different reaction channels at the BGO-OD experiment. With the Møller polarimeter the polarization observables C_x and C_z get accessible, which can be measured in

the hyperon channels due to the self analyzing weak hyperon decay, without requiring an addition recoil polarimeter. To perform these measurements with circularly polarized photon beams, additional focusing magnets need to be installed in the extraction beamline.

APPENDIX **A**

Units and Coordinate System

Natural units are used in this thesis. In natural units energy is measured in units of eV, where 1 eV corresponds to the kinetic energy one electron gains when it is accelerated by a potential difference of 1 V and is equal to 1.6022×10^{-19} J. In these units the Planck constant, $\hbar$ and the speed of light, c are equal to 1. $\hbar$ and c are omitted in most formulas given in the thesis, so that mass and momentum are also given in units of eV.

The coordinate systems used in this thesis are right handed. If not stated differently the z-axis is defined along the photon beam. Therefore when looking in beam direction the x-axis points right, and the y-axis points upwards.

A.1 Masses of particles discussed in this thesis

Electron: $m_e = 0.511\,\text{MeV}$
Proton: $m_p = 938.3\,\text{MeV}$
π^0: $m_{\pi^0} = 135.0\,\text{MeV}$
K^+: $m_{K^+} = 493.7\,\text{MeV}$
Λ: $m_\Lambda = 1\,115.7\,\text{MeV}$
Σ^0: $m_{\Sigma^0} = 1\,189.4\,\text{MeV}$

APPENDIX B

Goniometer Tank

The previously installed vacuum chamber for the goniometer system (goniometer tank), was just large enough to contain the goniometer. When installing the Møller target on the goniometer system, the goniometer system did no longer fit into the existing goniometer tank. Therefore a new goniometer tank was required. This tank had to fit in the same space in z direction, therefore it was not possible to just scale the size of the old goniometer tank, but a completely new design was needed. Using the design used at the Crystal-Barrel experiment was also not suitable as it is also much larger than the available space.

When designing the new tank some new features were added to the goniometer tank. The homing procedure of the goniometer system results in different home positions depending on the temperature of the system. Therefore a way to check and correct the absolute position of the system was wished. To provide this possibility a reference camera and a reference mark were added to the tank. When moving the goniometer system all to the right, the "empty radiator" position and the reference mark can be seen simultaneously with a huge magnification. In this position the gonimeter can be moved to the correct position and the system can than be said that it is in the correct position. A second point was the camera that showed the radiator. In the old goniometer tank, this camera always showed some spot on the radiator plate, but it would be nice to be able to see the radiator directly. Therefore a camera was mounted such that the radiator is directly visible with this camera. Because one never knows what future improvements are needed, several spare parts were added to the tank:

- Two crane eyes are added to be able to move the tank for maintainance.
- A crane eye is also added to the two end plates closing the tube, so that it is not needed to hold the weight of the end plates when opening the tank.
- Four rails with screw holes are added in the front, back, top and bottom of the tank.
- Two KF25 flanges were added at the bottom of the tank, to be able to provide water cooling to the goniometer system if needed.
- Several blind flanges were added to be prepared for anything else.

As design for the tank a tube shape was chosen, with a diameter as large that it just fits the available space. Because in this size the radiator is not in the center of the tank, the beam pipe enters the tank eccentrically. The CAD design was made with Autodesk Inventor 2010 and the mechanical drawings are attached in section B.1.

To check prior to the production of the tank, that it would stand the air pressure, when the tank is evacuated, a finite elements simulation was performed with the tools included in Autodesk Inventor. The result of this simulation is attached in section B.2.

B.1 Schematic Drawings

The goniometer tank was manufactured according to these drawings. Unfortunately one error was present in the design: the sealing faces in the end plates were too deep, therefore the whole end plates of the final tank was dressed to size. A second point were the feet for the goniometer system. Welding such small things with the precision needed, turned out to be not possible. It would have been better to use one massive foot to mount the goniometer system on.

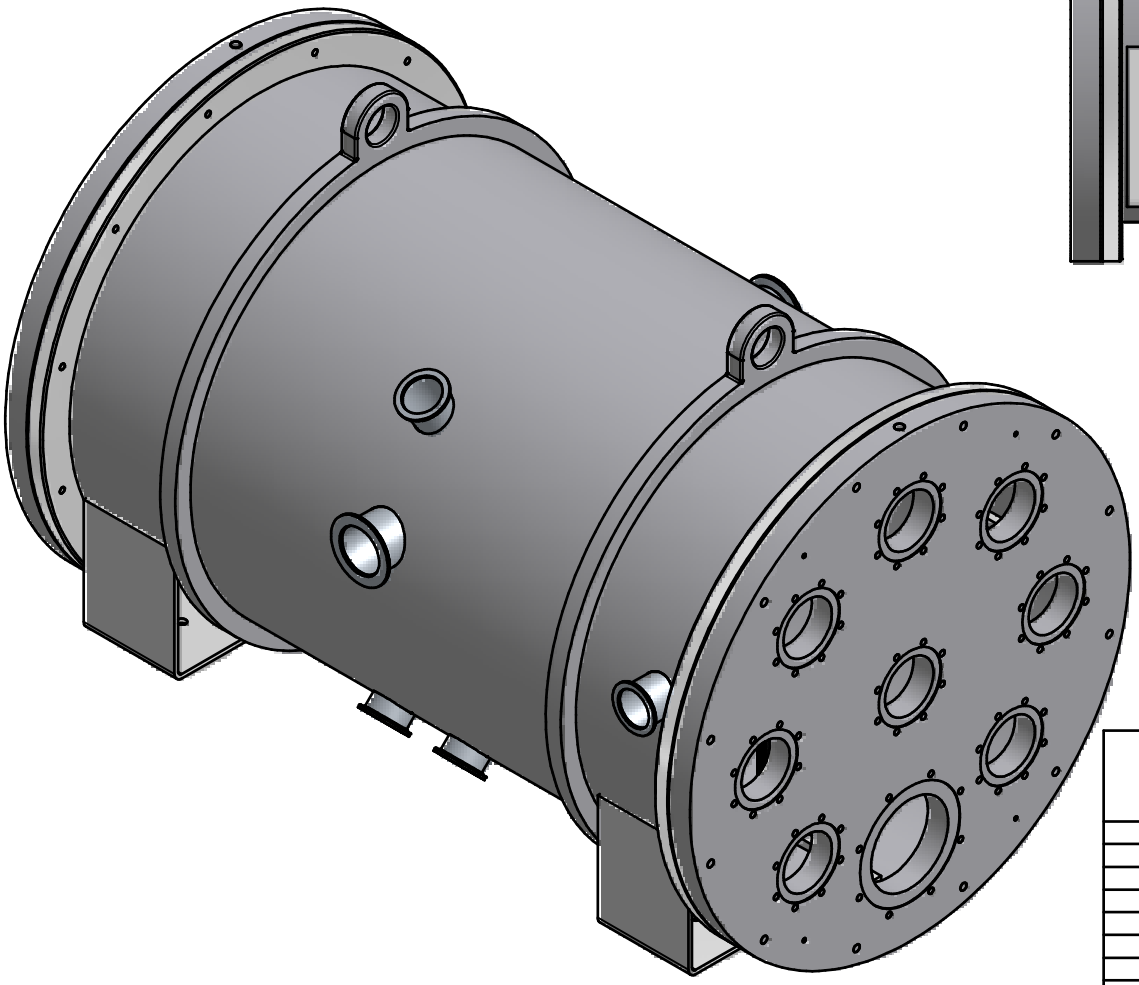

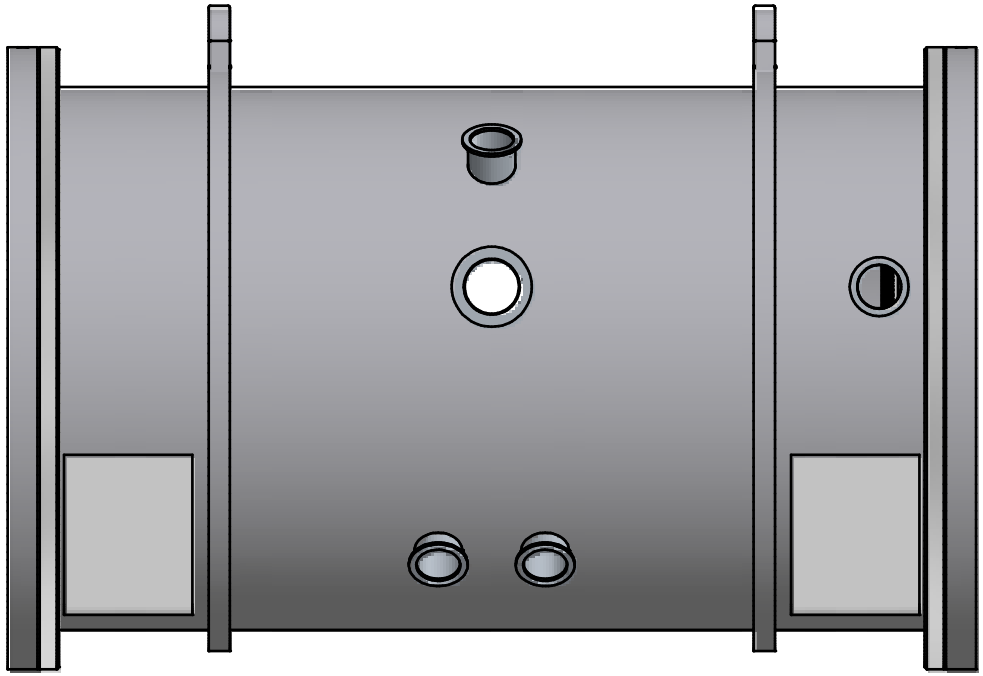

					Datum	Name
				Gezeichnet	07.07.2014	zimmermann
				Kontrolliert		
				Norm		
Status	Änderungen	Datum	Name			

Goni4-2

1

A3

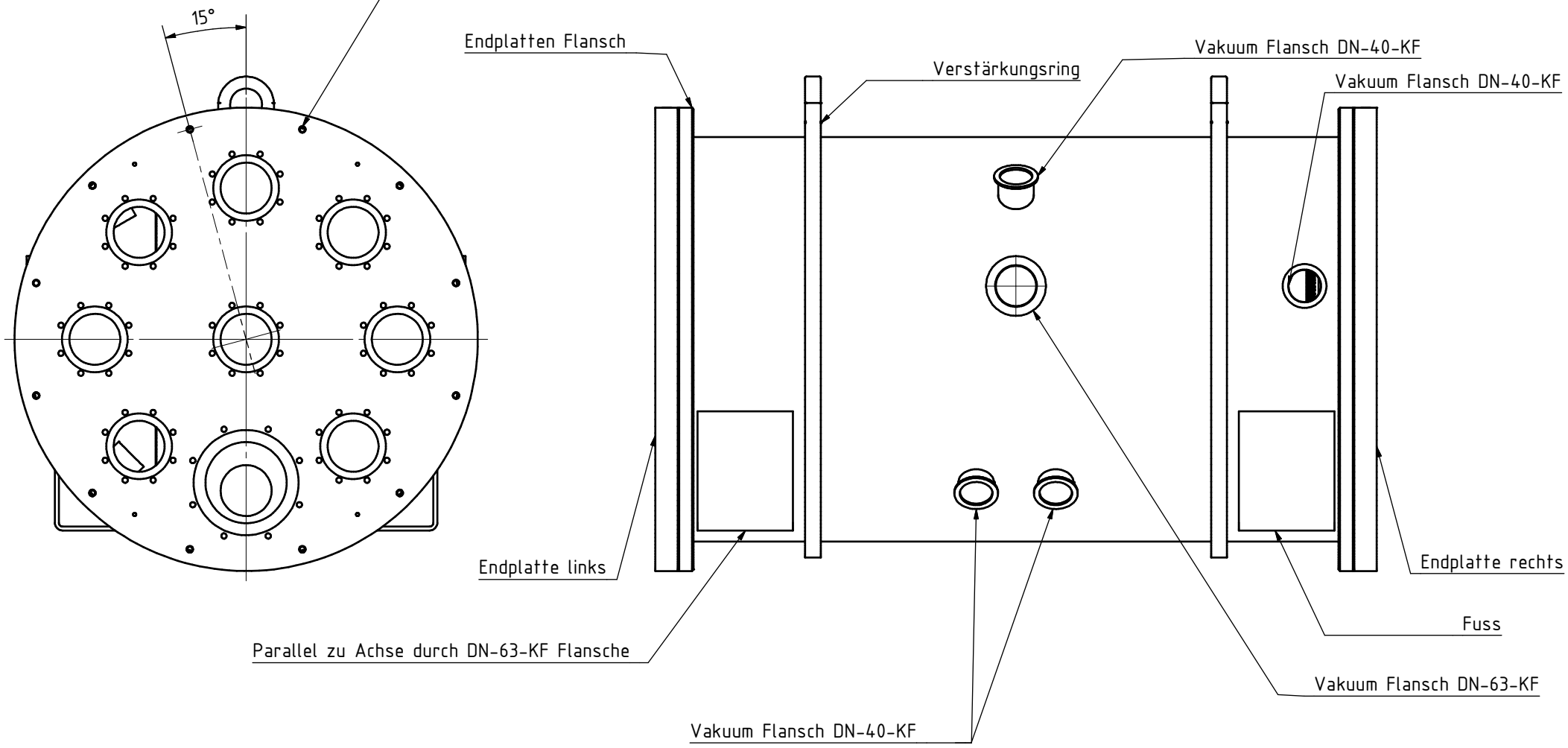

	Datum	Name
Gezeichnet	07.07.2014	zimmermann
Kontrolliert		
Norm		

Status	Änderungen	Datum	Name

Goni4-2

2

A3

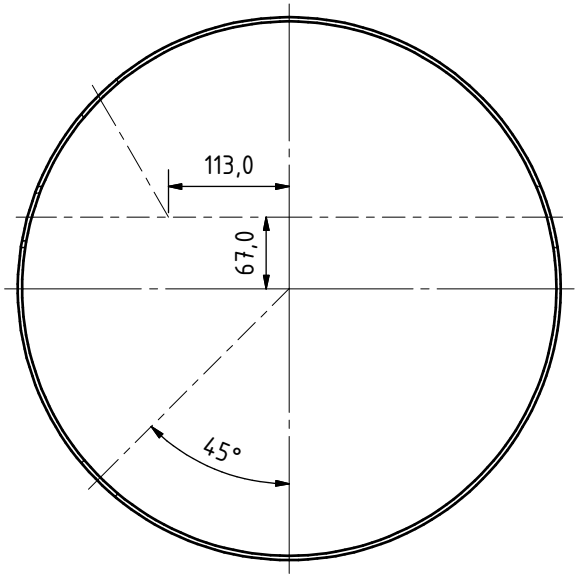

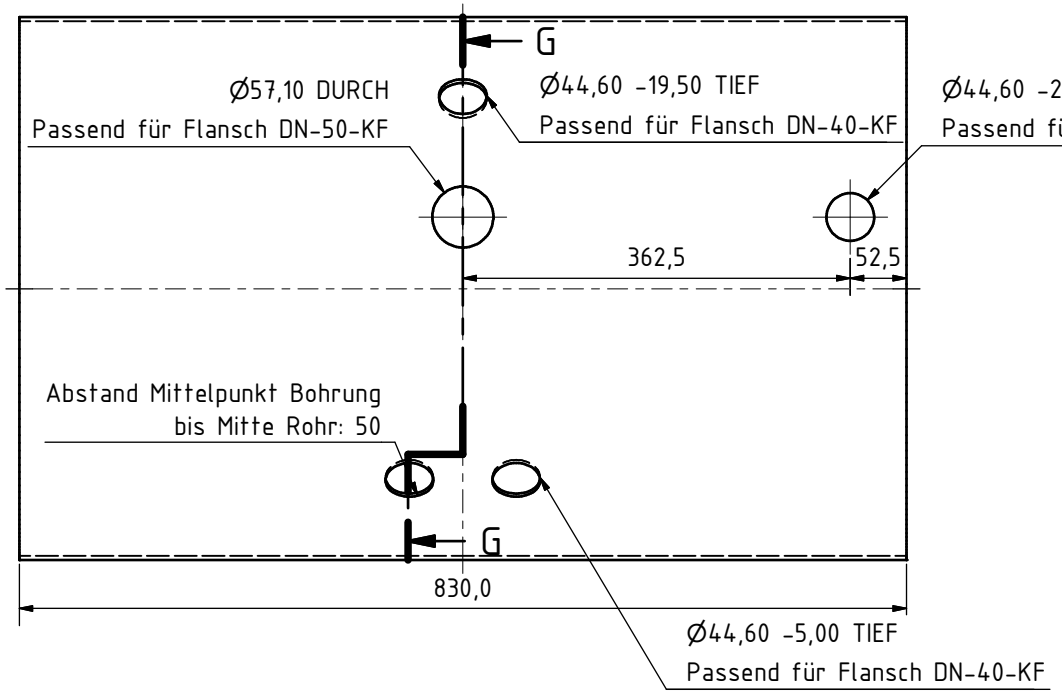

45° im Uhrzeigersinn gedreht

G-G (1 : 5)

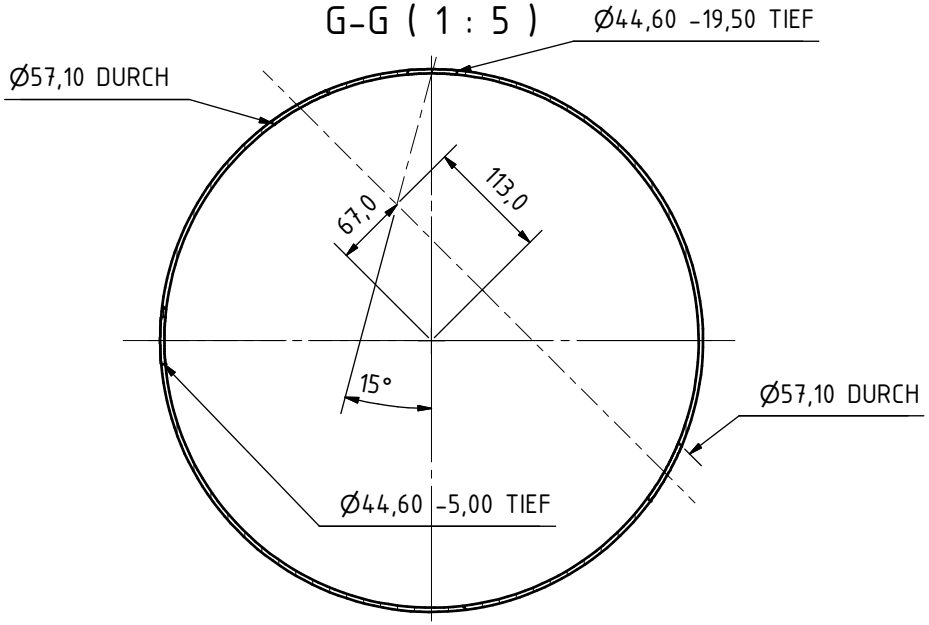

					Datum	Name	Rohr Material: Stahl 304 / 1.4301
				Gezeichnet	07.07.2014	zimmermann	
				Kontrolliert			
				Norm			
							Goni4-2
Status	Änderungen	Datum	Name				3 A3

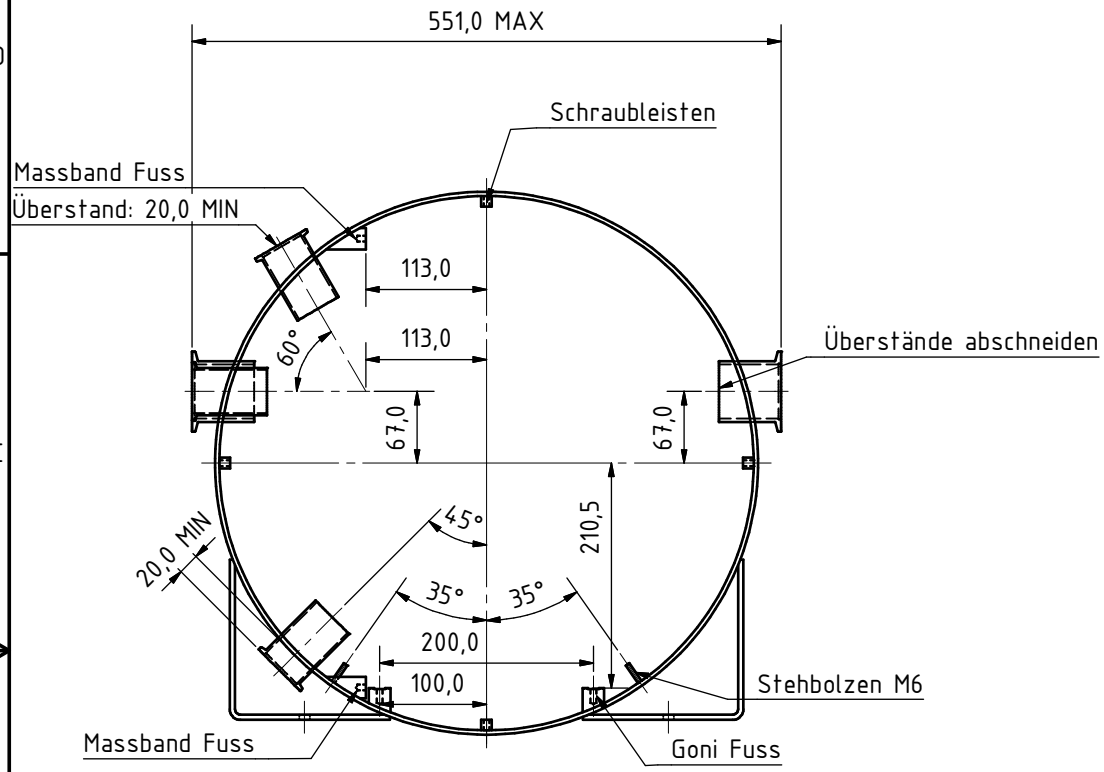

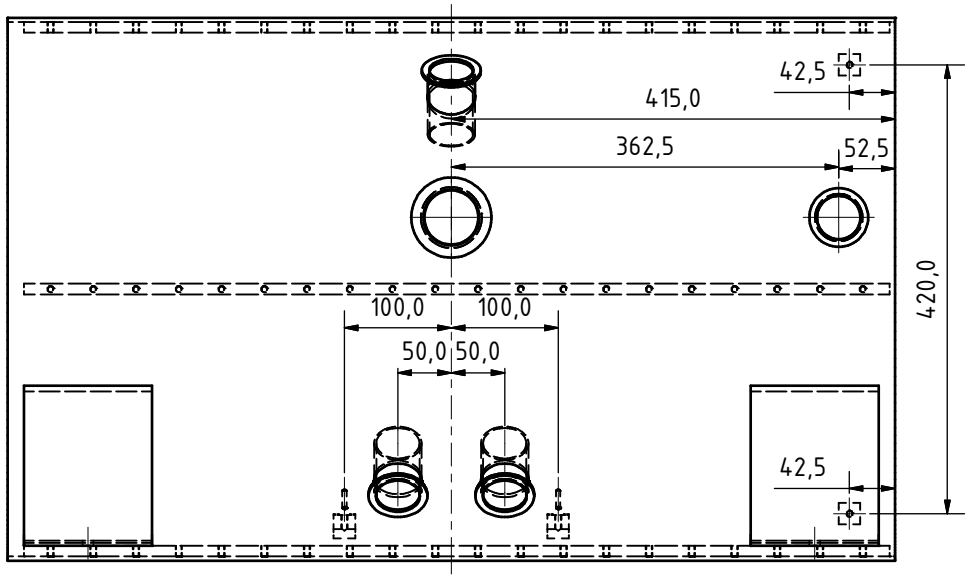

					Datum	Name
				Gezeichnet	07.07.2014	zimmermann
				Kontrolliert		
				Norm		
Status	Änderungen	Datum	Name			

Rohr mit angeschweißten Teilen

Goni4-2

4

A3

B (1 : 1)

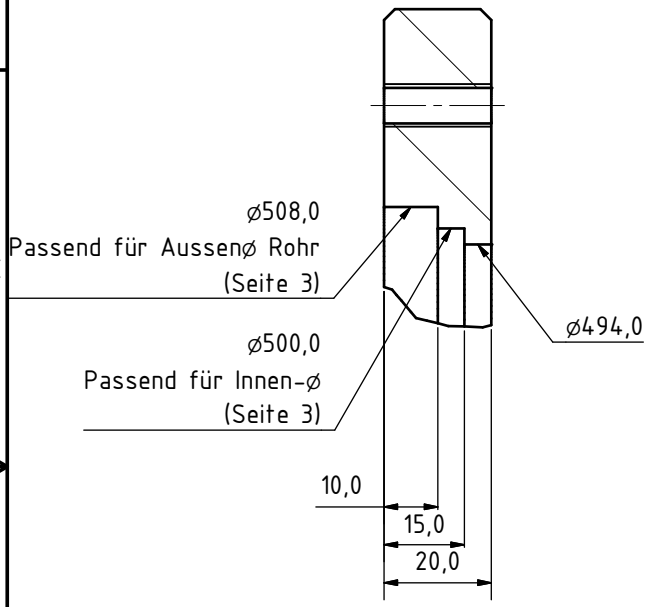

A-A (1 : 5)

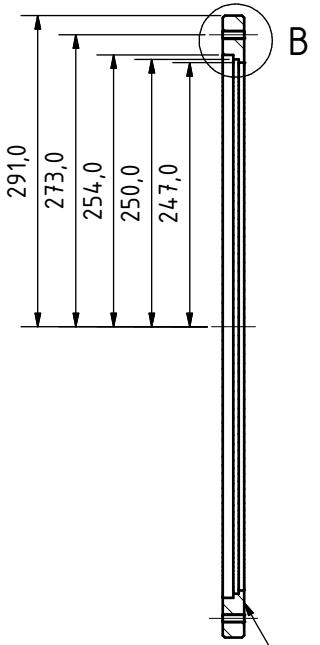

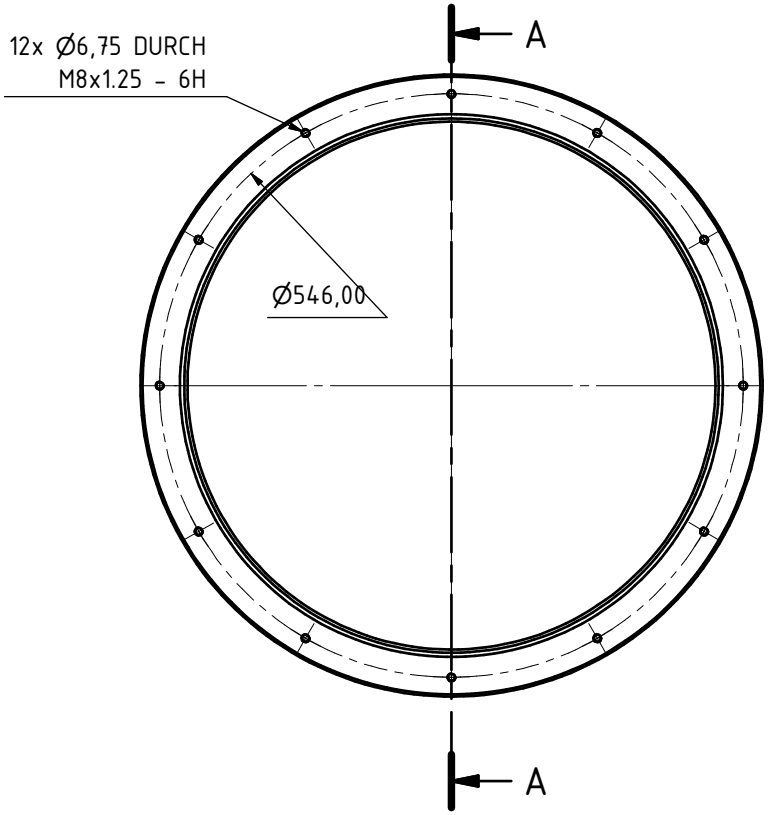

Dichtfläche (Plan drehen, evtl. nach dem Anscheißen)

					Datum	Name	Flansch für Endplatten links und rechts (2 Stück)
				Gezeichnet	07.07.2014	zimmermann	
				Kontrolliert			
				Norm			Material: Stahl 304 / 1.4301
							Goni4-2 — 5 — A3
Status	Änderungen	Datum	Name				

D (1 : 1)

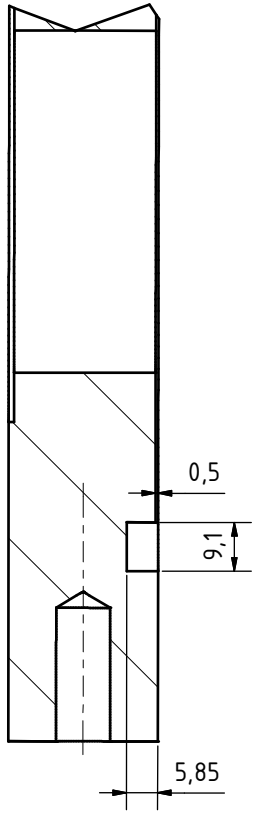

C-C (1 : 5)

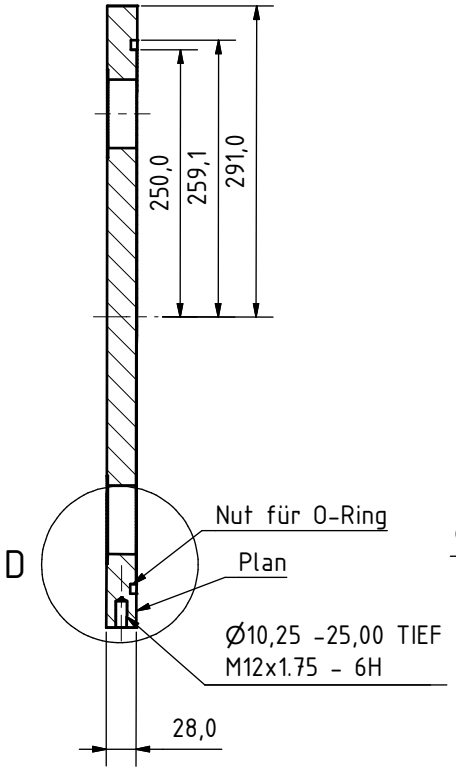

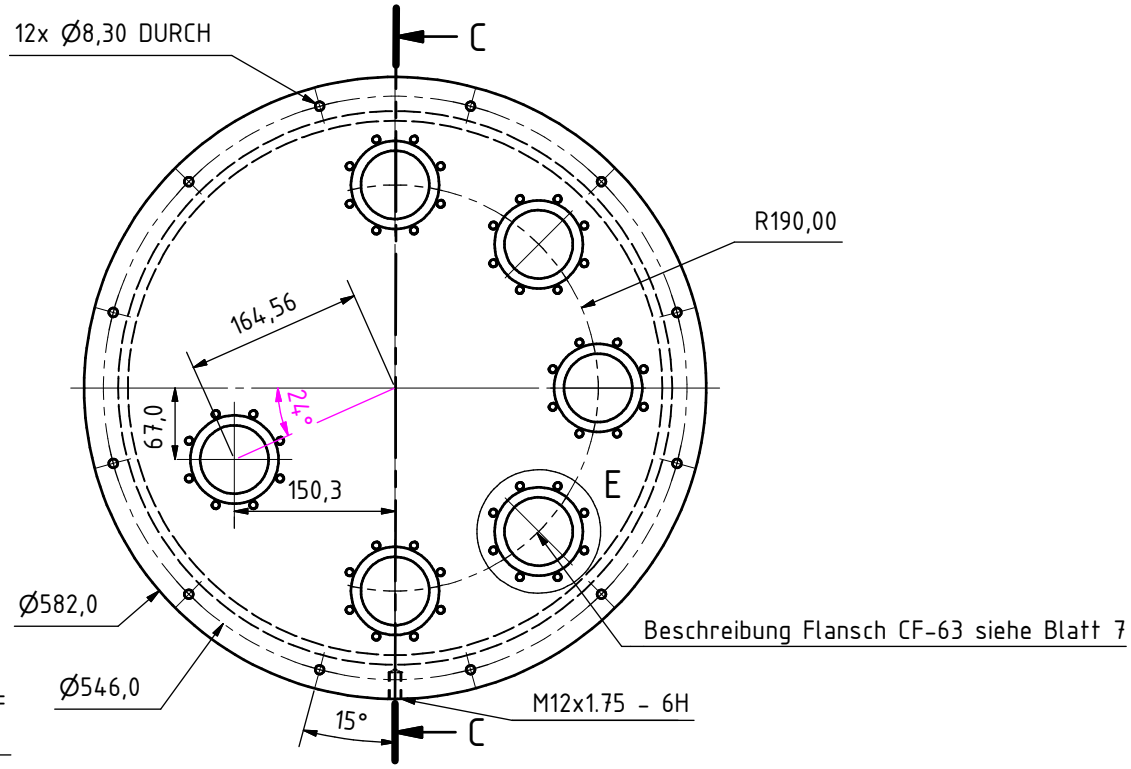

					Datum	Name
				Gezeichnet	07.07.2014	zimmermann
				Kontrolliert		
				Norm		
Status	Änderungen	Datum	Name			

Endplatte links
Material: AlMg4,5Mn

Goni4-2

6
A3

F-F (1 : 1)

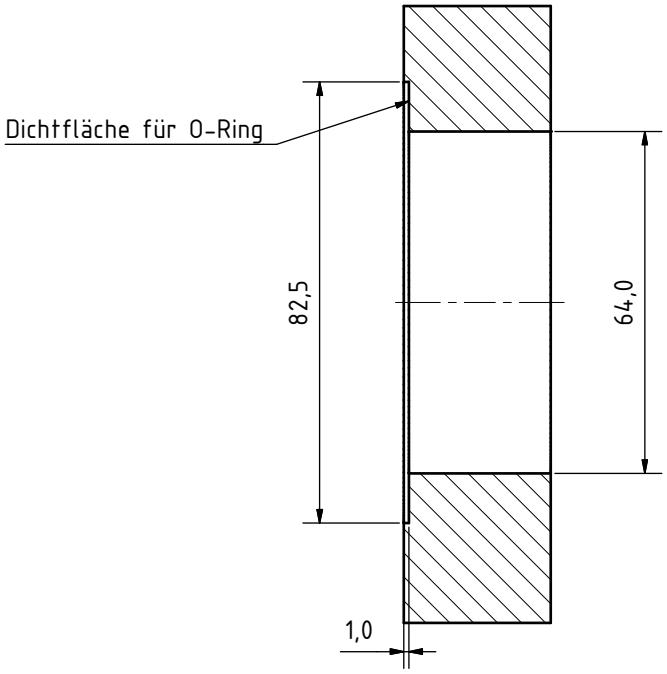

E (1 : 1)

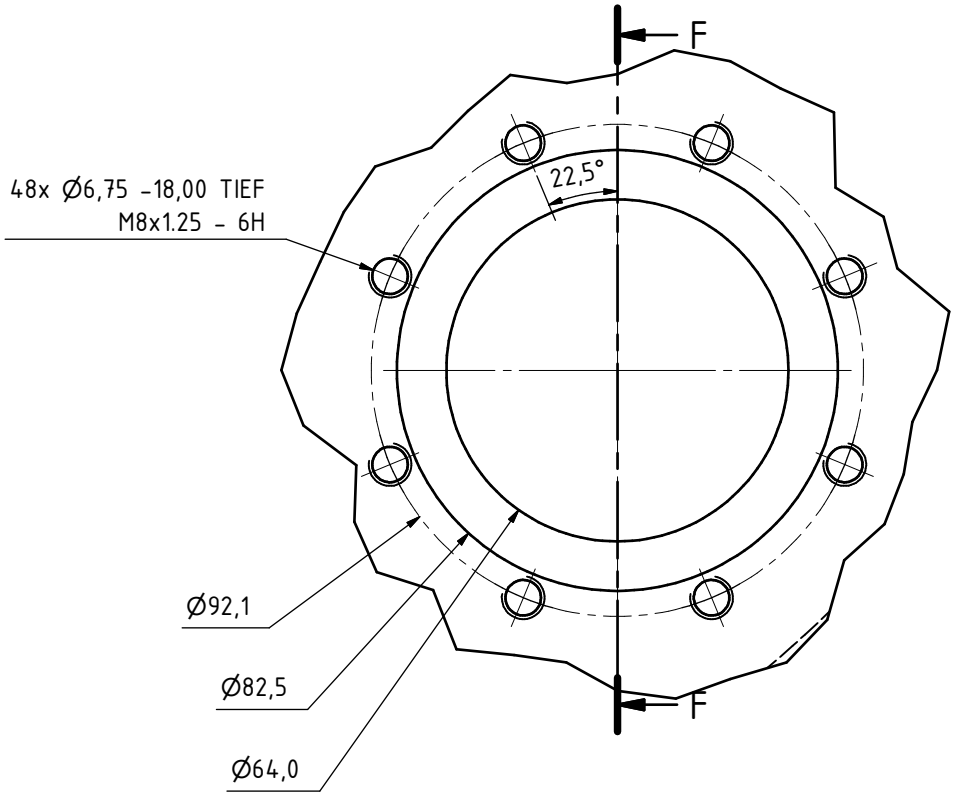

					Datum	Name
				Gezeichnet	07.07.2014	zimmermann
				Kontrolliert		
				Norm		
Status	Änderungen	Datum	Name			

DN 63 Flansche für Endplatte links und rechts

Goni4-2

7

A3

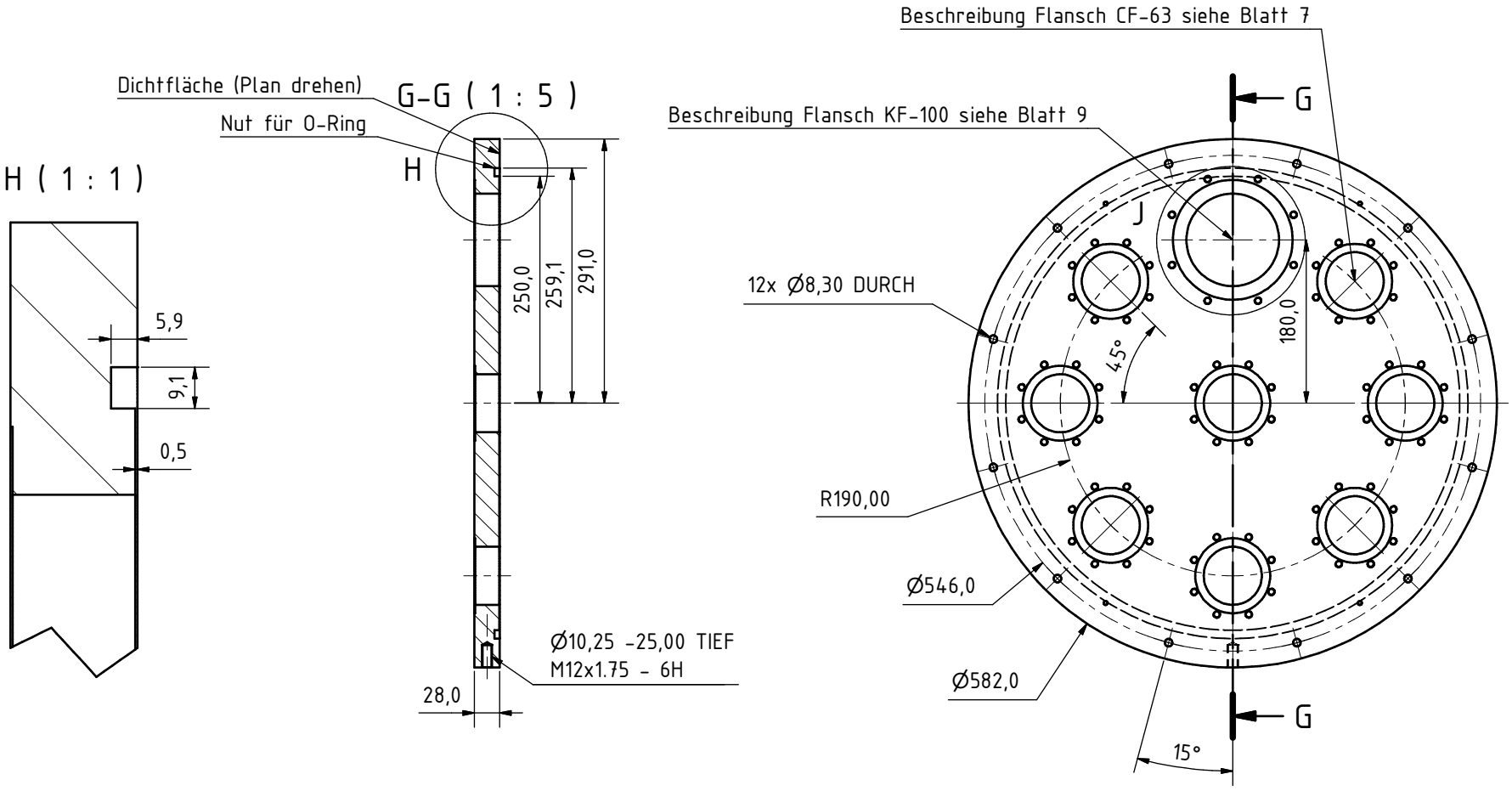

					Datum	Name	Endplatte rechts Material: AlMg4,5Mn	
				Gezeichnet	07.07.2014	zimmermann		
				Kontrolliert				
				Norm				
							Goni4-2	8 A3
Status	Änderungen	Datum	Name					

K-K (1 : 1)

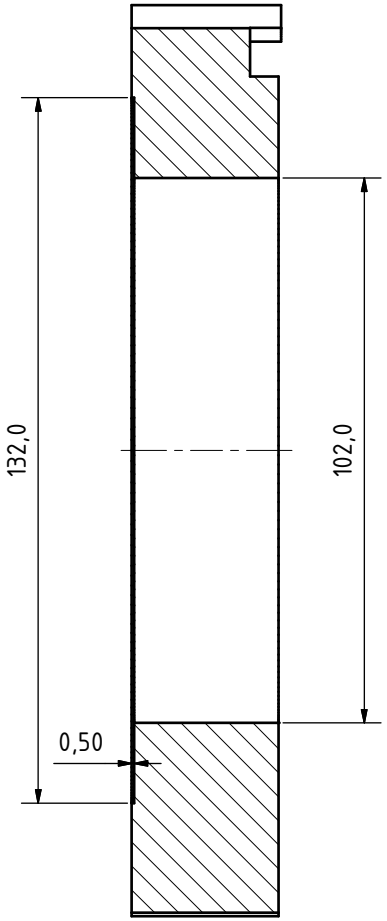

J (1 : 1)

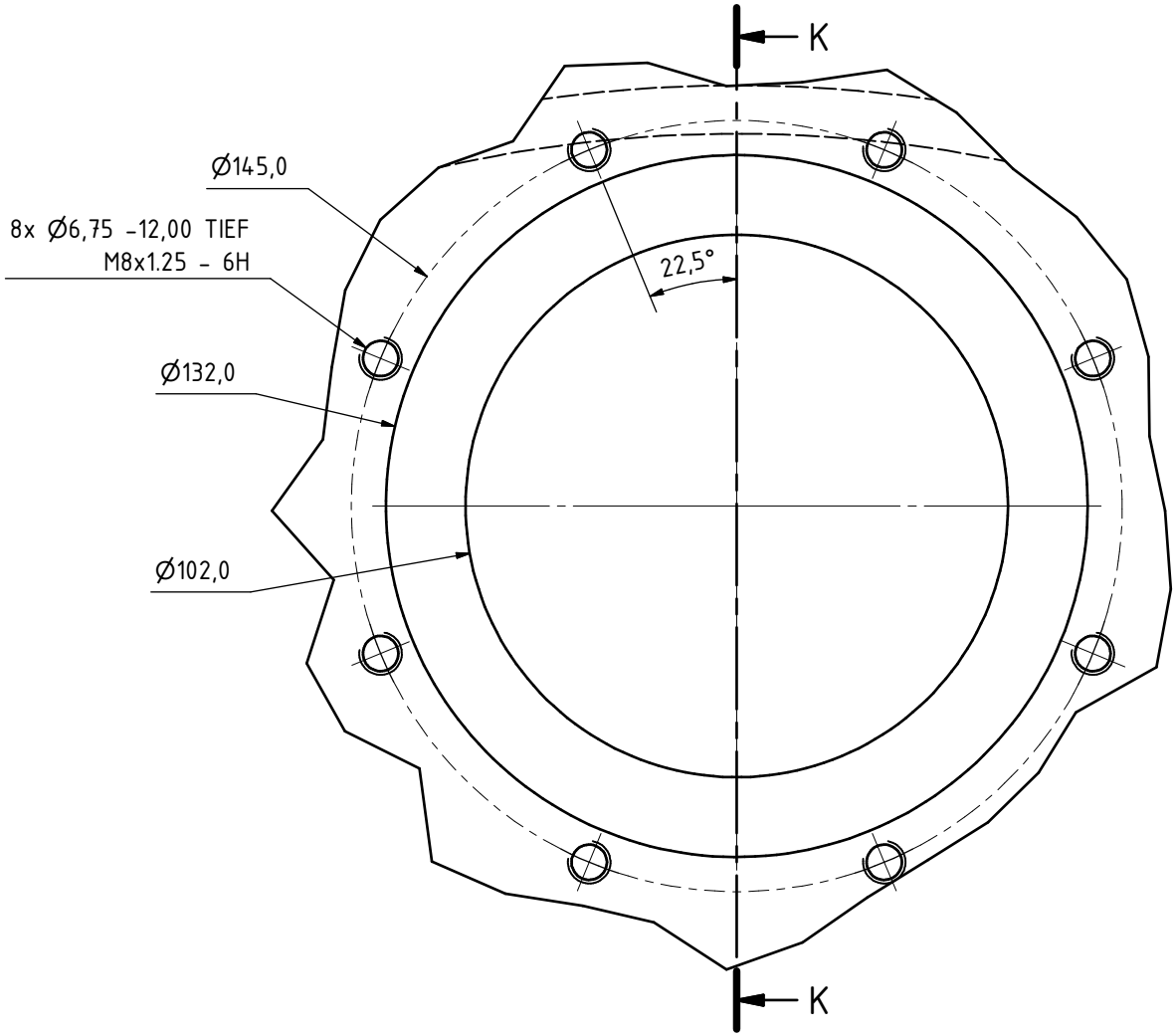

					Datum	Name
				Gezeichnet	07.07.2014	zimmermann
				Kontrolliert		
				Norm		
Status	Änderungen	Datum	Name			

DN 100 Flansch für Endplatte rechts

Goni4-2

9

A3

L-L (1 : 5)

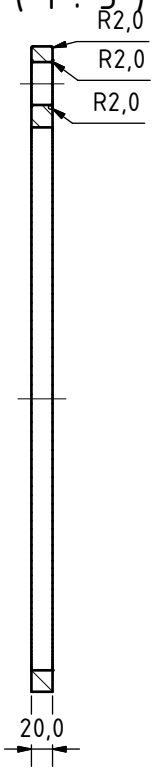

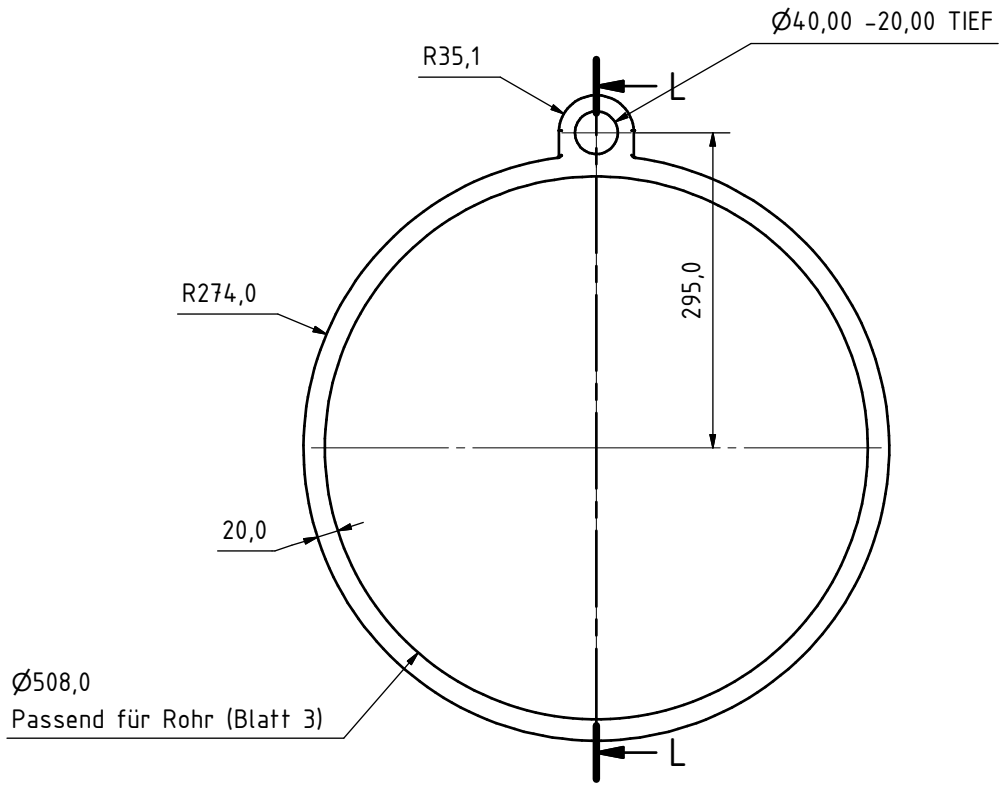

					Datum	Name
				Gezeichnet	07.07.2014	zimmermann
				Kontrolliert		
				Norm		
Status	Änderungen	Datum	Name			

Verteifunsring mit Kranöse
(2 Stück)
Material: Stahl 304 / 1.4301

Goni4-2

10
A3

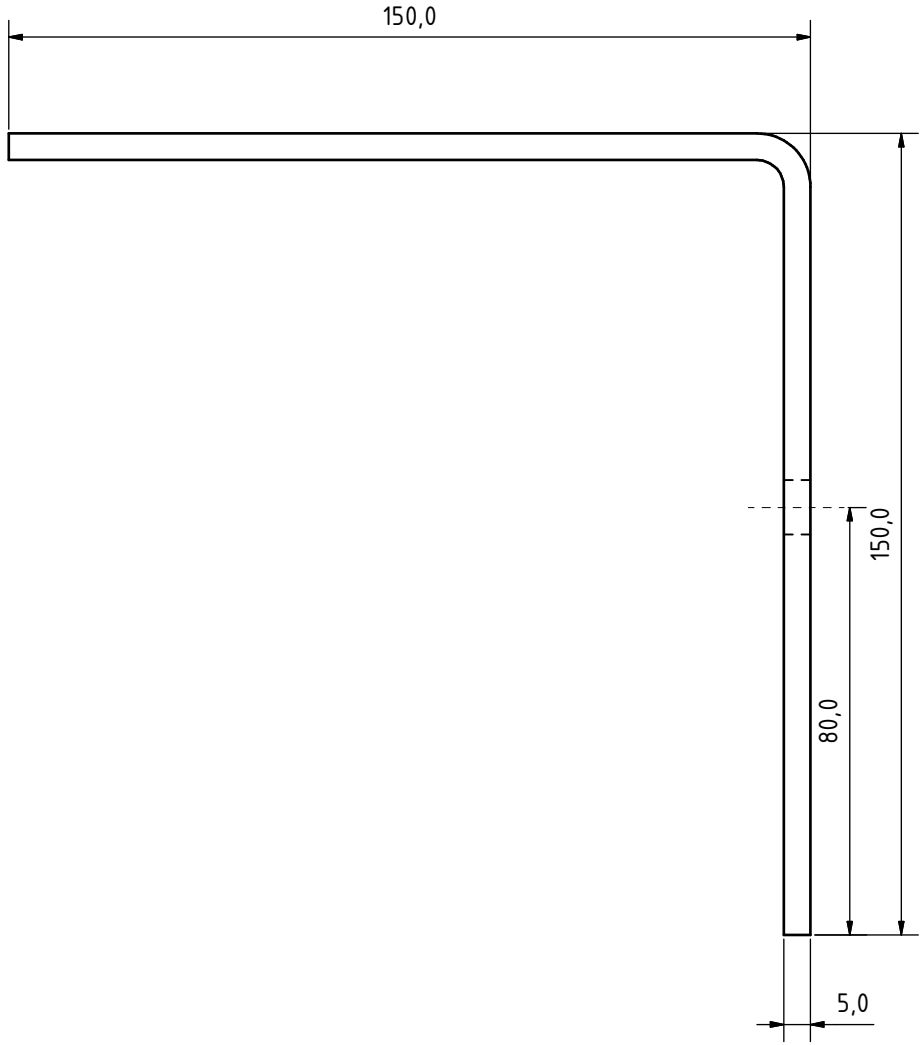

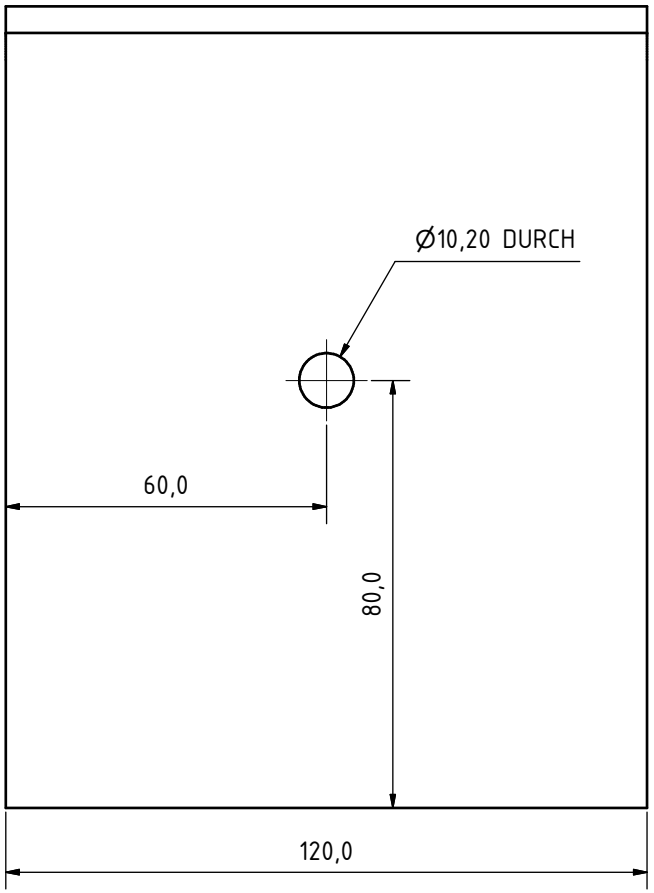

					Datum	Name
				Gezeichnet	07.07.2014	zimmermann
				Kontrolliert		
				Norm		

Fuss
(4 Stück)
Material: Stahl 304 / 1.4301

Goni4-2

11
A3

Status	Änderungen	Datum	Name

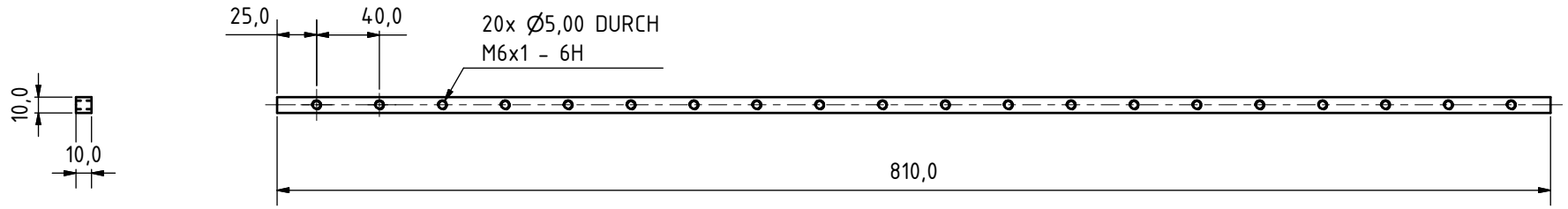

					Datum	Name
				Gezeichnet	07.07.2014	zimmermann
				Kontrolliert		
				Norm		
Status	Änderungen	Datum	Name			

Schraubleisten
(4 Stück)
Material: Stahl 304

Goni4-2

12
A3

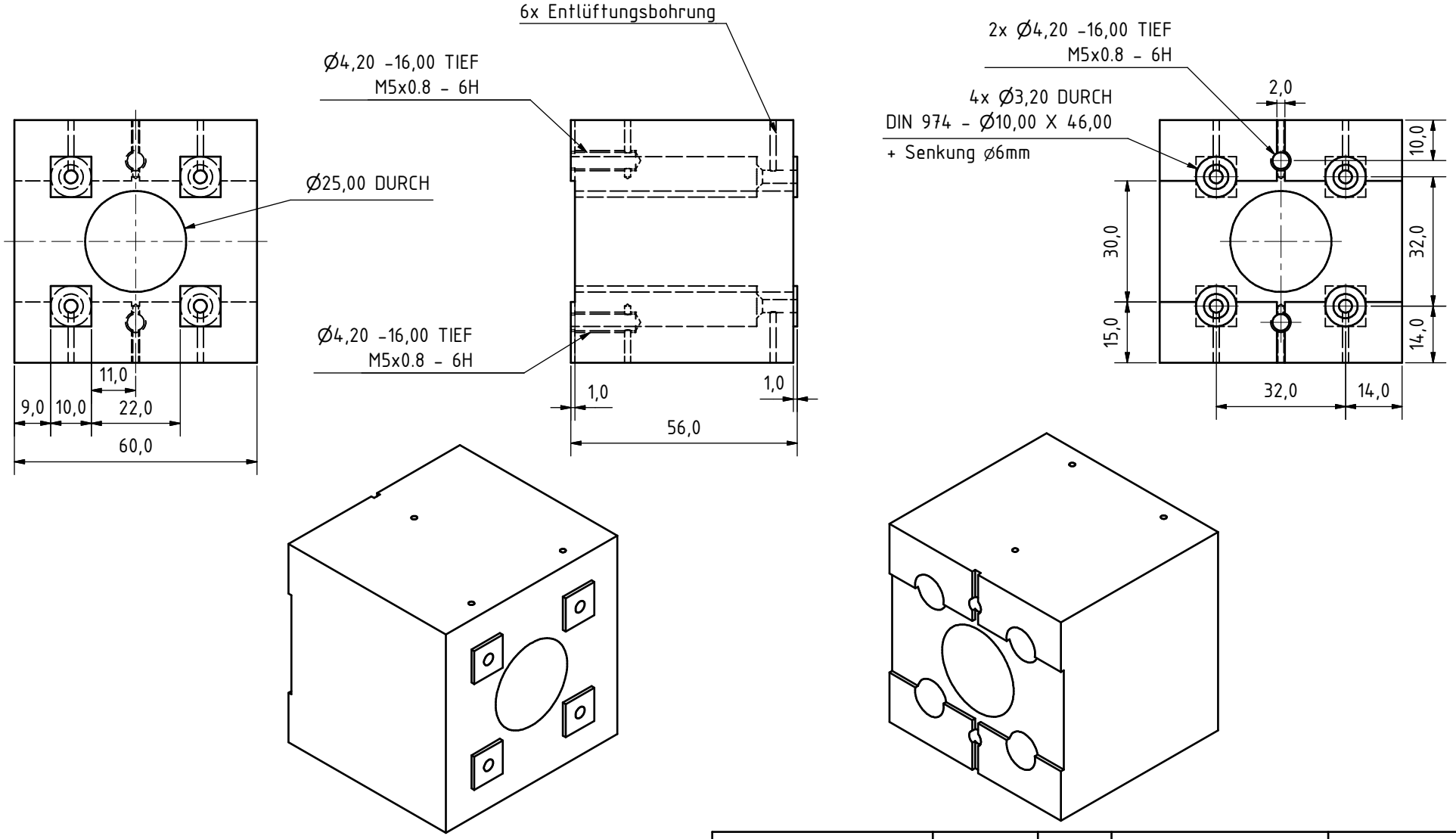

					Datum	Name
				Gezeichnet	07.07.2014	zimmermann
				Kontrolliert		
				Norm		
Status	Änderungen	Datum	Name			

Moller Spulen Abstandshalter
Material: Alu

Goni4-2

13
A3

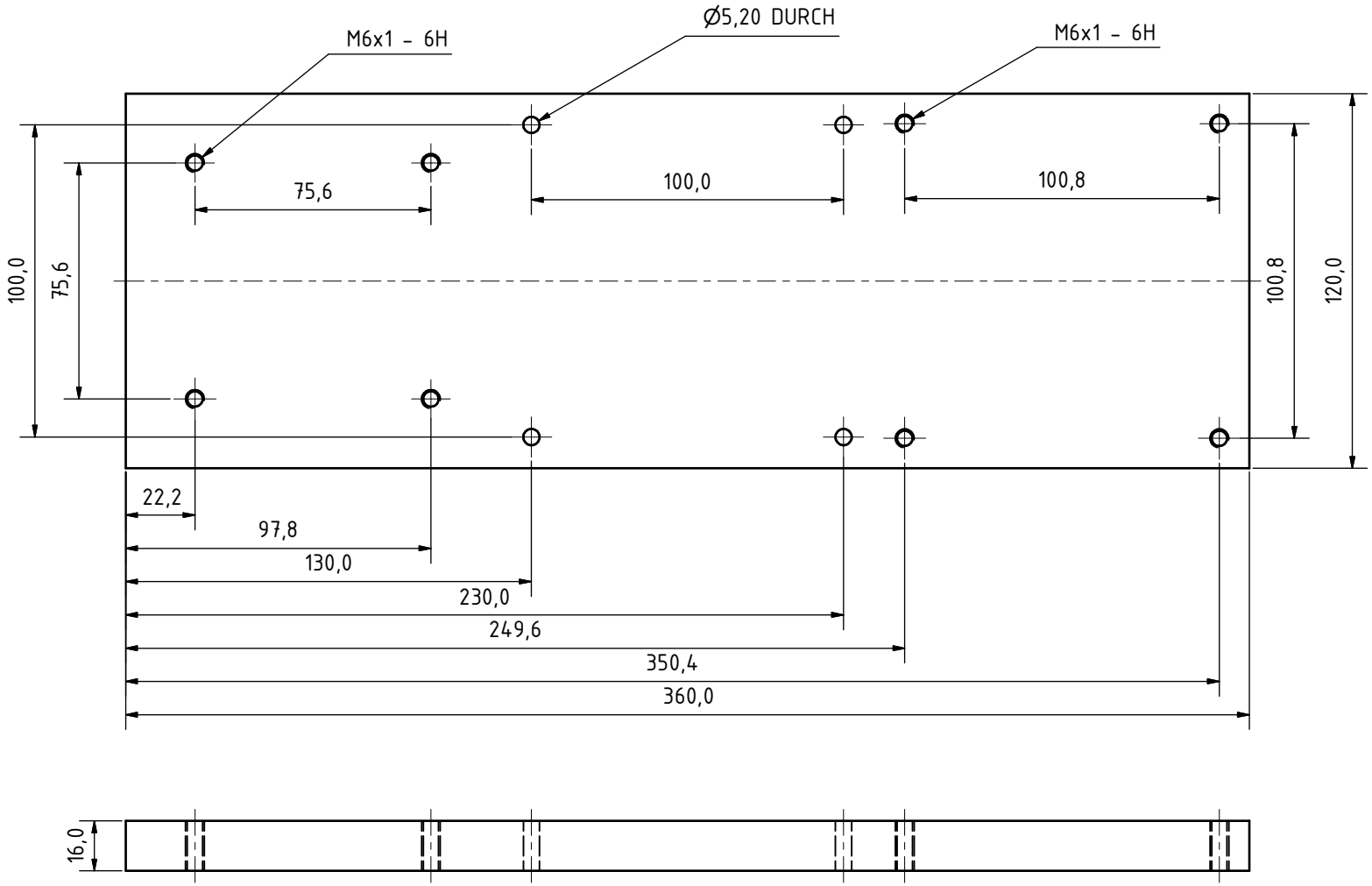

					Datum	Name
				Gezeichnet	07.07.2014	zimmermann
				Kontrolliert		
				Norm		
Status	Änderungen	Datum	Name			

Goniometer Adapterplatte
Material: Alu

Goni4-2

14
A3

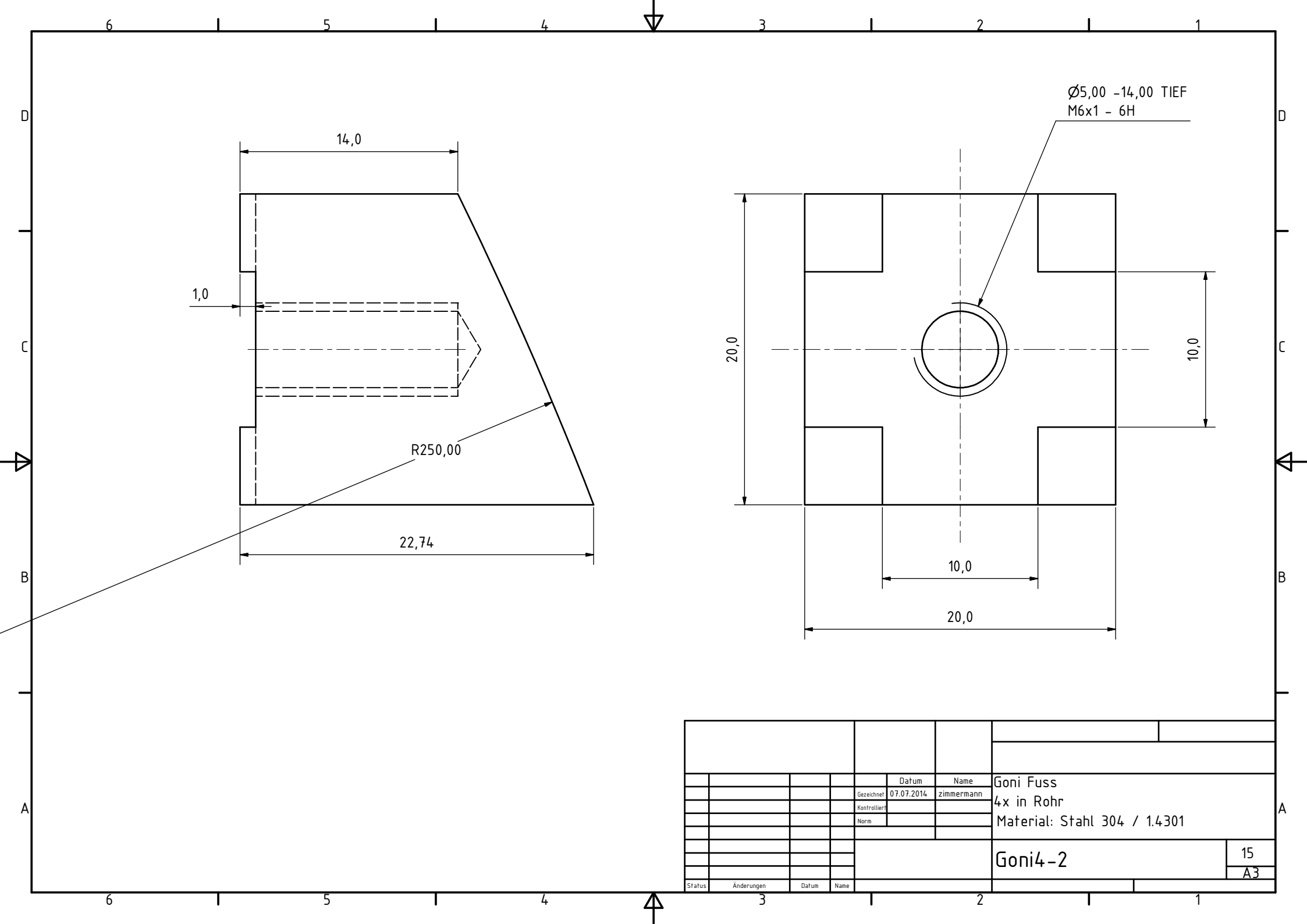

					Datum	Name
				Gezeichnet	07.07.2014	zimmermann
				Kontrolliert		
				Norm		

Goni Fuss
4x in Rohr
Material: Stahl 304 / 1.4301

Goni4-2

15
A3

Status	Änderungen	Datum	Name

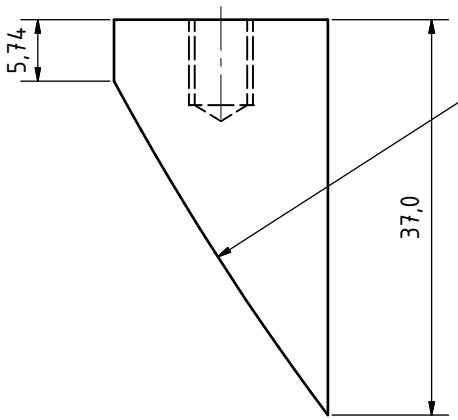

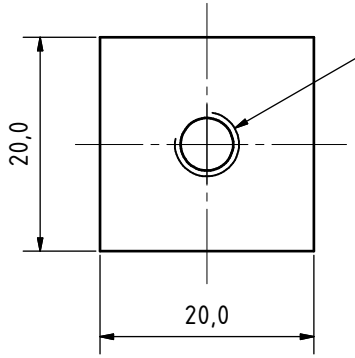

					Datum	Name
				Gezeichnet	07.07.2014	zimmermann
				Kontrolliert		
				Norm		
Status	Änderungen	Datum	Name			

Massband Fuss
2x in Rohr
Material: Stahl 304 / 1.4301

Goni4-2

16
A3

B.2 FEM Simulation

Analyse von Goni4-Belastungsanalyse.ipt

Autor:	zimmermann
Analyse erstellt am:	Dienstag, 29. Juli 2014 15:39:26
Letzte Änderung der Analyse:	Dienstag, 29. Juli 2014 15:54:21
Bericht erstellt am:	Montag, 25. April 2016 16:03:02
Datenbank:	*C:\Users\zimmermann\Documents\Vault\B1_Project\Workspace\Goniometer\Goni2\Goni4-Belastungsanalyse.ipa*
Software:	Autodesk Inventor Professional 2009 ANSYS Technology

Einführung

Die Belastungsanalyse von Autodesk Inventor Professional wurde zur Simulation des Verhaltens eines Maschinenbauteils unter Traglastbedingungen verwendet. Die in diesem Bericht aufgeführten Ergebnisse wurden durch die ANSYS-Technologie generiert.

Lehnen Sie einen Entwurf nicht allein basierend auf den in diesem Bericht enthaltenen Daten ab bzw. akzeptieren Sie ihn nicht allein basierend hierauf. Verwenden Sie zum Bewerten von Entwürfen diese Informationen zusammen mit Testdaten und der praktischen Erfahrung von Konstrukteuren und anderen Experten. Die ordnungsgemäße Herangehensweise an einen Konstruktionsentwurf setzt in der Regel physische Test als letzte Stufe der Prüfung der strukturellen Integrität auf der Grundlage einer gemessenen Präzision voraus.

Weitere Informationen über die Belastungsanalyse von AIP und ANSYS-Produkte für Autodesk Inventor erhalten Sie unter www.ansys.com/autodesk.

Geometrie und Netz

Mit der unten aufgeführten Relevanzeinstellung wurde die Feinheit des in dieser Analyse verwendeten Netzes gesteuert. Zur Referenz: Die Einstellung -100 erzeugt ein grobes Netz, schnelle Lösungen und Ergebnisse, die eine beträchtliche Unbestimmtheit aufweisen können. Eine Einstellung von +100 erzeugt ein feines Netz, führt zu längeren Lösungszeiten und einer geringeren Unbestimmtheit der Ergebnisse. Die Standard-Referenzeinstellung ist Null.

TABELLE 1
Goni4-Belastungsanalyse.ipt Statistik

Begrenzungsrahmenmaße	621,1 mm 582,0 mm 906,0 mm
Teilemasse	179,9 kg
Teilevolumen	2,226e+007 mm³
Netzrelevanzeinstellung	0
Knoten	222368
Elemente	124449

Die Begrenzungsrahmenmaße geben die Längen in globaler X-, Y- und Z-Richtung an.

Materialdaten

Bei dieser Analyse wird vom folgenden Materialverhalten ausgegangen:

- Linear - Spannung ist direkt proportional zur Belastung.
- Konstant - Alle Eigenschaften sind temperaturunabhängig.
- Homogen - Eigenschaften ändern sich im Volumen des Teils nicht.
- Isotrop - Die Materialeigenschaften sind in allen Richtungen identisch.

TABELLE 2
Edelstahl

Elastizitätsmodul	1,93e+005 MPa
Poissonsche Zahl	0,3
Massendichte	8,08e-006 kg/mm³
Zug-Streckgrenze	250,0 MPa
Zugfestigkeit	0,0 MPa

Lasten und Abhängigkeiten

Die folgenden Lasten und Abhängigkeiten wirken auf bestimmte Regionen des Teils. Regionen wurden durch die Auswahl von Flächen, Zylindern, Kanten oder Scheitelpunkten definiert.

TABELLE 3
Definitionen für Lasten und Abhängigkeiten

Name	Typ	Größe	Vektor
Druck 1	Flächenpressung	0,1 MPa	-
Festgelegte Abhängigkeit 1	Kante - Festgelegte Abhängigkeit	0,0 mm	0,0 mm 0,0 mm 0,0 mm

TABELLE 4
Abhängigkeitsreaktionen

Name	Kraft	Vektor	Moment	Moment-Vektor
Festgelegte Abhängigkeit 1	2602 N	387,1 N 490,8 N -2526 N	3,877e+005 N·mm	-1,055e+005 N·mm 3,731e+005 N·mm 4,922e-003 N·mm

Anmerkung: Vektordaten entsprechen den globalen X-, Y- und Z-Komponenten.

Ergebnisse

In der Tabelle unten sind alle strukturellen Ergebnisse der Analyse aufgeführt. Der folgende Abschnitt stellt Zahlen zur Verfügung, die die einzelnen Ergebnisse verteilt über die Fläche des Teils zeigen.

Der Sicherheitsfaktor wurde unter Verwendung der maximalen Entsprechung der Spannungsbruchtheorie für verformbare Materialien berechnet. Die Spannungsgrenze wurde durch Zug-Streckgrenze des Materials angegeben.

TABELLE 5
Strukturelle Ergebnisse

Name	Minimum	Maximum
Vergleichsspannung	4,601e-003 MPa	24,99 MPa
Maximale Hauptspannung	-2,992 MPa	9,91 MPa
Minimale Hauptspannung	-27,18 MPa	1,248 MPa
Deformation	0,0 mm	4,468e-002 mm
Sicherheitsfaktor	10,0	-

Zahlen

ZAHL 1
Vergleichsspannung

Vergleichsspannung
Typ: Vergleichsspannung
Einheit: MPa
25.04.2016 16:02

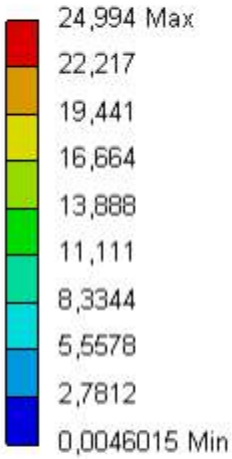

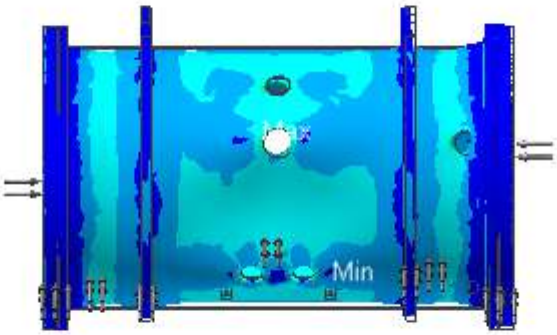

ZAHL 2
Maximale Hauptspannung

Maximale Hauptspannung
Typ: Maximale Hauptspannung
Einheit: MPa
25.04.2016 16:02

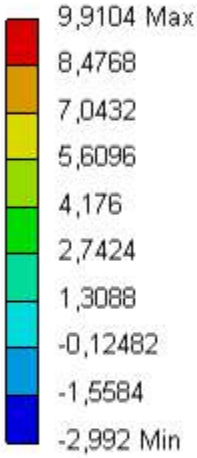

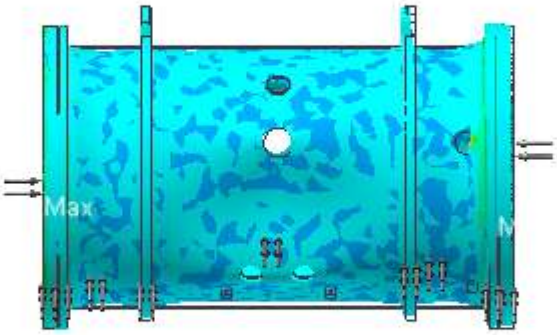

ZAHL 3
Minimale Hauptspannung

Minimale Hauptspannung
Typ: Minimale Hauptspannung
Einheit: MPa
25.04.2016 16:02

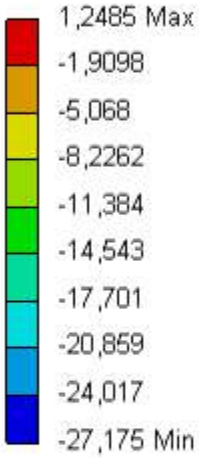

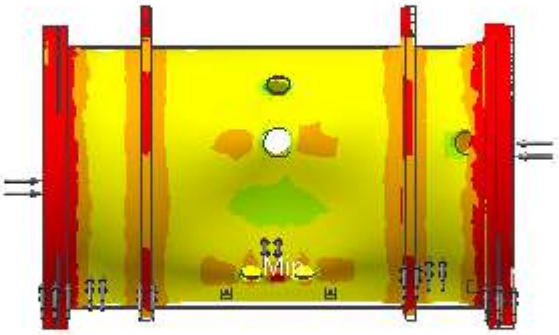

ZAHL 4
Deformation

Deformation
Typ: Deformation
Einheit: mm
25.04.2016 16:02

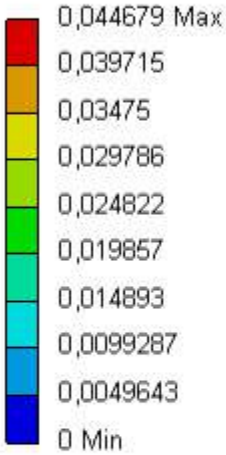

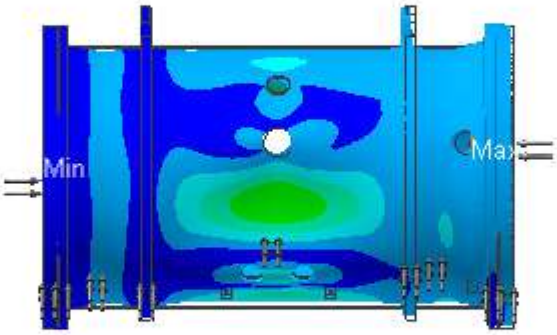

ZAHL 5
Sicherheitsfaktor

Sicherheitsfaktor
Typ: Sicherheitsfaktor
25.04.2016 16:03

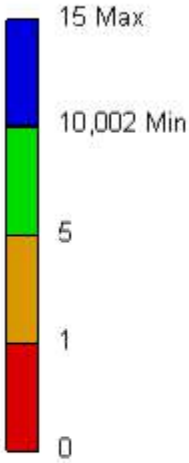

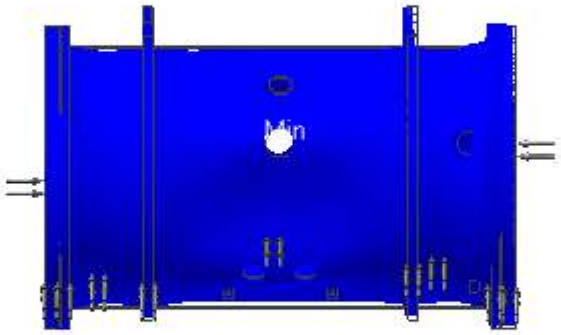

APPENDIX C

PCB: NIM-Isolator

The NIM-Isolator was designed to electrically isolate two different ground potentials. At the BGO-OD experiment it is used to isolate signals that are exchanged between the ELSA accelerator and the BGO-OD experiment. Ideally this should work with signal rates up to 200 MHz, which is the maximum frequency of the jTDC/jDisc module. Unfortunately this was not achieved, but the circuit is limited by the bandwidth of the used input and output stages (TI TLV3501) to 70 MHz. The isolation itself is achieved by TI ISO721 digital isolators and isolated DC/DC converters. The TI ISO721 can handle signals from DC to 150 mbps.

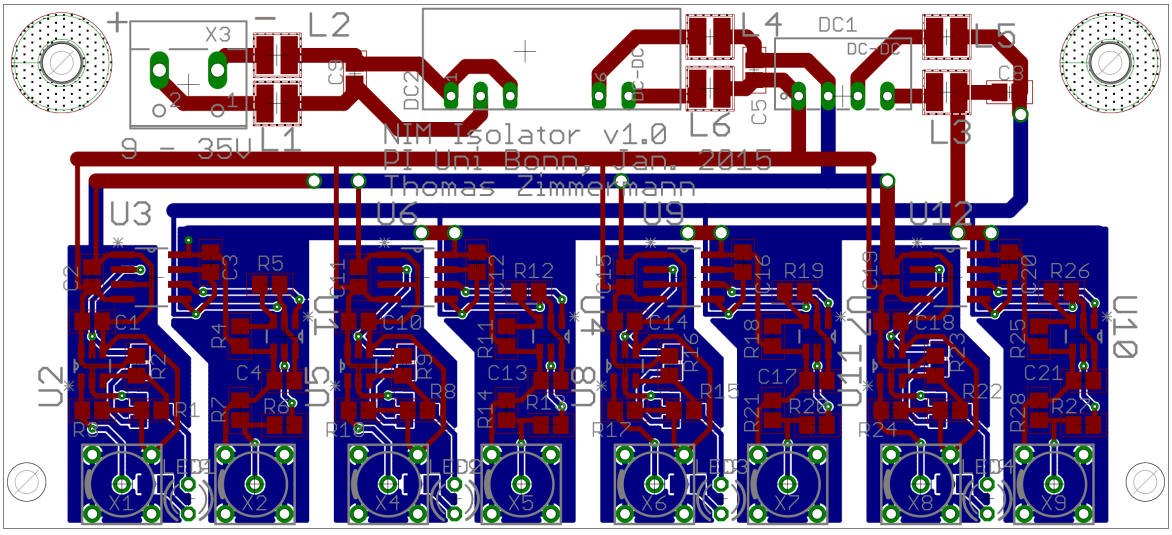

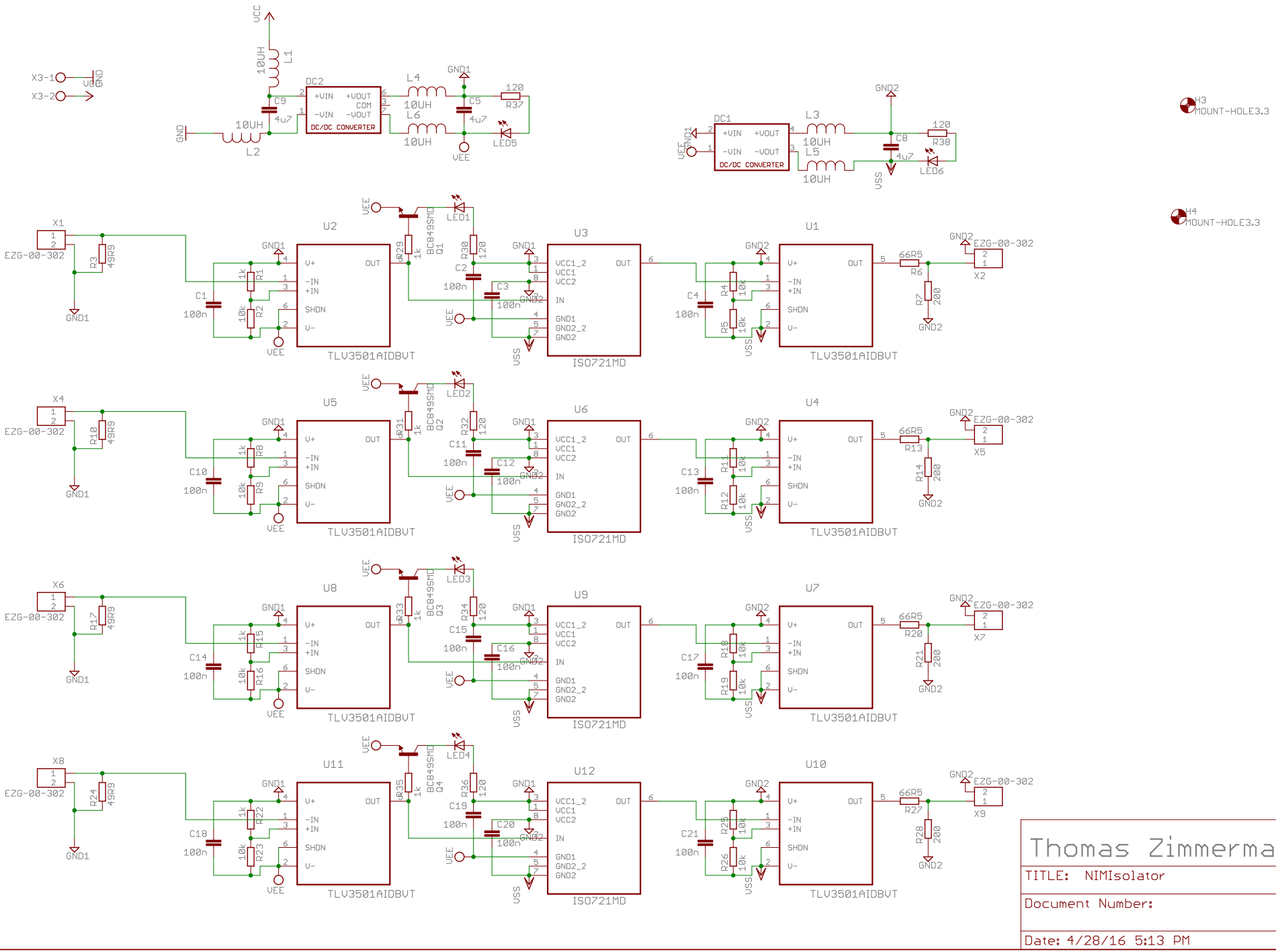
VCC
10UH
L1
DC2
+VIN
+VOUT
COM
-VIN
-VOUT
DC/DC CONVERTER
C9
4u7
L4
10UH
L6
10UH
GND1
C5
4u7
120
R37
LED5
VEE
GND
L2
X3-1
X3-2
DC1
L3
L5
C8
R38
LED6
VSS
GND2
H3
MOUNT-HOLE3.3
H4
MOUNT-HOLE3.3
X1
EZG-00-302
R3
49R9
C1
100n
R1
1k
R2
10k
U2
TLV3501AIDBVT
R29
1k
BC849SMD
Q1
LED1
R30
120
C2
100n
C3
100n
U3
ISO721MD
VCC1_2
VCC1
VCC2
IN
GND1
GND2_2
GND2
OUT
U1
R4
10k
R5
10k
66R5
R6
R7
200
X2
X4
R10
49R9
C10
100n
R8
1k
R9
10k
U5
R31
1k
Q2
LED2
R32
120
C11
100n
C12
100n
U6
C13
100n
R11
10k
R12
10k
U4
R13
R14
200
X5
X6
R17
49R9
C14
100n
R15
1k
R16
10k
U8
R33
1k
Q3
LED3
R34
120
C15
100n
C16
100n
U9
C17
100n
R18
10k
R19
10k
U7
R20
R21
200
X7
X8
R24
49R9
C18
100n
R22
1k
R23
10k
U11
R35
1k
Q4
LED4
R36
120
C19
100n
C20
100n
U12
C21
100n
R25
10k
R26
10k
U10
R27
R28
200
X9
Thomas Zimmermann
TITLE: NIMIsolator
Document Number:
REV: 1
Date: 4/28/16 5:13 PM
Sheet: 1/1

APPENDIX D

PCB: PT100USB

The PT1000USB was built to measure temperatures with PT1000 platinum sensors. At the BGO-OD experiment usally Maxim DS18B20 1-wire temperature sensors are used, but in certain conditions these are not suited, e.g. when the space is very constrained or the radiation is to high. For these purposes the PT1000 sensors are used, as they are radiation hard and can have very small dimensions. The PT1000USB is based on the “Bausatz PT1000 Messwandler” from Pollin Electronic, extended by an AtMega8U2 micro controller, to provide a usb-to-serial interface.

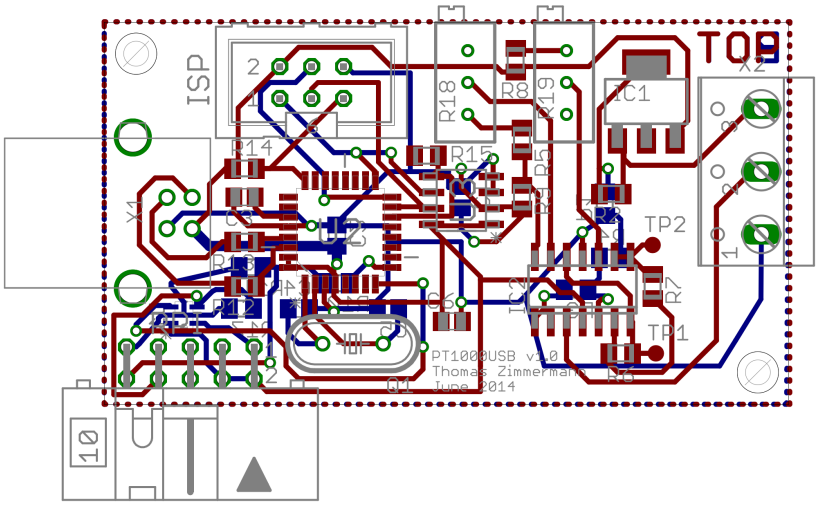

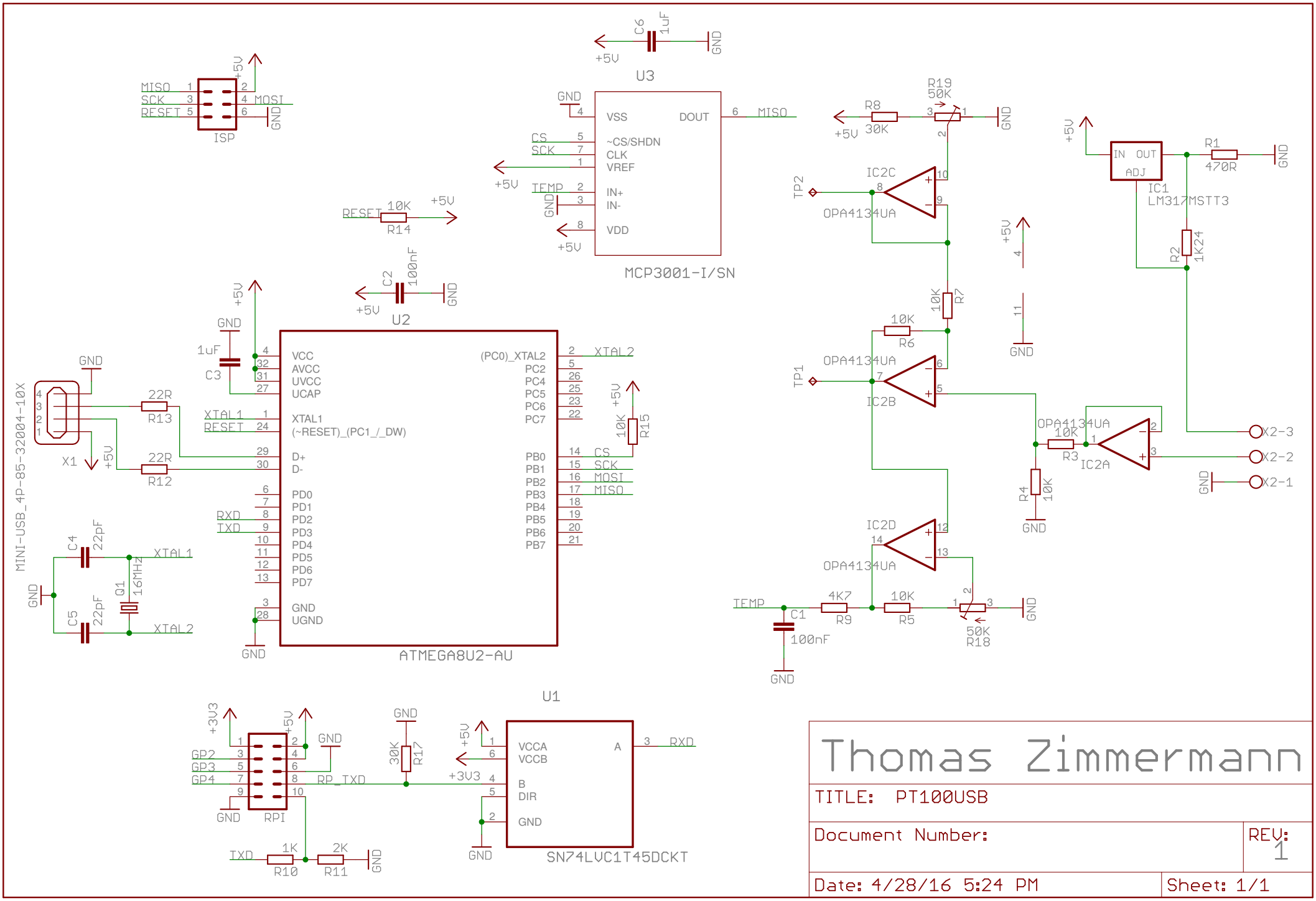

Thomas Zimmermann	
TITLE: PT100USB	
Document Number:	REV: 1
Date: 4/28/16 5:24 PM	Sheet: 1/1

APPENDIX E

$K^+\Lambda$ Line Shapes

The following figures show the missing mass to the K^+ in every $\Theta^{c.m.}_{K^+}$ and W bin. Every spectrum is fitted with two Gaussian functions as described in section 5.2.

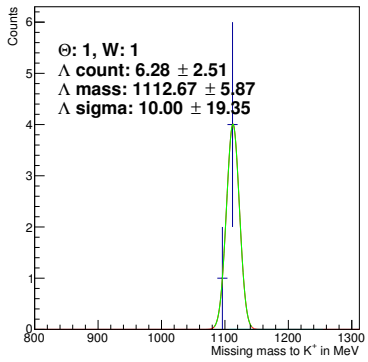

(a) $\Theta^{c.m.}_{K^+} = 3°$ to $6°$

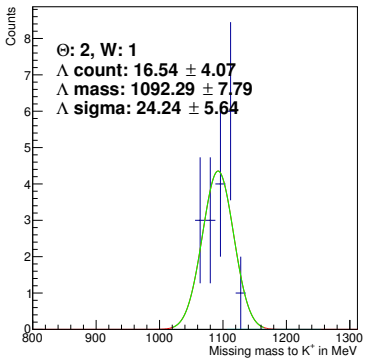

(b) $\Theta^{c.m.}_{K^+} = 6°$ to $9°$

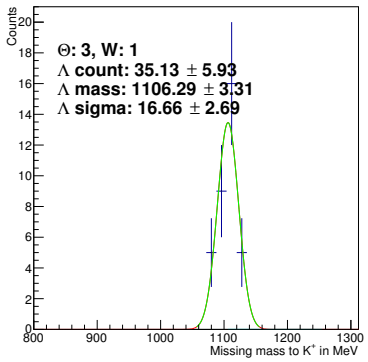

(c) $\Theta^{c.m.}_{K^+} = 9°$ to $12°$

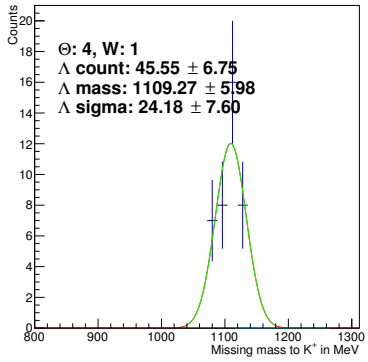

(d) $\Theta^{c.m.}_{K^+} = 12°$ to $15°$

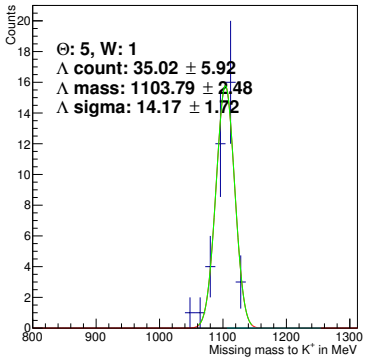

(e) $\Theta^{c.m.}_{K^+} = 15°$ to $18°$

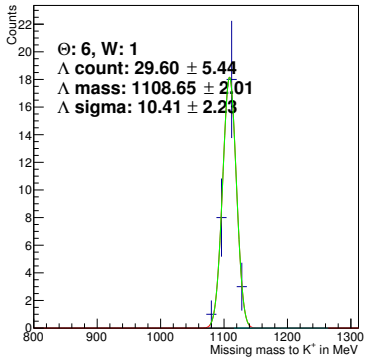

(f) $\Theta^{c.m.}_{K^+} = 18°$ to $21°$

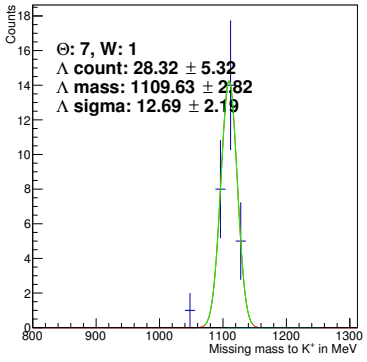

(g) $\Theta^{c.m.}_{K^+} = 21°$ to $24°$

Figure E.1: $W = 1.6\,\text{GeV}$ to $1.7\,\text{GeV}$

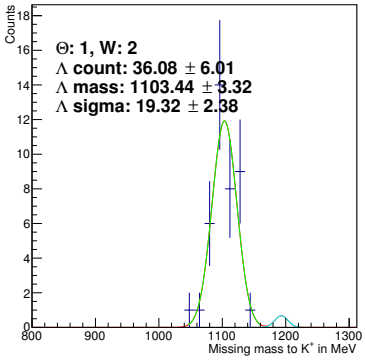

(a) $\Theta_{K^+}^{c.m.} = 3°$ to $6°$

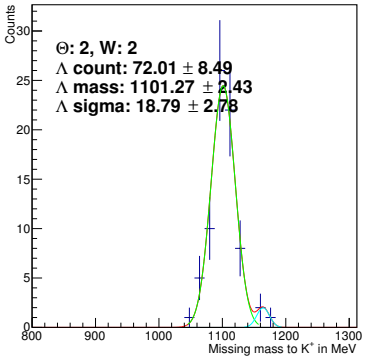

(b) $\Theta_{K^+}^{c.m.} = 6°$ to $9°$

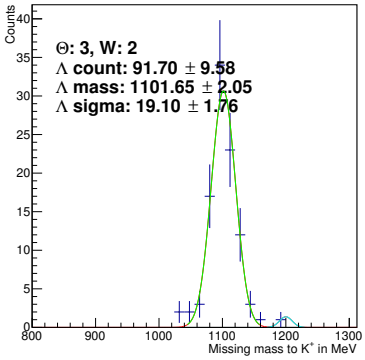

(c) $\Theta_{K^+}^{c.m.} = 9°$ to $12°$

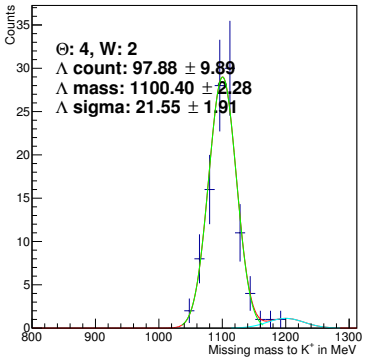

(d) $\Theta_{K^+}^{c.m.} = 12°$ to $15°$

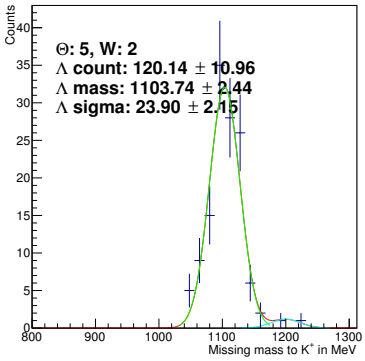

(e) $\Theta_{K^+}^{c.m.} = 15°$ to $18°$

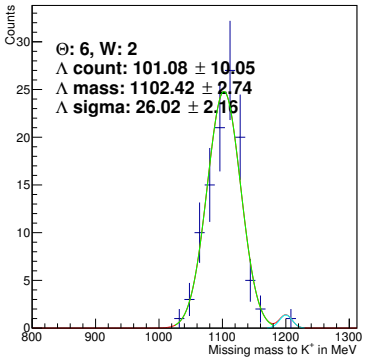

(f) $\Theta_{K^+}^{c.m.} = 18°$ to $21°$

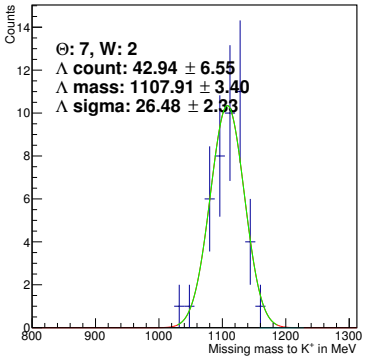

(g) $\Theta_{K^+}^{c.m.} = 21°$ to $24°$

Figure E.2: $W = 1.7\,\text{GeV}$ to $1.8\,\text{GeV}$

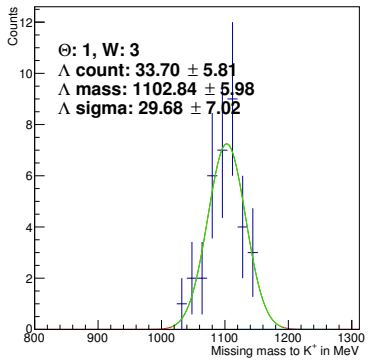

(a) $\Theta^{c.m.}_{K^+} = 3°$ to $6°$

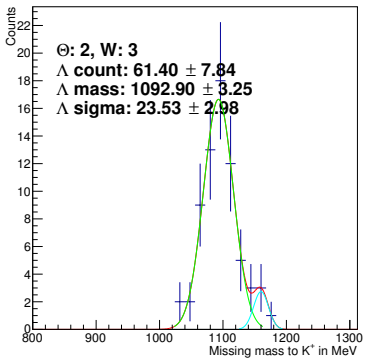

(b) $\Theta^{c.m.}_{K^+} = 6°$ to $9°$

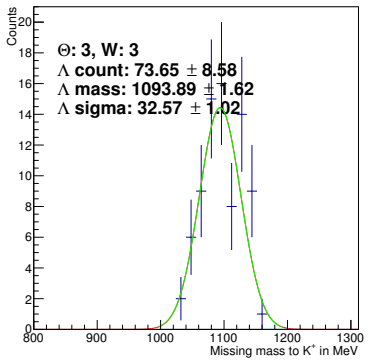

(c) $\Theta^{c.m.}_{K^+} = 9°$ to $12°$

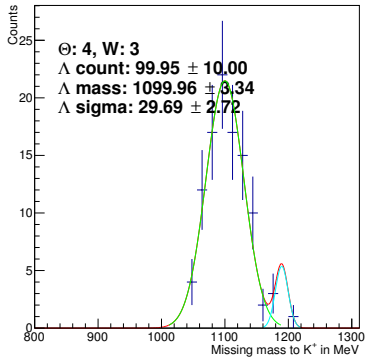

(d) $\Theta^{c.m.}_{K^+} = 12°$ to $15°$

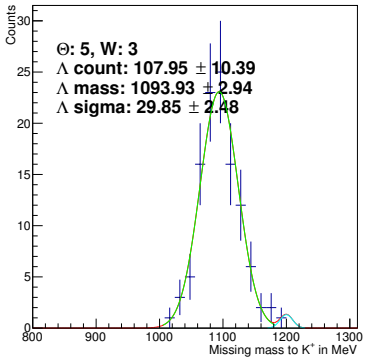

(e) $\Theta^{c.m.}_{K^+} = 15°$ to $18°$

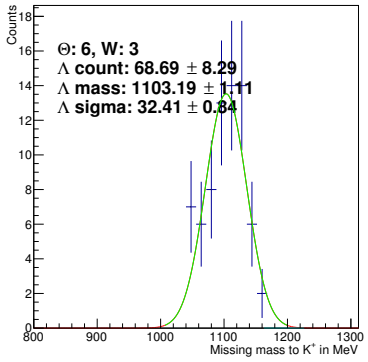

(f) $\Theta^{c.m.}_{K^+} = 18°$ to $21°$

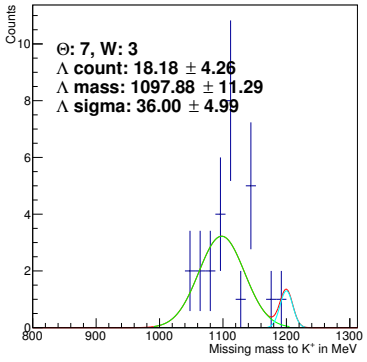

(g) $\Theta^{c.m.}_{K^+} = 21°$ to $24°$

Figure E.3: $W = 1.8\,\text{GeV}$ to $1.9\,\text{GeV}$

APPENDIX E

Bibliography

[Aai+15] R. Aaij et al., *Observation of $J/\psi p$ Resonances Consistent with Pentaquark States in $\Lambda_b^0 \to J/\psi K^- p$ Decays*, Phys. Rev. Lett. **115** (7 Aug. 2015) p. 072001, URL: http://link.aps.org/doi/10.1103/PhysRevLett.115.072001.

[Afz15] F. N. Afzal, *Measurement of the double polarization observables E and G at the Crystal Ball experiment at MAMI* (2015), Proceedings of the XVIth International Workshop in Polarized Sources, Targets, and Polarimetry, URL: http://pos.sissa.it/archive/conferences/243/036/PSTP2015_036.pdf.

[Ago+03] S. Agostinelli et al., *Geant4–a simulation toolkit*, Nuclear Instruments and Methods in Physics Research Section A: Accelerators, Spectrometers, Detectors and Associated Equipment **506**.3 (2003) pp. 250–303, ISSN: 0168-9002, URL: http://geant4.cern.ch.

[Ale15] S. Alef, *Scintillating Fibre detector and kinematic fitting for the BGO-OD experiment*, master thesis: Rheinische Friedrich-Wilhelms-Universität Bonn, Sept. 2015, URL: https://www.hsag.physik.uni-bonn.de/forschung/diplom-doktorarbeiten/diplom-masterarbeiten/Masterarbeit_Stefan%20Alef.pdf.

[Apy+98] A. Apyan et al., *Circularly polarized photon beams produced by channeled longitudinally polarized electrons*, Nuclear Instruments and Methods in Physics Research Section B: Beam Interactions with Materials and Atoms **145**.1–2 (1998) pp. 142–145, ISSN: 0168-583X, URL: http://www.sciencedirect.com/science/article/pii/S0168583X98002572.

[ASW03] R. A. Arndt, I. I. Strakovsky, and R. L. Workman, *THE SAID PWA PROGRAM*, International Journal of Modern Physics A **18**.03 (2003) pp. 449–455, eprint: http://www.worldscientific.com/doi/pdf/10.1142/S0217751X0301437X, URL: http://www.worldscientific.com/doi/abs/10.1142/S0217751X0301437X.

[Bal13] A. Balling, personal communication, Jan. 30, 2013.

[Bar+05] O. Bartholomy et al., *Neutral-PionPhotoproduction off Protons in the Energy Range 0.3 GeV > E_γ > 3 GeV*, Phys. Rev. Lett. **94** (1 Jan. 2005) p. 012003, URL: http://link.aps.org/doi/10.1103/PhysRevLett.94.012003.

[Bau14] P. Bauer, *Aufbau und Test eines schnellen Flugzeitspektrometers für das BGO-OD-Experiment*, bachelor thesis: Rheinische Friedrich-Wilhelms-Universität Bonn, Aug. 2014, URL: https://www.hsag.physik.uni-bonn.de/forschung/diplom-doktorarbeiten/bachelorarbeiten/BachelorThesis_PatrickBauer.pdf.

[Bel+07] F. Bellemann et al.,
Experimental study of the pd →^{3}He K^+K^- and pd →^{3}He ϕ reactions close to threshold,
Phys. Rev. C **75** (1 Jan. 2007) p. 015204,
URL: http://link.aps.org/doi/10.1103/PhysRevC.75.015204.

[Bel+99] F. Bellemann et al.,
Pion-pion p -wave dominance in the pd^{3}He$\pi^+\pi^-$ reaction near threshold,
Phys. Rev. C **60** (6 Nov. 1999) p. 061002,
URL: http://link.aps.org/doi/10.1103/PhysRevC.60.061002.

[Bel11] A. Bella, *Setup of a Goniometer System for the Production of Linearly Polarised Photons for the BGO-OD Experiment at ELSA*,
diploma thesis: Rheinische Friedrich-Wilhelms-Universität Bonn, 2011,
URL: https://www.hsag.physik.uni-bonn.de/forschung/diplom-doktorarbeiten/diplom-masterarbeiten/Diplomarbeit_AndreasBella.pdf.

[Bel16] A. Bella, *Linearly polarised photons at the BGO-OD experiment at ELSA*,
PhD thesis: Rheinische Friedrich-Wilhelms-Universität Bonn, 2016,
URL: http://nbn-resolving.de/urn:nbn:de:hbz:5n-44930.

[Bie11] J. Bieling, "FPGA module and firmware descriptions", BGO-OD-008-2011, Aug. 2011.

[Bie13] J. Bieling, "A 98-channel FPGA-based time-to-digital converter (TDC)",
DPG Frühjahrstagung, HK 53.7, Poster, 2013,
URL: http://www.dpg-verhandlungen.de/year/2013/conference/dresden/part/hk/session/53/contribution/7.

[Bie16] J. Bieling, *FPGA based 30ps RMS TDCs*, 2016,
URL: https://github.com/jobisoft/jTDC/.

[Ble+70] A. Bleckmann et al.,
Photoproduction of $K^+\Lambda$ and $K^+\Sigma^0$ from hydrogen between 1.3 and 1.45 GeV,
Zeitschrift für Physik **239**.1 (1970) pp. 1–15, ISSN: 0044-3328,
URL: http://dx.doi.org/10.1007/BF01408507.

[Bös16] S. Böse, *Aufbau und Test eines neuen Szintillationsfaser-Detektors für das neue Vorwärtsspektrometer an ELSA*,
PhD thesis: Rheinische Friedrich-Wilhelms-Universität Bonn, 2016,
URL: http://nbn-resolving.de/urn:nbn:de:hbz:5n-43001.

[BR97] R. Brun and F. Rademakers, *New Computing Techniques in Physics Research V ROOT — An object oriented data analysis framework*,
Nuclear Instruments and Methods in Physics Research Section A: Accelerators, Spectrometers, Detectors and Associated Equipment **389**.1 (1997) pp. 81–86,
ISSN: 0168-9002, URL: http://root.cern.ch.

[Bra+06] R. Bradford et al., *Differential cross sections for $\gamma + p \to K^+ + Y$ for Λ and Σ^0 hyperons*,
Phys. Rev. C **73** (3 Mar. 2006) p. 035202,
URL: http://link.aps.org/doi/10.1103/PhysRevC.73.035202.

[Bra+07] R. K. Bradford et al.,
First measurement of beam-recoil observables C_x and C_z in hyperon photoproduction,
Phys. Rev. C **75** (3 Mar. 2007) p. 035205,
URL: http://link.aps.org/doi/10.1103/PhysRevC.75.035205.

[Bro+72] C. N. Brown et al., *Coincidence Measurements of Single K^+ Electroproduction*, Phys. Rev. Lett. **28** (16 Apr. 1972) pp. 1086–1089, URL: http://link.aps.org/doi/10.1103/PhysRevLett.28.1086.

[Brü14] T. Brück, *Messung der Targetpolarisation für das BGO-OD Møllerpolarimeter*, bachelor thesis: Rheinische Friedrich-Wilhelms-Universität Bonn, Aug. 2014, URL: https://www.hsag.physik.uni-bonn.de/forschung/diplom-doktorarbeiten/bachelorarbeiten/Bachelorarbeit_TobiasBrueck.pdf.

[CAEa] CAEN, *MOD. V1290 A/N VX1290 A/N 32/16 CHANNEL MULTIHIT TDCs*, URL: http://www.caen.it/servlet/checkCaenManualFile?Id=8653.

[CAEb] CAEN, *V1190 A/B VX1190 A/B MULTIHIT TDCs MANUAL REV.13*, URL: http://www.caen.it/servlet/checkCaenManualFile?Id=8657.

[Čer37] P. A. Čerenkov, *Visible Radiation Produced by Electrons Moving in a Medium with Velocities Exceeding that of Light*, Phys. Rev. **52** (4 Aug. 1937) pp. 378–379, URL: http://link.aps.org/doi/10.1103/PhysRev.52.378.

[Cho+03] S.-K. Choi et al., *Observation of a Narrow Charmoniumlike State in Exclusive $B^\pm \to K^\pm \pi^+ \pi^- J/\psi$ Decays*, Phys. Rev. Lett. **91** (26 Dec. 2003) p. 262001, URL: http://link.aps.org/doi/10.1103/PhysRevLett.91.262001.

[CKT93] Y. F. Chen, C. M. Kwei, and C. J. Tung, *Analytic functions for atomic momentum-density distributions and Compton profiles of K and L shells*, Phys. Rev. A **47** (5 May 1993) pp. 4502–4505, URL: http://link.aps.org/doi/10.1103/PhysRevA.47.4502.

[CT97] W.-T. Chiang and F. Tabakin, *Completeness rules for spin observables in pseudoscalar meson photoproduction*, Phys. Rev. C **55** (4 Apr. 1997) pp. 2054–2066, URL: http://link.aps.org/doi/10.1103/PhysRevC.55.2054.

[Dav+96] J. C. David et al., *Electromagnetic production of associated strangeness*, Phys. Rev. C **53** (6 June 1996) pp. 2613–2637, URL: http://link.aps.org/doi/10.1103/PhysRevC.53.2613.

[Dol98] D. Doll, *Das Compton-Polarimeter an ELSA*, PhD thesis: Rheinische Friedrich-Wilhelms-Universität Bonn, 1998, URL: http://www-elsa.physik.uni-bonn.de/Publikationen/texte/dis_bonn-ir-98-08_dietmar_doll.pdf.

[Ebe06] H. Eberhardt, *Messung der Targetpolarisation und Detektorstudie für das Møllerpolarimeter des Crystal-Barrel-Aufbaus an ELSA*, German, diploma thesis: Rheinische Friedrich-Wilhelms-Universität Bonn, 2006, URL: https://www.hsag.physik.uni-bonn.de/forschung/diplom-doktorarbeiten/diplom-masterarbeiten/EberhardtDiplom.pdf.

[Elj] Eljen Technology, *EJ-204 PLASTIC SCINTILLATOR*, URL: http://www.eljentechnology.com/images/stories/Data_Sheets/Plastic_Scintillators/ej204%20data%20sheet.pdf.

[ELS] ELSA, *Conceptual Design of ELSA*, URL: http://www-elsa.physik.uni-bonn.de/Beschleuniger/bilder/elsaplan_en.pdf.

[ET] ET Enterprises, *25 mm (1") photomultiplier 9111B series data sheet*, URL: https://my.et-enterprises.com/pdf/9111B.pdf.

[Fre12] T. Frese, *Insitu field measurement of the Open Dipole magnet at the BGO-OD experiment*, diploma Thesis: Rheinische Friedrich-Wilhelms-Universität Bonn, Dec. 2012, URL: https://www.hsag.physik.uni-bonn.de/forschung/diplom-doktorarbeiten/diplom-masterarbeiten/Diplomarbeit_TorstenFrese.pdf.

[Fre15] O. Freyermuth, "A new FPGA-based Time-over-Threshold System for the Time of Flight Detectors at the BGO-OD Experiment", *DPG Frühjahrstagung*, HK 41.2, 2015, URL: http://www.dpg-verhandlungen.de/year/2015/conference/heidelberg/part/hk/session/41/contribution/2.

[Fre16] O. Freyermuth, "Fast and Convenient Data Analysis Software at the BGO–OD Experiment", *DPG Frühjahrstagung*, HK 8.1, 2016, URL: http://www.dpg-verhandlungen.de/year/2016/conference/darmstadt/part/hk/session/8/contribution/1.

[Fuc05] M. Fuchs, *Photoproduktion neutraler Pionpaare mit dem Crystal-Barrel-Detektor an ELSA*, PhD thesis: Rheinische Friedrich-Wilhelms-Universität Bonn, 2005, URL: http://nbn-resolving.de/urn:nbn:de:hbz:5N-05830.

[Gen99] M. Gentner, *Präparation von Teilchenstrahlen für Experimente der Hadronenphysik: langsame Extraktion an ELFE@DESY und ELSA, sowie Strahlkühlung an HERA*, PhD thesis: Rheinische Friedrich-Wilhelms-Universität Bonn, 1999, URL: http://www-elsa.physik.uni-bonn.de/Publikationen/texte/gentner_dr.pdf.

[Ghi+98a] F. Ghio et al., *The GRAAL high resolution BGO calorimeter and its energy calibration and monitoring system*, Nuclear Instruments and Methods in Physics Research Section A: Accelerators, Spectrometers, Detectors and Associated Equipment **404**.1 (1998) pp. 71–86, ISSN: 0168-9002, URL: http://www.sciencedirect.com/science/article/pii/S0168900297011248.

[Ghi+98b] F. Ghio et al., *The GRAAL high resolution BGO calorimeter and its energy calibration and monitoring system*, Nuclear Instruments and Methods in Physics Research Section A: Accelerators, Spectrometers, Detectors and Associated Equipment **7404**.1 (1998) pp. 71–86, ISSN: 0168-9002, URL: http://www.sciencedirect.com/science/article/pii/S0168900297011248.

[Gla+04] K.-H. Glander et al., *Measurement of $\gamma p \to K^+\Lambda$ and $\gamma p \to K^+\Sigma^0$ at photon energies up to 1.47 GeV*, The European Physical Journal A - Hadrons and Nuclei **19**.2 (2004) pp. 251–273, ISSN: 1434-601X, URL: http://dx.doi.org/10.1140/epja/i2003-10119-x.

[Gow01] M. Gowin, *Optimierung der laserinduzierten Photoemission zur Erzeugung polarisierter Elektronenstrahlen an der 50 ke V-Quelle der Bonner Beschleunigeranlage ELSA*, PhD thesis: Rheinische Friedrich-Wilhelms-Universität Bonn, 2001, URL: http://www-elsa.physik.uni-bonn.de/Publikationen/texte/gowin_dr.pdf.

[Gut+14] E. Gutz et al., *High statistics study of the reaction $\gamma p \to p\pi^0\eta$*, The European Physical Journal A **50**.4 (2014) pp. 1–27, ISSN: 1434-601X, URL: http://dx.doi.org/10.1140/epja/i2014-14074-1.

[Hama] Hamamatsu Photonics, *Metal Package Photomultiplier tube R29880U Series*, URL: https://www.hamamatsu.com/resources/pdf/etd/R9880U_TPMH1321E.pdf.

[Hamb] Hamamatsu Photonics, *Photomultiplier Tube Assemblies*, URL: http://www.hamamatsu.com/resources/pdf/etd/PMT_78-85_e.pdf.

[Hamc] Hamamatsu Photonics, *Photomultiplier tube R2083, R3377*, URL: https://www.hamamatsu.com/resources/pdf/etd/R2083_R3377_TPMH1227E.pdf.

[Ham08] D. Hammann, *Test und Betrieb der Prototyp-Driftkammer für das B1-Spektrometer*, German, diploma thesis: Rheinische Friedrich-Wilhelms-Universität Bonn, 2008, URL: https://www.hsag.physik.uni-bonn.de/forschung/diplom-doktorarbeiten/diplom-masterarbeiten/Diplomarbeit_DanielHammann.pdf.

[Ham16] D. Hammann, *The data acquisition for the BGO-OD experiment*, PhD thesis: Rheinische Friedrich-Wilhelms-Universität Bonn, 2016, URL: http://nbn-resolving.de/urn:nbn:de:hbz:5n-44095.

[Hil00] W. Hillert, *Erzeugung eines Nutzstrahls spinpolarisierter Elektronen an der Beschleunigeranlage ELSA*, Habilitation thesis, PhD thesis: Rheinische Friedrich-Wilhelms-Universität Bonn, 2000, URL: http://www-elsa.physik.uni-bonn.de/Publikationen/texte/hillert_habil.pdf.

[Hof01] M. Hoffmann, *Beschleunigung polarisierter Elektronen in der Bonner Elektronen-Beschleunigeranlage ELSA*, PhD thesis: Rheinische Friedrich-Wilhelms-Universität Bonn, Dec. 2001, URL: http://nbn-resolving.de/urn:nbn:de:hbz:5n-00512.

[Ire16] D. G. Ireland, "N* Physics with Meson Photoproduction at CLAS", *Proceedings of the 10th International Workshop on the Physics of Excited Nucleons (NSTAR2015)*, 2016, eprint: http://journals.jps.jp/doi/pdf/10.7566/JPSCP.10.010001, URL: http://journals.jps.jp/doi/abs/10.7566/JPSCP.10.010001.

[Jah] R. Jahn, *MOMO*, URL: https://bgo-od.physik.uni-bonn.de/ExperimentalSetup/Momo.

[Jud+14] T. Jude et al., *$K^+\Lambda$ and $K^+\Sigma^0$ photoproduction with fine center-of-mass energy resolution*, Physics Letters B **735** (2014) pp. 112–118, ISSN: 0370-2693, URL: http://www.sciencedirect.com/science/article/pii/S0370269314004109.

[Jud11] T. Jude, "Charged particle track reconstruction in the forward spectrometer", BGO-OD-021-2011, July 2011.

[Jud16] T. Jude, "Alignments, energy corrections, efficiencies and resolutions applied to data at the preanalysis stage", BGO-OD-027-2016, July 2016.

[Kam10] S. Kammer, *Strahlpolarimetrie am CBELSA/TAPS Experiment*, PhD thesis: Rheinische Friedrich-Wilhelms-Universität Bonn, 2010, URL: http://nbn-resolving.de/urn:nbn:de:hbz:5N-20564.

[Kla11] F. Klarner,
Konzeption, Aufbau und Inbetriebnahme eines neuen Vorbeschleunigersystems an ELSA,
PhD thesis: Rheinische Friedrich-Wilhelms-Universität Bonn, 2011,
URL: http://nbn-resolving.de/urn:nbn:de:hbz:5N-27211.

[Kni] Knight Optical, *PTK3000*, URL: http://www.knightoptical.com/stock/optical-components/uvvisnir-optics/prisms/right-angle-prisms/precision-right-angle-prisms-bk7-or-equivalent-/right-angle-prism-bk7-30x30mm-entryexit-face-uncoated/.

[Koh16] K. Kohl, *Absolute measurement of the Photon Flux of the BGO-OD experiment*,
in preparation,
master thesis: Rheinische Friedrich-Wilhelms-Universität Bonn, Sept. 2016.

[Koo] R. Koop, under preparation,
PhD thesis: Rheinische Friedrich-Wilhelms-Universität Bonn.

[Lee+01] F. Lee et al., *Quasifree kaon photoproduction on nuclei*,
Nuclear Physics A **695**.1–4 (2001) pp. 237–272, ISSN: 0375-9474, URL:
http://www.sciencedirect.com/science/article/pii/S0375947401010983.

[Lei14] B. Leibrock,
Erstinbetriebnahme der Vieldrahtproportionalkammer des BGO-OD-Experiments,
bachelor thesis: Rheinische Friedrich-Wilhelms-Universität Bonn, Sept. 2014,
URL: https://www.hsag.physik.uni-bonn.de/forschung/diplom-doktorarbeiten/bachelorarbeiten/Bachelorarbeit_BarbaraLeibrock.pdf.

[Lev94] L. Levchuk,
The intra-atomic motion of bound electrons as a possible source of the systematic error in electron beam polarization measurements by means of a Möller polarimeter,
Nuclear Instruments and Methods in Physics Research Section A: Accelerators, Spectrometers, Detectors and Associated Equipment **345**.3 (1994) pp. 496–499,
ISSN: 0168-9002, URL:
http://www.sciencedirect.com/science/article/pii/0168900294905053.

[Lle+07] A. Lleres et al., *Polarization observable measurements for $\gamma p \to K^+\Lambda$ and $\gamma p \to K + \Sigma^0$ for energies up to 1.5 GeV*, The European Physical Journal A **31**.1 (2007) pp. 79–93,
ISSN: 1434-601X, URL: http://dx.doi.org/10.1140/epja/i2006-10167-8.

[Lle+09] A. Lleres et al., *Measurement of beam-recoil observables Ox , Oz and target asymmetry T for the reaction $\gamma p \to K^+\Lambda$*, The European Physical Journal A **39**.2 (2009) pp. 149–161,
ISSN: 1434-601X, URL: http://dx.doi.org/10.1140/epja/i2008-10713-4.

[LMP01] U. Löring, B. Metsch, and H. Petry, *The light-baryon spectrum in a relativistic quark model with instanton-induced quark forces*,
The European Physical Journal A - Hadrons and Nuclei **10**.4 (2001) pp. 395–446,
ISSN: 1434-601X, URL: http://dx.doi.org/10.1007/s100500170105.

[MA10] P. Markowitz and A. Acha, *LOW Q2 KAON ELECTROPRODUCTION*,
International Journal of Modern Physics E **19**.12 (2010) pp. 2383–2386, eprint:
http://www.worldscientific.com/doi/pdf/10.1142/S0218301310016843,
URL: http://www.worldscientific.com/doi/abs/10.1142/S0218301310016843.

[Max] Maxim Integrated, *±18-Bit ADC with Serial Interface*,
URL: http://datasheets.maximintegrated.com/en/ds/MAX132.pdf.

[McC+10] M. E. McCracken et al., *Differential cross section and recoil polarization measurements for the $\gamma p \to K^+\Lambda$ reaction using CLAS at Jefferson Lab*, Phys. Rev. C **81** (2 Feb. 2010) p. 025201, URL: http://link.aps.org/doi/10.1103/PhysRevC.81.025201.

[McN+10] E. F. McNicoll et al., *Experimental study of the $\gamma p \to \eta p$ reaction with the Crystal Ball detector at the Mainz Microtron (MAMI-C)*, Phys. Rev. C **82** (3 Sept. 2010) p. 035208, URL: http://link.aps.org/doi/10.1103/PhysRevC.82.035208.

[Mei13] P. Meiß, *The Time Of Flight Spectrometer of the BGO-OD Experiment*, diploma Thesis: Rheinische Friedrich-Wilhelms-Universität Bonn, Sept. 2013, URL: https://www.hsag.physik.uni-bonn.de/forschung/diplom-doktorarbeiten/diplom-masterarbeiten/Diplomarbeit_PeterMeiss.pdf.

[Mes14] F. Messi, "BGO-OD SetUp", BGO-OD-023-2014, Sept. 2014.

[Mes15] F. Messi, *The Tagging System of the BGO-OD experiment*, PhD thesis: Rheinische Friedrich-Wilhelms-Universität Bonn, 2015, URL: http://nbn-resolving.de/urn:nbn:de:hbz:5n-40284.

[Mic96] T. Michel, *Konzeption eines Møllerpolarimeters für das Experiment zur Überprüfung der Gerasimov-Drell-Hearn Summenregel*, German, diploma thesis: Rheinische Friedrich-Wilhelms-Universität Bonn, 1996, URL: http://www.pi4.nat.uni-erlangen.de/novel-detectors/publications/phd-diplomathesis/michel_diplom.ps.

[Møl32] C. Møller, *Zur Theorie des Durchgangs schneller Elektronen durch Materie*, Annalen der Physik **406**.5 (1932) pp. 531–585, ISSN: 1521-3889, URL: http://dx.doi.org/10.1002/andp.19324060506.

[Mül15] J. Müller, "Baryon Spectroscopy: Measurement of the Double Polarisation Observable E in η Photoproduction", Talk at SFB/TR 16 Students Exchange Week, 2015.

[New13] Newport, *URS-BPPV6 Series*, 2013, URL: https://www.newport.com/medias/sys_master/images/images/hca/h1f/8797298262046/URS-BPPV6-Data-Sheet.pdf.

[Oli+14] K. A. Olive et al., *Review of Particle Physics*, Chin. Phys. **C38** (2014) p. 090001.

[OM59] H. Olsen and L. C. Maximon, *Photon and Electron Polarization in High-Energy Bremsstrahlung and Pair Production with Screening*, Phys. Rev. **114** (3 1959) pp. 887–904, URL: http://link.aps.org/doi/10.1103/PhysRev.114.887.

[Pat+16] C. A. Paterson et al., *Photoproduction of Λ and Σ^0 hyperons using linearly polarized photons*, Phys. Rev. C **93** (6 June 2016) p. 065201, URL: http://link.aps.org/doi/10.1103/PhysRevC.93.065201.

[Ras] Raspberry Pi Foundation, *Raspberry Pi 1 Model B+*, URL: https://www.raspberrypi.org/products/model-b-plus/.

[Rei15] B.-E. Reitz, *Coherent bremsstrahlung with the scintillating fiber detector of the BGO-OD tagging system*,
master thesis: Rheinische Friedrich-Wilhelms-Universität Bonn, Oct. 2015,
URL: https://www.hsag.physik.uni-bonn.de/forschung/diplom-doktorarbeiten/diplom-masterarbeiten/Masterarbeit_Bjoern-EricReitz.pdf.

[Rut11] E. Rutherford, *The scattering of α and β particles by matter and the structure of the atom*, Philosophical Magazine **21** (1911) pp. 669–688,
URL: http://www.math.ubc.ca/~cass/rutherford/rutherford.html.

[Sai] Saint-Gobain Crystals,
BC-440, BC-440M, BC-448, BC-448M Premium Plastic Scintillators,
URL: http://www.crystals.saint-gobain.com/uploadedFiles/SG-Crystals/Documents/SGC%20BC440%20BC448%20Series%20Data%20Sheet.pdf.

[San+96] P. L. Sandri et al.,
Performance of a {BGO} calorimeter in a tagged photon beam from 260 to 1150 MeV,
Nuclear Instruments and Methods in Physics Research Section A: Accelerators, Spectrometers, Detectors and Associated Equipment **370**.2–3 (1996) pp. 396–402,
ISSN: 0168-9002, URL:
http://www.sciencedirect.com/science/article/pii/016890029500839X.

[Sar+14] A. V. Sarantsev et al., *Bonn-Gatchina Partial Wave Analysis*, 2014,
URL: http://pwa.hiskp.uni-bonn.de/.

[SB14] G. Scheluchin and J. Bieling, "Spartan 6 firmwares (jTDC v6 and derivatives)",
BGO-OD-022-2014, Sept. 2014.

[SB16] D. Skoupil and P. Byd žovský, *Photoproduction of KΛ on the proton*,
Phys. Rev. C **93** (2 Feb. 2016) p. 025204,
URL: http://link.aps.org/doi/10.1103/PhysRevC.93.025204.

[Sch+94] W. Schwille et al., *Design and construction of the SAPHIR detector*,
Nuclear Instruments and Methods in Physics Research Section A: Accelerators, Spectrometers, Detectors and Associated Equipment **344**.3 (1994) pp. 470–486,
ISSN: 0168-9002, URL:
http://www.sciencedirect.com/science/article/pii/0168900294908680.

[Sch+98] C. Schaerf et al., *GRAAL Experiment at the ESRF*,
Nuclear Physics News **8**.1 (1998) pp. 24–28,
eprint: http://dx.doi.org/10.1080/10506899809410857,
URL: http://dx.doi.org/10.1080/10506899809410857.

[Sch10] T. Schwan,
Test und Inbetriebnahme der Driftkammern für das BGO-OD-Spektrometer, German,
diploma thesis: Rheinische Friedrich-Wilhelms-Universität Bonn, 2010,
URL: https://www.hsag.physik.uni-bonn.de/forschung/diplom-doktorarbeiten/diplom-masterarbeiten/Diplomarbeit_TimoSchwan.pdf.

[Sch12] L. Schildgen, *Charakterisierung des Antwortverhaltens der Time-of-Flight-Detektoren des BGO-OD-Experiments*,
bachelor thesis: Rheinische Friedrich-Wilhelms-Universität Bonn, July 2012.

[Sch13] G. Scheluchin, *Detektorsystem für das BGO-OD Møller-Polarimeter*, bachelor thesis: Rheinische Friedrich-Wilhelms-Universität Bonn, June 2013, URL: https://www.hsag.physik.uni-bonn.de/forschung/diplom-doktorarbeiten/bachelorarbeiten/Bachelorarbeit_GeorgScheluchin.pdf.

[Sch15a] G. Scheluchin, *Meson photoproduction on the proton using the BGO-OD detector complemented by a new Scintillating Ring (SciRi)*, master thesis: Rheinische Friedrich-Wilhelms-Universität Bonn, Aug. 2015, URL: https://www.hsag.physik.uni-bonn.de/forschung/diplom-doktorarbeiten/diplom-masterarbeiten/Masterarbeit_GeorgScheluchin.pdf.

[Sch15b] M. Schedler, *Intensitäts- und Energieerhöhung an ELSA*, PhD thesis: Rheinische Friedrich-Wilhelms-Universität Bonn, 2015, URL: http://nbn-resolving.de/urn:nbn:de:hbz:5n-42070.

[SHE] SHENZHEN KORAD TECHNOLOGY CO., LTD., *KA3005P Control Power*, URL: http://koradtechnology.com/en/cp-11.html.

[Sum+06] M. Sumihama et al., *The $\vec{\gamma}\, p \to K^+\Lambda$ and $\vec{\gamma}\, p \to K^+\Sigma^0$ reactions at forward angles with photon energies from 1.5 to 2.4 GeV*, Phys. Rev. C **73** (3 Mar. 2006) p. 035214, URL: http://link.aps.org/doi/10.1103/PhysRevC.73.035214.

[VAC] VACUUMSCHMELZE GmbH & Co. KG, *Soft Magnetic Cobalt-Iron-Alloys*, URL: http://www.vacuumschmelze.com/fileadmin/docroot/medialib/documents/broschueren/htbrosch/Pht-004_e.pdf.

[Wag+90] B. Wagner et al., *A Møller polarimeter for {CW} and pulsed intermediate energy electron beams*, Nuclear Instruments and Methods in Physics Research Section A: Accelerators, Spectrometers, Detectors and Associated Equipment **294**.3 (1990) pp. 541–548, ISSN: 0168-9002, URL: http://www.sciencedirect.com/science/article/pii/016890029090296I.

[Wal14] D. Walther, personal communication, Sept. 25, 2014.

[WIE] W-IE-NE-R, Plein & Baus GmbH, *W-Ie–Ne-R AVM16 / AVX16*, URL: http://file.wiener-d.com/documentation/AVM16/WIENER_AVM16-Manual_2.0.pdf.

[Wu+05] C. Wu et al., *Photoproduction of ρmesons and Δ-baryons in the reaction $\gamma p \to p\pi^+\pi^-$ at energies up to $\sqrt{s} = 2.6$ GeV*, The European Physical Journal A - Hadrons and Nuclei **23**.2 (2005) pp. 317–344, ISSN: 1434-601X, URL: http://dx.doi.org/10.1140/epja/i2004-10093-9.

[Zim12] T. Zimmermann, *PhotonFluxMonitor for the BGO-OD experiment*, diploma Thesis: Rheinische Friedrich-Wilhelms-Universität Bonn, Jan. 2012, URL: https://www.hsag.physik.uni-bonn.de/forschung/diplom-doktorarbeiten/diplom-masterarbeiten/Diplomarbeit_ThomasZimmermann.pdf.

[Züg15] P. Züge, *Aufbau und Test eines segmentierten Plastik-Szintillationsdetektors für das BGO-OD Experiment*,
bachelor thesis: Rheinische Friedrich-Wilhelms-Universität Bonn, July 2015,
URL: https://www.hsag.physik.uni-bonn.de/forschung/diplom-doktorarbeiten/bachelorarbeiten/Bachelorarbeit_PaulZuege.pdf.

List of Figures

List of Tables

Acronyms

ADC analog to digital converter. 27, 29, 46, 68, 119

APD avalanche photo diode. 24, 118

DAQ data acquisition. 18, 25, 26

ELSA Electron Stretcher Accelerator. 9, 10, 12, 34, 49, 53, 117

FPGA field-programmable gate array. 15, 26, 49, 51

GIM Gamma Intensity Monitor. 16

MRPC multi gap resistive plate chamber. 24

MWPC multi wire proportional chamber. 17–19, 25, 29, 118, 123

PMT photomultiplier tube. 15, 16, 18, 21, 25, 29, 48, 49, 118, 123

PWA partial wave analysis. 3, 4, 71, 75, 76, 79

QCD quantum chromo dynamics. 1

SADC sampling analog to digital converter. 18, 19, 27

TDC time to digital converter. 15, 20, 25, 27, 49–51, 68, 120

TOF time of flight. 19, 20, 23–26, 30, 32, 118, 123

ToT time over threshold. 15, 29, 49, 119